A new design of a compact strontium cold-atom source



Dongyang Xu

Linacre College

University of Oxford

A thesis submitted for the degree of

Doctor of Philosophy

Michaelmas 2020

Acknowledgements

First, I want to thank Chris for his help over the last few years on research and various other tasks. Chris is very quick on feeding back on new ideas and I can always learn useful things from him. Also, he is very supportive for students and working under Chris' supervision is a very delightful thing. His book has been the most frequently used textbook for me, which contains a lot of useful materials for cold atoms. Just like his book, Chris is someone that you can always count on and turn to during difficult times.

Then, I want to thank Elliot for his warm friendship and generous help for all this time. Elliot is a super smart researcher with clear mind and outstanding practical skills. I am always amazed by his speed in learning new things and also inspired by seeing him exploring his potential and capacity. I really admire him for being so capable and enthusiastic. He is someone that you always know he will succeed in every thing he wants to achieve. Elliot is also a caring person and always generously helps me with my questions and problems about researches and life.

Thanks for Sean with various help not only about researches, but also about living a dedicated life. He is such a faithful, generous and loving person that always offers a helping hand to surroundings without pursuing anything return. I was lucky to have the chance to work with him.

Also, thanks for my group members and former group members: Ben, David, Adam, Shinichi, Kathrin, Peter, and Rowan for their company and support. There is nothing more honoured for me than having the chance to working with such a group of active and motivated experimentalists.

I want to thank my parents for their continuous support for me. It is a pity that I could not accompany them a lot over the last couple of years. Their enthusiasm and positive attitudes towards life comfort me a lot when I feel nervous about the future. Thanks for my housemates: Shaobo, Oscar, Zhifeng, Reevu and Ben for the fun and joy they bring to me.

Thanks for staff and reseachers in Oxford Physics Department. Also, I want to thank NUDT for sponsoring my project.

A new design of a compact strontium cold-atom source

Dongyang Xu

A thesis submitted for the degree of Doctor of Philosophy

Abstract

A high-flux compact source of strontium atoms has been designed and built. We have investigated the feasibility of direct trapping of cold atoms from the atomic flux out of a hot oven. Our design uses a two-dimensional magneto-optical trap (MOT) with an additional laser beam that exerts a radiation force that is not counterbalanced to eject atoms (so-called 'push' beam), which is known as a $2D^+$ MOT configuration. This approach has been previously used for sodium, and has been extended to strontium in this work. Laser cooling of strontium typically requires multiple stages: effusion of atoms from an oven to produce an atomic beam, transverse collimation, a Zeeman slower and deflection before finally collecting atoms in a 3D MOT. A $2D^+$ MOT combines the Zeeman slowing, transverse collimation, and deflection into a single compact stage to provide a high-flux source suitable for applications such as matter-wave interferometry, atomic clocks and experimental studies of degenerate quantum gases.

This thesis reports experimental work that has been carried out to develop and test an oven and the associated laser cooling apparatus for producing a source of cold strontium atoms which is straightforward to manufacture. We test the oven up to a temperature of $T_o = 642\,^{\circ}\mathrm{C}$ and measure a peak intensity of $6.8 \times 10^{16}\,\mathrm{s^{-1}\,sr^{-1}}$ and a flux of $2.9 \times 10^{16}\,\mathrm{s^{-1}}$. We typically operate the oven at $T_o = 502\,^{\circ}\mathrm{C}$, for which the peak intensity and flux are $2.2 \times 10^{15}\,\mathrm{s^{-1}\,sr^{-1}}$ and $7.5 \times 10^{14}\,\mathrm{s^{-1}}$. A multi-channel nozzle made of graphite gives an angular divergence of 0.17 rad (10°) for the atomic beam. Trapping atoms directly from the thermal atomic beam into the MOT gives a maximum loading rate of $7.1 \times 10^{10}\,\mathrm{s^{-1}}$, without any laser light to repump atoms into the cooling cycle. We demonstrated a novel frequency stabilising technique for the laser by developing Zeeman-tunable modulation transfer spectroscopy in strontium with an inaccuracy of ±3.5 MHz and a frequency tuning range of 160 MHz.

The initial aim of this thesis was to make a compact, high-flux strontium source suitable for quantum technology applications. During the course of this research, we participated in the preparation of a proposal for the construction of a large-scale atom interferometer based on the clock transition in strontium (^{87}Sr) for the exploration of dark matter and gravitational waves (a project known as the Atom Interferometer Observatory and Network, AION). This changed the design requirements towards producing a higher flux (in particular of the isotope ^{87}Sr), with compactness of the source being less important in ∼10 m scale apparatus.

Contents

1 Introduction and background **1**

1.1 Laser cooling of alkaline-earth metals 1

1.2 Theory for laser cooling 2

1.2.1 Two-level system 2

1.2.2 Radiation forces 5

1.2.3 Optical molasses 6

1.2.4 The Doppler cooling limit 8

1.2.5 The magneto-optical trap 8

1.3 Properties of atomic strontium 10

1.3.1 Difference between the isotopes ^{87}Sr and ^{88}Sr 14

1.3.2 Applications of strontium 16

1.4 Motivation and research gap 17

1.4.1 Our design 18

2 Apparatus: oven and vacuum system **20**

2.1 Survey of previous oven designs 21

2.1.1 A simple source: an externally heated tube 21

2.1.2 A traditional atomic oven with in-vacuum heaters 22

2.1.3 Previous re-entrant oven design 23

2.2 Our re-entrant oven design 23

2.2.1 Oven body 24

2.2.2 Nozzle 27

2.3 Atomic flux calculation 27

2.3.1 Velocity distribution 27

2.3.2 Flux out of an aperture 30

2.3.3 Effusion of atoms through a tube 35

2.3.3.1 Collision-less vs. continuum flow ('opaque' mode) . . 35

2.3.3.2 Mean free path and flow regimes 37

2.3.3.3 Collision-less flow (Free molecular flow) 37
2.3.4 Hydrodynamic flow (opaque mode) 40
2.4 Heaters and the temperature control system 40
2.5 The vacuum system 42
2.5.1 MOT chamber 46
2.5.1.1 Main chamber 46
2.5.1.2 Coils for the MOT chamber 46
2.5.2 Supporting and viewports 49
2.5.3 Spectroscopy chamber 49
2.5.3.1 Oven for the spectroscopy chamber 50
2.5.3.2 Coils for the spectroscopy chamber 51
2.5.4 Pumping 51
2.6 Conclusion 51

3 Characterisation of the oven **53**
3.1 Thermal performance of the oven 53
3.1.1 Thermocouple measurements 53
3.1.2 Power consumption 54
3.1.3 Heat loss by conduction, radiation and convection 55
3.1.4 Conductivity of strontium vapour 60
3.1.5 Nozzle temperatures 60
3.2 Flux measurement by absorption spectroscopy 61
3.2.1 Doppler-broadened absorption spectroscopy 61
3.2.2 Measurements of atomic flux 65
3.3 Opaque mode 69
3.3.1 Flux and peak intensity 73
3.4 Absorption of the laser light (MOT beams) 74
3.5 Conclusion 77

4 Apparatus: laser system **79**
4.1 Mathematical description of laser radiation 79
4.1.1 Gaussian beams for laser cooling 79
4.1.2 Polarisation of light 80
4.1.3 Polarising optics 81
4.2 Laser 82
4.2.1 Main laser table 82
4.2.2 SolsTiS Ti:sapphire laser 82

4.2.3 Frequency doubling cavity . . . 83
4.2.4 Beam distribution board . . . 84
4.2.5 Secondary distribution board . . . 86
4.2.6 Spectroscopy board . . . 87
4.2.7 Test module for polarisation . . . 87
4.3 Laser spectroscopy for frequency stabilisation . . . 89
4.3.1 Absorption spectroscopy . . . 89
4.3.2 Doppler-free absorption spectroscopy . . . 89
4.3.3 Polarisation spectroscopy . . . 91
4.3.4 DAVLL scheme . . . 92
4.3.5 Frequency modulation spectroscopy . . . 94
4.3.6 Modulation Transfer spectroscopy . . . 95
4.3.7 Tunable MTS . . . 96
4.3.8 locking electronics . . . 97

5 Magneto-optical trapping of strontium 102
5.1 MOT optics . . . 102
5.2 Measurements for trapped atoms . . . 102
5.2.1 Optics for measurements . . . 103
5.2.2 Data analysis . . . 103
5.2.3 Results . . . 107
5.2.3.1 Loading rate versus MOT beam intensity . . . 108
5.2.3.2 Loading rate versus the magnetic field gradient . . . 110
5.2.3.3 Loading rate versus frequency detuning . . . 110
5.2.3.4 Loading rate versus oven temperature . . . 112
5.2.3.5 Analysis of the losses . . . 113

6 Conclusion and outlook 117

A Thermal analysis of oven 122
A.1 Oven features . . . 122
A.2 Radiation exchange between surfaces . . . 122
A.3 Heat shield . . . 124
A.4 Temperature distribution over the outer surface . . . 126

B List of constants 129

References 129

List of Tables

1.1 Strontium isotopes and their properties 12
1.2 A comparison of the parameters involved in laser cooling for various elements 13
1.3 Data for the elements commonly used in laser-cooled atom experiments. More elements are listed in Ref [62]. 14

2.1 The root mean squared velocity of atoms in an effusive beam $[v_{rms}]_{\text{beam}}$ at different temperatures that are typically used. 31
2.2 Total flux and peak intensity at 500 °C for ideal apertures (infinitely thin wall) of different diameters. 35
2.3 Comparison between different nozzles' performance 39

3.1 ξ_0 and ξ_1 constraints or values in various models 73

5.1 Optimised power distribution for MOT beams 110

List of Figures

1.1 Interaction of an atom with a single beam 6
1.2 Interaction of an atom with two counter-propagating beams 7
1.3 Acceleration generated by two counter-propagating beams 7
1.4 3D MOT layout 10
1.5 Zeeman sub-levels with molasses 11
1.6 2D MOT diagram 11
1.7 Strontium energy structure 12
1.8 Proposed scheme for 2D+ MOT 19

2.1 A basic atomic source 21
2.2 The strontium vapour source in the apparatus at the USTC, China, is an externally heated tube, shown as the red tube at the bottom of the picture taken from Ref [53]. 22
2.3 Schioppo oven 23
2.4 Killian's group's oven with one cartridge heater and sperately heated nozzle 24
2.5 Our re-entrant oven design 25
2.6 CAD model and pictures of two versions of oven 26
2.7 CAD model and picture of graphite nozzles 28
2.8 The CAD models and pictures of single-hole metal nozzles 29
2.9 The velocity distributions of strontium-87 atoms in an effusive beam at different temperatures, as given by eqn 2.3 (normalised). 30
2.10 Diagram for solid angle and one element of solid angle 31
2.11 Volume atoms sweeps off with velocity v 33
2.12 Logplot for strontium vapour pressure over temperature 34
2.13 Flux-temperature and intensity-temperature curves for different diameters of aperture 35
2.14 Atomic flux coming off an tube 36
2.15 Mean-free path over temperature 37

2.16 Angular dependence $j(\theta)$ over angle θ 39
2.17 W-β curve 40
2.18 Logplot for total flux over temperature 41
2.19 Logplot of peak intensity over temperature 42
2.20 Customized cartridge heaters 43
2.21 Temperature control box with data logging function 44
2.22 Test chamber and scheme of 2D+ MOT source 45
2.23 MOT chamber front and side view 46
2.24 Picture of assembled MOT chamber 47
2.25 The magnetic field and gradient with 100 A current 48
2.26 Topview of the spectrscopy board 50

3.1 Temperatures measured 54
3.2 Total power consumption versus temperature 55
3.3 Oven diagram for thermal analysis 56
3.4 Heat radiation and conduction in a cylindrical tube 57
3.5 Heat radiation exchange between the tube and ambient chamber. . . 58
3.6 Radiation loss by radiation, conduction and air convection. 59
3.7 Images of heated nozzle 61
3.8 Equilibrium temperature of nozzle 62
3.9 A horizontal laser beam travels through the vertical atomic beam and then the absorption signal is recorded by a photodiode. 63
3.10 Diagram for a sample slice of atoms 64
3.11 Absorption lineshape with etalon peaks 66
3.12 Etalon fits 67
3.13 Normalised lineshape and sampled points 67
3.14 Normalised lineshape with fits 68
3.15 Fitting with free-collision model at high oven temperature 69
3.16 Angular dependence under Opaque mode in various models and under different temperatures 72
3.17 Absorption lineshape fitted with collision-free model and opaque model 73
3.18 Centerline intensity over temperatures in opaque mode 74
3.19 Fitted vapour temperatures and the RMSE for fits 75
3.20 Flux and peak intensity calculated with fitted vapour temperatures . 76
3.21 Power attenuation for the MOT beam 78

4.1 Optics layout in SolsTiS 83

4.2 Optics layout in ECD-X 84
4.3 Beam waist measurements 85
4.4 Beam radius versus distance to ECD-X 86
4.5 Test module for handedness of polarised light 88
4.6 An example of using the test module 88
4.7 Diagram for absorption spectroscopy 89
4.8 Diagram for Doppler-free absorption spectroscopy 90
4.9 Diagram for simplified doppler-free absorption spectroscopy 90
4.10 Profile of saturated 91
4.11 Profile of polarisation spectroscopy 92
4.12 Diagram for DAVLL spectroscopy 93
4.13 Diagram for sub-Doppler DAVLL spectroscopy 94
4.14 DAVLL lineshape 95
4.15 Image of 3D-printed 95
4.16 Frequency modulation spectroscopy 96
4.17 Modulation transfer spectroscopy lineshape 97
4.18 Diagram for detuning over current 98
4.19 Picture of the locking electronic box 99
4.20 Main laser table 100
4.21 Optics layout in secondary distribution board and spectroscopy board 101

5.1 MOT optics used in our experiment 103
5.2 Images of atoms trapped in MOT 104
5.3 Optics for fluorescence measurements 104
5.4 Calibration of beam power vs. photodiode's voltage 105
5.5 Fitting of a MOT loading trace 107
5.6 Time constant and loading rate vs. power 108
5.7 Probability distribution with v_p and FWHM 109
5.8 Deceleration in molasses under various beam intensity and detuning . 109
5.9 Time constant and loading rate versus B'_z 111
5.10 Time constant and loading rate versus detuning 111
5.11 Time constant and loading rate versus temperature 112
5.12 Collision rate between trapped atoms and atoms in the background atomic beam versus vapour temperature 114
5.13 $1/\tau$ versus detuning and power 115
5.14 Second-round data taken by camera with a different setting 116

6.1 Temperature versus number of atoms per second for various projects include AION 119
6.2 Diagram for the AION project 120
6.3 Distilling strontium by loading one oven with the other 120

A.1 Temperature versus total power consumed 123
A.2 Temperature distribution over the full range 124
A.3 Nozzle temperature vs. oven temperature in full range 125
A.4 Radiation exchange between two grey body surfaces. 125
A.5 Heat loss through radiation with Heat shield 126
A.6 A typical simplified temperature distribution oven oven body. 127

Chapter 1

Introduction and background

1.1 Laser cooling of alkaline-earth metals

Laser cooling was first demonstrated using sodium atoms [2] and was rapidly extended to other alkali metals. Alkali metals are highly suitable for laser cooling because they have a single valence electron, giving a simple atomic structure with a dominant (resonance) transition that can be reasonably approximated as a two-level system for excitation on, or near to, resonance. The development path of solid-state laser systems had a significant influence on the choice of atomic system, in particular the advent of reliable and inexpensive diode lasers that stimulated extensive work on the heavier alkalis: potassium (K)[27, 49], rubidium (Rb)[1] and cesium (Cs)[63]. Rubidium is particularly favourable because it has a transition of wavelength in the near-infrared, where commercial diode lasers are readily available. The high vapour pressure of Rb also makes it easy to work with, since generating a sufficient number of atoms for cooling and trapping does not require a high temperature oven, unlike other atomic systems (e.g. sodium[59]).

Alkaline-earth metals, and atoms with similar electronic structure such as ytterbium, are attracting growing interest for having transitions suitable for laser cooling. They also have very narrow transitions that allow much higher resolution spectroscopy and finer control. These atoms can be modelled as two-electron systems[1] (two spin-1/2 particles), which produces an energy level structure with terms that are either singlets or triplets (total spin S= 0 and 1 respectively). There is a selection rule that forbids transitions between singlet and triplet terms but this breaks down leads

[1]Helium is a true two-electron atomic system but transitions from its ground state can only be excited by vacuum ultraviolet radiation. So, experimentally, helium is laser-cooled using transitions from long-lived metastable states.

to a feature that is very useful for laser cooling: the existence of strong and weak transitions.

Strong transitions are those that are allowed by the angular momentum selection rules and their excited states have a short lifetime (due to rapid decay by spontaneous emission). Weak transitions are 'partially' forbidden by the selection rules but are observable because of the partial breakdown of the LS-coupling approximation for heavier atoms[2]. Thus, their excited states can be significantly longer lived, and they can have narrower linewidth transitions than are found in the alkalis, resulting in intercombination lines with very narrow bandwidths, and some very long-lived metastable states. Therefore, laser cooling of strontium can utilise a two-stage process: firstly using the large radiation force exerted by laser light on the strong transition to capture many atoms, and then cooling atoms to much lower temperatures using transitions with a narrow line width (but not too narrow otherwise the scattering rate is not sufficient). This atomic structure of alkaline-earth metals has been exploited in atomic frequency standards for many years using the very narrow 'clock' transitions, in particular, the 'clock' transition in ^{87}Sr.

The advance of reliable laser technology enabled work with alkaline-earth metals such as Sr, and other elements with two valence electrons such as Yb and Hg. The first alkaline-earth-metal-like element to be cooled to quantum degeneracy was ytterbium[74], followed by calcium[39]. A key breakthrough in the field was the first observation of a Bose-Einstein Condensation (BEC) of strontium led by Professor Florian Schreck[71]; two-stage laser cooling with two wavelengths produced a sample of atoms that was colder and denser than is possible with single-stage laser cooling of alkalis, and hence only a short period of evaporation was needed to reach quantum degeneracy. Work such as this requires a high initial number of atoms because evaporative cooling is an inherently lossy process, so a high flux source of cold strontium is of significant importance.

1.2 Theory for laser cooling

1.2.1 Two-level system

We apply a semi-classical solution to treat how a two-level atom interacts with radiation, which means that the radiation is described as a classical electric field and the

[2]This is more pronounced for heavier atoms, such as strontium, where the spin-orbit interaction is larger than in lighter atoms.

atom as a two-level quantum mechanical system. The time-dependent Schrödinger equation is

$$i\hbar\frac{d\Psi}{dt} = H\Psi. \tag{1.1}$$

The Hamiltonian H is written as the sum of two parts

$$H = H_0 + H_1(t), \tag{1.2}$$

The eigenvalues and eigenfunctions of H_0 represent energy levels and wave functions of the atom and the time-dependent component in the Hamiltonian, $H_1(t)$, describes the perturbation of the eigenfunctions of H_0 by the oscillating electric field. The wave function for an atomic level with energy E_n is

$$\Psi_n(\boldsymbol{r}, t) = \phi_n(\boldsymbol{r}) \exp(-iE_n t/\hbar). \tag{1.3}$$

For two-level system, where $|1\rangle$ is the ground state and $|2\rangle$ is the excited state, the respective wave functions satisfy

$$H_0\phi_1(\boldsymbol{r}) = E_1\phi_1(\boldsymbol{r}), \tag{1.4}$$

$$H_0\phi_2(\boldsymbol{r}) = E_2\phi_2(\boldsymbol{r}). \tag{1.5}$$

The total time-dependent wavefunction solution can be written as

$$\Psi(\boldsymbol{r}, t) = c_1(t)\,|1\rangle \exp(-i\omega_1 t/\hbar) + c_2(t)\,|2\rangle \exp(-i\omega_2 t/\hbar), \tag{1.6}$$

Here $\omega_1 = E_2/\hbar$ and $\omega_2 = E_2/\hbar$ for the basis states $|1\rangle \equiv \phi_1(\boldsymbol{r})$ and $|2\rangle \equiv \phi_2(\boldsymbol{r})$. The superposition state is normalised, $|c_1|^2 + |c_2|^2 = 1$. The radiation is described classically by an electric field oscillating at angular frequency ω

$$\boldsymbol{E} = \boldsymbol{E}_0 \cos(\omega t). \tag{1.7}$$

The perturbation Hamiltonian H_1 can be written as

$$H_1(t) = e\boldsymbol{r} \cdot \boldsymbol{E}, \tag{1.8}$$

where $\boldsymbol{r}$ is the position of the electron from the centre of mass, $-e\boldsymbol{r}$ is an electric dipole and H_1 is the energy of this dipole in the field. From eqn. (1.1), we find

$$i\dot{c}_1 = \Omega \cos(\omega t) \exp(-i\omega_0 t) c_2, \tag{1.9}$$

$$i\dot{c}_2 = \Omega^* \cos(\omega t) \exp(i\omega_0 t) c_1, \tag{1.10}$$

where $\omega_0 = (E_1 - E_2)/\hbar$, and $\Omega(\boldsymbol{r})$ is the Rabi frequency defined by:

$$\Omega = \frac{\langle 1 | \, e\boldsymbol{r} \cdot \boldsymbol{E} \, | 2 \rangle}{\hbar} \tag{1.11}$$

Writing $\cos(\omega t)$ in exponentials, we can write eqn. (1.9) as

$$i\dot{c}_1 = c_2 \left[e^{i(\omega - \omega_0)t} + e^{-i(\omega + \omega_0)t} \right] \frac{\Omega}{2}. \tag{1.12}$$

When we apply this general picture of an atom interacting with radiation to the case of laser cooling, the frequency of the radiation ω is close to the atomic resonance frequency ω_0, so $|\omega_0 - \omega| \ll \omega_0$ and $\omega_0 + \omega \backsim 2\omega_0$. The term with $(\omega + \omega_0)t$ oscillates rapidly so it can be averaged to zero for a reasonable interaction time. This is the rotating-wave approximation, and applying it simplifies eqn. (1.9) and eqn. (1.10) to

$$i\dot{c}_1 = \frac{\Omega}{2} c_2 e^{i\delta t}, \tag{1.13}$$

$$i\dot{c}_2 = \frac{\Omega^*}{2} c_1 e^{-i\delta t}, \tag{1.14}$$

where the frequency detuning $\delta = \omega - \omega_0$. With initial conditions $c_1(0) = 1$ and $c_2(0) = 0$, the probability in the upper state is given by

$$|c_2(t)|^2 = \frac{\Omega^2}{\Omega^2 + \delta^2} \sin^2 \left[\frac{(\Omega^2 + \delta^2)t}{2} \right]. \tag{1.15}$$

At resonance $\delta = 0$, this gives $|c_2(t)|^2 = \sin^2 \Big(\Omega t/2 \Big)$, so population oscillates between the two levels (Rabi oscillations). Introducing a radiative damping term and solving the optical Bloch equations[26], we can find the steady-state population of the upper level as

$$\rho_{22} = \frac{\Omega^2/4}{\delta^2 + \Omega^2/2 + \Gamma^2/4}, \tag{1.16}$$

where Γ is the natural linewidth of the transition. It is useful to define the saturation intensity I_{sat} in terms of Ω and Γ as

$$\frac{I}{I_{\text{sat}}} = \frac{2\Omega^2}{\Gamma^2}, \tag{1.17}$$

This is the definition used in Ref [26], which is consistent with standard textbooks on laser physics. There are other definitions used in laser cooling papers such as $I = I_{\text{sat}}$ when $\Omega = \Gamma$ (used by Cohen-Tannoudji).

1.2.2 Radiation forces

The semiclassical forces derived from the Hamiltonian H are [26]

$$\boldsymbol{F} = \frac{d\langle \boldsymbol{p} \rangle}{dt} = \boldsymbol{F}_{dipole} + \boldsymbol{F}_{scatt}, \tag{1.18}$$

$$\boldsymbol{F}_{\text{dipole}} = -\frac{\hbar\delta}{2}\frac{\Omega}{\delta^2 + \Omega^2/2 + \Gamma^2/4}\nabla\Omega, \tag{1.19}$$

$$\boldsymbol{F}_{\text{scat}} = \frac{\hbar\Gamma}{2}\frac{\Omega^2/2}{\delta^2 + \Omega^2/2 + \Gamma^2/4}\mathbf{k}, \tag{1.20}$$

where $\mathbf{k}$ is the wave vector for the laser light with wave number $k = |\mathbf{k}| = 2\pi/\lambda$. The dipole force $\boldsymbol{F}_{\text{dipole}} = 0$ at resonance $\delta = 0$. When $\delta > 0$, the dipole potential formed is maximised at the point with highest intensity, which is commonly the focus (waist) for the laser beam. So atoms are repelled from regions with higher intensity. While for $\delta < 0$, conversely, the atoms are attracted to regions with higher intensity. Techniques using the dipole force to confine atoms are called a dipole-force trap or dipole trap. The scattering force can be written in the form of scattering rate R_{scat} times the momentum of a single photon $\hbar k$

$$F_{\text{scat}} = R_{\text{scat}}\hbar k, \tag{1.21}$$

$$R_{\text{scat}} = \frac{\Gamma}{2}\frac{I/I_{\text{sat}}}{1 + I/I_{\text{sat}} + 4\delta^2/\Gamma^2}, \tag{1.22}$$

with eqn. (1.17). The scattering force has a maximum at resonance $\delta = 0$ and reaches a limiting value of $F_{\text{max}} = \hbar k\Gamma/2$ as $I \to \infty$. So the maximum acceleration that can be achieved is

$$a_{\text{max}} = \frac{F_{max}}{M} = \frac{\hbar k}{M}\frac{\Gamma}{2} = \frac{v_r}{2\tau}, \tag{1.23}$$

where $\tau = \Gamma^{-1}$ is the lifetime for radiative broadening (lifetime of an atom in the excited state of the two-level system) and v_r is the recoil velocity that represents the change of the atom's velocity by absorbing, or emitting, one photon with wave number k. The scattering force is illustrated in Fig 1.3. The atom is moving towards the laser, and each absorbed photon gives a kick to the atom in the direction that is opposite to the atom's movement. The scatted photons go in random directions, which results in a net force slowing the atom down. Thus the average effect of photon scattering is to slow the atom down. The Doppler effect shifts the laser frequency from ω to $\omega + kv$, so the frequency detuning is velocity dependent: $\delta = \omega - \omega_0 + kv$.

There are two techniques to compensate for the Doppler shift so that the laser light is resonant as the atoms slow down. The first one is called chirp cooling[16], which sweeps the laser frequency rapidly according to the Doppler shift. The second

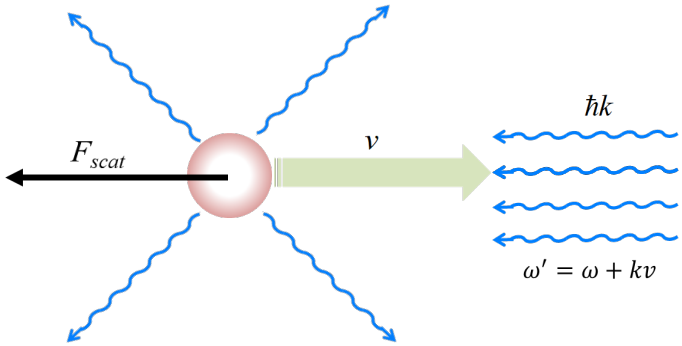


Figure 1.1: An atom moving at velocity v towards a counter-propagating laser beam with frequency ω absorbs photons and the energy is then spontaneously emitted by the excited atom.

one utilises the Zeeman effect from a tailored magnetic-field profile[59]. The Zeeman shift in a B-field is

$$\delta_B = \frac{g\mu_B B}{\hbar}, \tag{1.24}$$

where $g = g_{F'} M_{F'} - g_F M_F$ for a transition between the hyperfine levels $|F, M_F\rangle$ and $|F', M'_F\rangle$, g_F and $g_{F'}$ are the Landé factors, and $g \backsimeq 1$ for many laser cooling cases (μ_B is the Bohr magneton). The frequency detuning including both Doppler and Zeeman shifts is

$$\delta = \omega - \omega_0 + kv - \frac{g\mu_B B}{\hbar}, \tag{1.25}$$

This frequency detuning δ should stay close to zero to optimise the capture atoms (with initial velocity v_c) in a Zeeman slower, with either a tapered solenoid or permanent magnets[31]. By either way, a 25 cm-long Zeeman slower with beam intensity $I = I_{\text{sat}}$ has a theoretical capture velocity of $v_c = 500\,\text{m}\,\text{s}^{-1}$ for strontium atoms.

1.2.3 Optical molasses

As shown in Fig 1.2, an atom moving along the $z-$direction in a pair counter-propagating laser beams observes light at frequencies shifted to $\omega - kv$ and $\omega + kv$ for the two beams. We can write down the net force on the atom as

$$F_{\text{net}} = \frac{\hbar k\,\Gamma}{2}\left[\frac{I/I_{\text{sat}}}{1 + 2I/I_{\text{sat}} + 4(\delta_0 - kv)^2/\Gamma^2} - \frac{I/I_{\text{sat}}}{1 + 2I/I_{\text{sat}} + 4(\delta_0 + kv)^2/\Gamma^2}\right], \tag{1.26}$$

$$\backsimeq 4\hbar k^2 \frac{I}{I_{\text{sat}}} \frac{2\delta/\Gamma}{[1 + 2I/I_{\text{sat}} + (2\delta/\Gamma)^2]^2} \cdot v, \tag{1.27}$$

The term $2I/I_{\text{sat}}$ in the denominator accounts for the saturating effect of both laser beams, and eqn. (1.27) is derived by a first-order Taylor's expansion for small v. In

this approximation the net force F_{net} is linearly dependent on the velocity, as shown in Fig 1.3, and this technique for making a frictional force is named optical molasses[20].

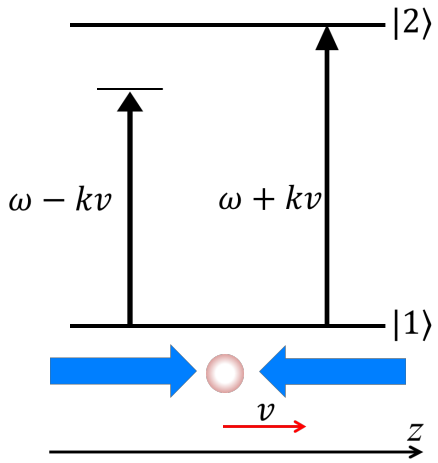


Figure 1.2: If an atom moves at velocity v, it will observe a Doppler shift $-kv$ for the beam towards right and $+kv$ shift for the beam towards left, which leads to a difference in the scattering force and a net force decelerating the atom.

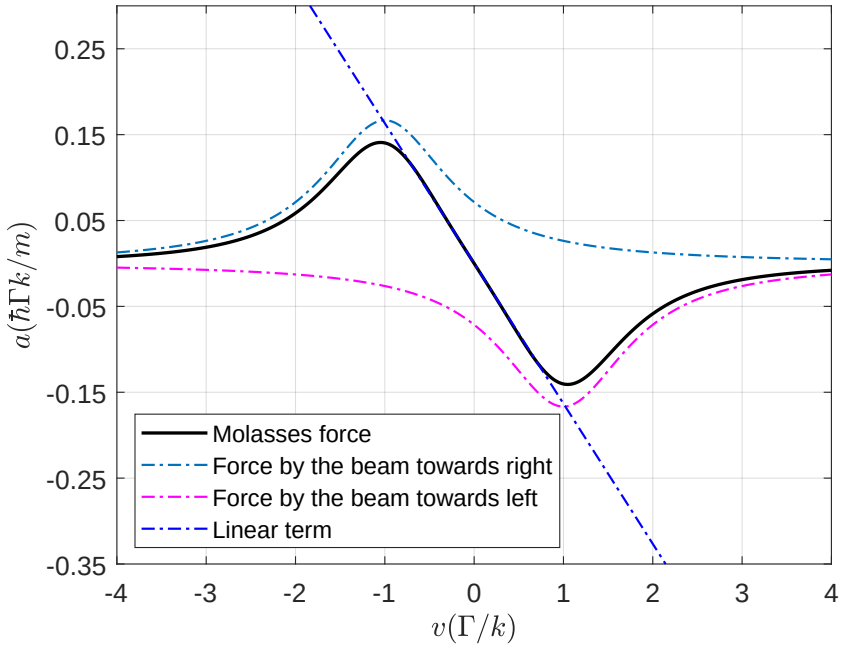


Figure 1.3: Acceleration (the axis a in the figure) caused by the molasses force is dependent on the velocity (the axis v in the figure) of the atom. The unit for the acceleration (a-axis) is $\hbar k\Gamma/m$ and the unit for the velocity (v-axis) is Γ/k, which are $a_u = 2 \times 10^6\,\mathrm{m\,s^{-2}}$ and $v_u = 15\,\mathrm{m\,s^{-1}}$ for the blue laser cooling transition. v_u is the widely-used estimation of the capture velocity.

1.2.4 The Doppler cooling limit

The Doppler cooling limit T_D which represents the lowest temperature that is predicted to be achieved with optical molasses technique for a $J = 0$ to 1 transition such as strontium, is written as

$$T_D = \frac{\hbar\Gamma}{2k_{\mathrm{B}}}. \tag{1.28}$$

There are 'sub-Doppler cooling methods' that produce atoms with temperatures lower than the Doppler limit, e.g. Sisyphus cooling. The fundamental limit of Sisyphus cooling is the recoil limit T_r, which refers to the energy gained by a static atom when spontaneously emitting one single photon. This corresponding recoil temperature is given by

$$k_{\mathrm{B}}T_r = \frac{\hbar^2k^2}{2M}. \tag{1.29}$$

The transitions of strontium are shown in Fig 1.7. For strontium's blue transition at 461 nm ($^1\mathrm{S}_0$ to $^1\mathrm{P}_1$), the Doppler limit is 0.8 mK and the recoil limit is 0.5 µK. For strontium's red transition at 689 nm ($^1\mathrm{S}_0$ to $^3\mathrm{P}_1$) both the Doppler limit and the recoil limit are the same value: 0.2 µK. Thus strontium can be laser cooled to a very low temperature in a short time (milliseconds), i.e. much more quickly than evaporative cooling. The metastable triplet level $^3\mathrm{P}_2$ is long-lived with lifetime $\tau \approx 500\,\mathrm{s}$[81], so atoms leaking into this $^3\mathrm{P}_2$ level are lost from the cooling cycle since experiments commonly last for only hundreds of milliseconds. The branching ratio into the $^1\mathrm{D}_2$ state is 2×10^{-5} (1:50000) and 1/3 of these leak into the dark state, so that atoms leak into the reservoir level at a rate $R_{scat}B_{br}$ where the effective branching ratio is $B_{br} = 6.6 \times 10^{-6}$. To boost the number of trapping atoms, atoms can be repumped (excited) from the $^3\mathrm{P}_2$ level to another level with a short lifetime so they can decay back to the ground level $^1\mathrm{S}_0$ and be involved in the cooling cycle again, however we did not have a laser available at the required wavelength.

1.2.5 The magneto-optical trap

With six laser beams constructing the light field for optical molasses, the velocity-dependent force slows atoms down in all three directions. Adding a quadrupole magnetic field, as shown in Fig 1.4, introduces a position-dependent force that pushes atoms towards the centre (field zero). This technique is called the magneto-optical trap (MOT). The energies of the Zeeman sub-levels as a function of position are shown in Fig 1.5, and the frequency detuning δ_B is

$$\delta_B = \frac{g\mu_B B'_z}{\hbar} z = \beta z, \tag{1.30}$$

where B'_z is the gradient of the magnetic field. The force for a pair of MOT beams can be written as

$$F_{\text{net}} = \frac{\hbar k\Gamma}{2}\Big[\frac{I/I_{\text{sat}}}{1 + C_s I/I_{\text{sat}} + 4(\delta_0 - kv - \beta z)^2/\Gamma^2} - \frac{I/I_{\text{sat}}}{1 + C_s I/I_{\text{sat}} + 4(\delta_0 + kv + \beta z)^2/\Gamma^2}\Big], \tag{1.31}$$

$$\backsimeq 4\hbar k^2 \frac{I}{I_{\text{sat}}} \frac{2\delta/\Gamma}{[1 + C_s I/I_{\text{sat}} + (2\delta/\Gamma)^2]^2} \cdot v + 4\hbar k\beta \frac{I}{I_{\text{sat}}} \frac{2\delta/\Gamma}{[1 + C_s I/I_{\text{sat}} + (2\delta/\Gamma)^2]^2} \cdot z, \tag{1.32}$$

where C_s accounts for the saturation effect of all six MOT beams and eqn. (1.32) comes from the Taylor expansion for small v and z. When $\delta < 0$, the scattering force will decelerate atoms and attract them towards $z = 0$. The polarisation of the MOT beams has to set according to the direction of local magnetic field as shown in Fig 1.4. The quadrupole coils are in the anti-Helmholtz layout, meaning that they are coaxial and have currents running through them in opposite directions. The four beams in the $x - y$ plane have the same handedness (as conventionally defined relative to their direction of propagation) while the beams along z axis have the other handedness. The convention of labelling polarisation relative to the local field direction does not work well in a MOT since the field direction reverses at the MOT centre. It is more common to label MOT beams as being $\sigma+$ or $\sigma-$ at all positions. A 2D MOT is formed from four beams, in the $x - y$ plane, and appropriate coils as shown in Fig 1.6. When used with a pushing laser beam along the z axis, this configuration is known as a $2D+$ MOT, which has been used as a deflector for strontium atoms in Ref [80] and a source of cold atoms in Ref [53].

There are various methods to realise the six beams for a MOT. The pyramid MOT takes advantage of reflections from prisms angled at 45° to constructs the light field from a single input laser beam, and an innovative design of pyramid MOT for Rb has recently been investigated in Oxford by Sean Ravenhall[61]. A pyramid MOT has been realised for ^{87}Sr[15], but the number of trapped atoms is only around 2×10^4, which is enough for an optical-lattice clock but not for atom interferometry. Also, specially-designed diffraction gratings can be used to reflect light at the appropriate angles to form a MOT[41] and this has been tested for Rb.

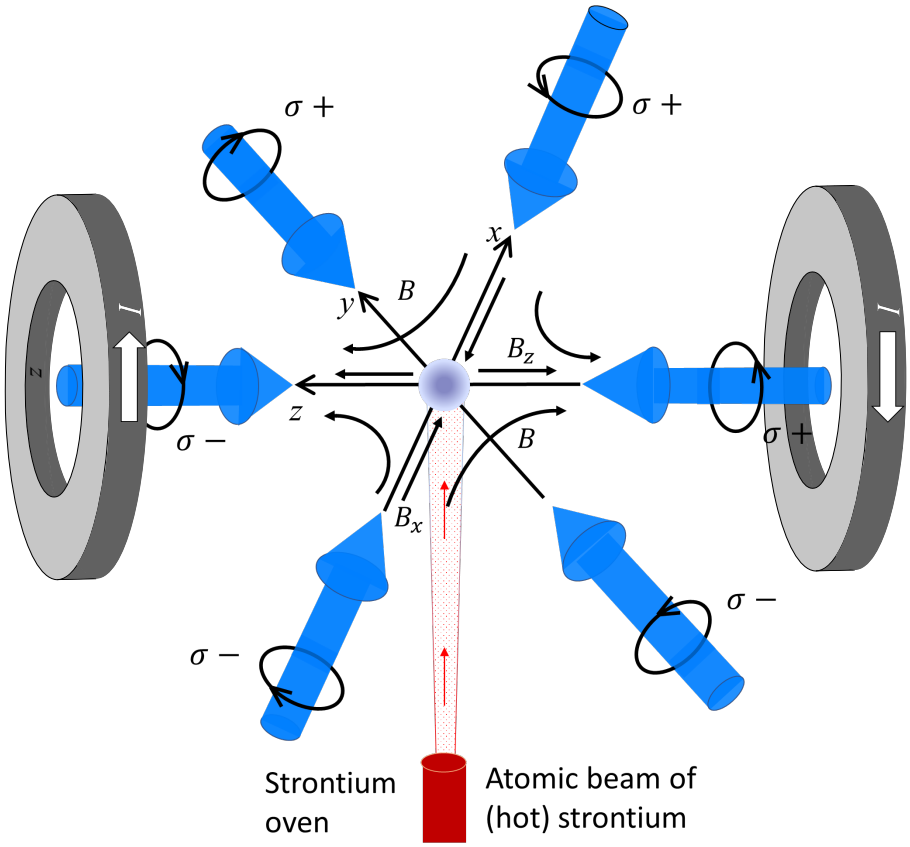


Figure 1.4: Atoms from the oven are slowed down and trapped in the MOT. The gradient of magnetic field is linear around the MOT centre and $B'_z = -2B'_x = -2B'_y$.

1.3 Properties of atomic strontium

This section focuses on explaining the beneficial features of strontium in laser cooling. Strontium has four stable isotopes with the following abundances: ^{84}Sr (0.56%), ^{86}Sr (9.86%),^{87}Sr (7.0) and ^{88}Sr (82.58%), whose properties are shown in Table 1.1. The even isotopes have zero nuclear spin and are bosonic (since the total electronic spin of the two electrons is an integer) whereas ^{87}Sr has nuclear spin $I = 9/2$ and this fermionic isotope has properties that are crucial for many applications, e.g. its lack of s-wave scattering and hyperfine structure[72]. The narrow optical transition $^1\mathrm{S}_0(F = 9/2) \rightarrow {}^3\mathrm{P}_0(F' = 9/2)$ of ^{87}Sr may permit sub-Doppler cooling to temperatures of tens of millikelvins in single step[79]. This transition is insensitive to external electromagnetic fields and cold-collision shifts. Transitions commonly used in ^{87}Sr and ^{88}Sr experiments are shown in Fig 1.7. A comparison of parameters involved in laser cooling is given in Table 1.2 for Na, Rb, ^{88}Sr and ^{87}Sr.

The advantages of strontium stem directly from the atomic structure of 'two-

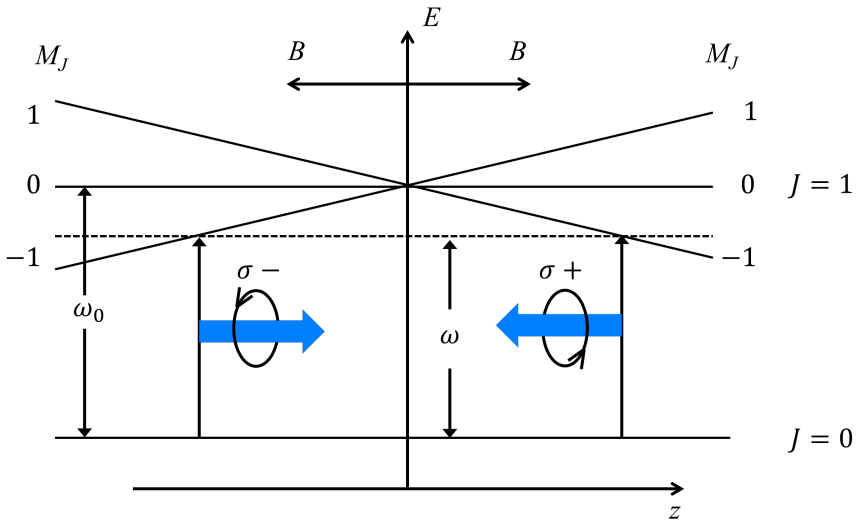


Figure 1.5: $\sigma+$ or $\sigma-$ label means that the beam drives the $\sigma+$ transition to $M_J = 1$ state or the $\sigma-$ transition to $M_J = -1$ state respectively. The molasses beam coming from the left shares the same handedness with that from the right-hand side, but the magnetic field direction is reversed, so they differ as to which transition they drive, and are therefore marked as $\sigma+$ and $\sigma-$.

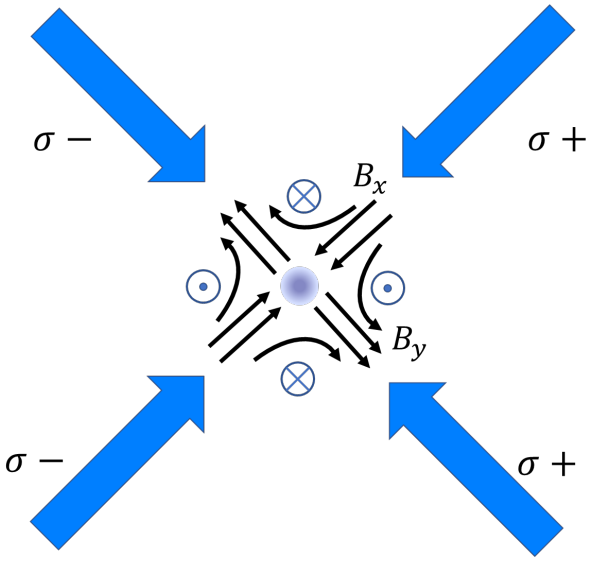


Figure 1.6: A schematic of a 2D MOT. The magnetic field coils are circles with a cross or dot in the middle representing opposite directions of currents (current along the z axis, into the paper, or opposite). The magnetic field stays zero along the z axis.

electron' systems, which have both strong transitions, that give rise to strong radiation forces (461 nm, used for blue MOT), which give rise to strong radiation forces and weaker transitions (689 nm, used for red MOT) that can be used for laser cooling

Isotopes	^{88}Sr	^{87}Sr	^{86}Sr	^{84}Sr
Abundance, %	82.6	7.0	9.9	0.6
Nuclear spin, I	0	9/2	0	0
Relative freq., /MHz	0	-51.9	-124.8	-270.8

Table 1.1: The isotopes of strontium used in cold-atom experiments are typically: ^{88}Sr, ^{87}Sr and ^{84}Sr. Frequency detuning are relative to ^{88}Sr.

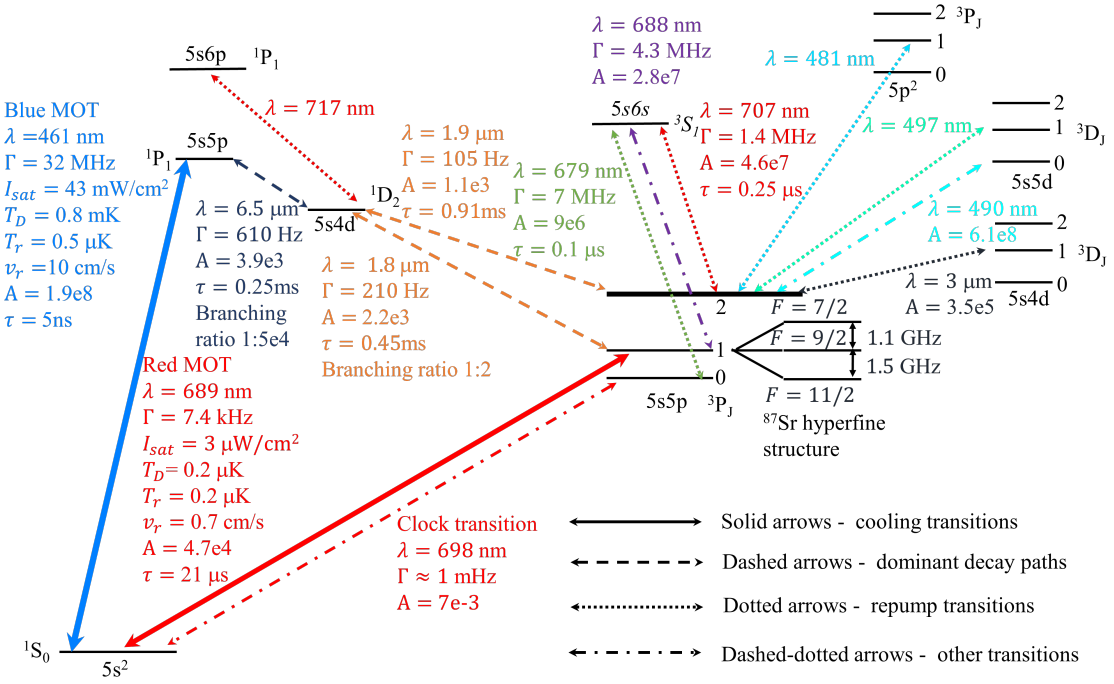


Figure 1.7: The transitions of strontium with other atomic data. Laser cooling transitions are shown with solid arrows, dominant decay paths with dashed arrows, repump transitions with dotted arrows and other transitions with dashed-dotted arrows. For ^{87}Sr there is hyperfine structure. The long-lived $^3P_2$ reservoir state is marked with longer and thicker line. Ref [53] reported an order of magnitude increase of the atom number with 481 nm repumping light. τ refers to the lifetime in the upper level of the transitions [43, 15, 80, 6, 53, 71].

to much lower temperatures because of their narrow linewidth. The strong and weak transitions of strontium are used for two-stage laser cooling which allows low temperatures to be reached very quickly (tens of milliseconds), as compared to methods such as evaporative cooling used for alkalis. In this way, ultracold samples of strontium can be produced that are almost quantum degenerate and require only a small amount of further cooling to reach BEC. This method was pioneered by Professor Florian Schreck[73]. The rapid production of cold dense samples is very useful for interferometers especially those are being designed for fundamental physics experiments, such

Isotope	Na	^{87}Rb	^{87}Sr	^{87}Sr
Transition	$^2S_{1/2}-^2P_{3/2}$	$^2S_{1/2}-^2P_{3/2}$	$^1S_0-^1P_1$	$^1S_0-^3P_1$
M/kg	0.38×10^{-25}	1.44×10^{-25}	1.44×10^{-25}	1.44×10^{-25}
λ/nm	589	780	461	689
τ/ns	16	26	5	2.2×10^4
Γ/MHz	9.8	6.1	32	7.4×10^{-3}
$I_{\rm sat}$/mW cm^{-2}	6.26	1.67	42.5	0.003
a_{max}/m s^{-2}	9.1×10^5	1.1×10^5	1.0×10^6	1.6×10^2

Table 1.2: A comparison of the parameters involved in laser cooling of Na, Rb, ^{88}Sr and ^{87}Sr[70, 69, 80]. The maximum deceleration is very similar for Sr and Na, both being 10 times that for Rb. The intercombination line of Sr is weak but cools atoms to temperatures of a few microkelvins because of its narrow linewidth (long lifetime).

as Ref [30] at Stanford University.

Cold-atom experiments all start by generating a thermal atomic vapour, but the temperature required varies greatly from element to element. There are two main ways of generating thermal gases for alkalis and alkali-earth-metals. The first way is to heat a chamber containing a sample of the material to create a hot vapour with higher pressure inside than that in the surrounding vacuum region. The hot vapour then shoots out of the chamber through a hole to form a thermal atomic beam. The atomic flux is determined by the vapour pressure inside the oven, which is depends on the oven temperature. Typically such ovens contain several grams of metal, which provides a long time between reloading. An alternative way is to use dispensers which contain chemical compounds in a heated metal tube, and which release a few milligrams of metal over their lifetime. The release rate depends on the temperature of the dispenser, which is controlled by the current applied through. Dispensers are suitable for a compact design, but they have a short lifetime, compared with an oven, which is particularly limiting for the high fluxes that we requie.

Some physical properties of Sr, Na and Rb are listed in Table.1.3. Strontium has a higher melting and boiling point than the other two elements and it requires a higher temperature to reach a vapour pressure of 1.3×10^{-2} mbar. The common practice in strontium experiments is to use an oven with a temperature of at least 450 °C to sustain an adequate atomic flux. Dispensers can however be used for spectroscopy purposes, since this only requires a vapour pressure of around $\sim10^{-7}$ mbar[17]. Rubidium

and caesium have a sufficient vapour pressure at room temperature for experiments and alkali-metal dispensers can give a pressure of $10^{-4} \sim 10^{-3}$ mbar (1×10^{-2} mm mercury), which is used as a standard reference pressure in Ross' paper on metal atom beam sources[62].

Element	Melting point(°C)	Boiling point(°C)	Temperature for vap. press. of 1.33×10^{-2} mbar (°C)
Strontium	769	1384	530
Ytterbium	819	1194	470
Sodium	98	883	290
Rubidium	39	688	175
Caesium	28	669	150
Lithium	180	1330	535

Table 1.3: Data for the elements commonly used in laser-cooled atom experiments. More elements are listed in Ref [62].

Experiments with the heavier alkali metals can be carried out with a vacuum cell and alkali metal dispensers, but this is not generally used for strontium because of the high temperature required; early work at JILA[79] used a strontium vapour but this was later replaced by an atomic beam.

1.3.1 Difference between the isotopes ^{87}Sr and ^{88}Sr

This section presents a comparison between the two isotopes ^{87}Sr and ^{88}Sr in their atomic structures and scattering lengths, which lead to their special benefits and drawbacks for applications such as lattice clocks and interferometers. Strontium has an atomic number $Z = 38$. Among the four stable isotopes in Nature, ^{88}Sr, ^{86}Sr and ^{84}Sr are bosons with zero nuclear spin, and ^{87}Sr(fermion) has a nuclear spin of $I = 9/2$, which leads to hyperfine structure. In the ground electronic configuration of strontium the two valence electrons are paired to give a singlet term $^1S_0$. This has zero contribution to the magnetic moment from the electrons, and for the even isotopes there is no nuclear magnetic moment either. Thus the even isotopes are insensitive to external magnetic fields. This feature is very useful for high precision measurement experiments as it requires less magnetic shielding compared with experiments with alkali atoms (which have a magnetic moment equal to 1 Bohr magneton). The fermionic isotope ^{87}Sr has a magnetic moment contributed solely by the nuclear spin (in the electronic ground level), which is much smaller compared with that for alkali atoms, whose magnetic moments are mainly from the electron (that ratio of

the Bohr and nuclear magnetons is $m_p/m_e = 1836$, m_p is the mass of the proton and m_e is the mass of the electron).

The structure of many-electron atoms, such as strontium, can be explained by a succession of approximations. The Coulomb interaction of the electrons with the nucleus and most of the electron-electron repulsion is accounted for by the so-called Central Field approximation, in the electrons experience a radial potential that conserves the angular momentum of each individual electron. The eigenstates of the atom are electronic configurations which are labeled by a list of the principal and orbital angular momentum quantum numbers. This gives a complete description of the ground configuration of Sr. For low-lying configurations in which one of the valence electrons is excited the residual electrostatic interaction, i.e. the part of the electron-electron repulsion left over from the CF, is the dominant interaction, and leads to eigenstates described by the LS-coupling scheme, for example, the $^1\mathrm{P}_1$ and $^3\mathrm{P}_J$ terms. Central Field approximation corrected with extra Hamiltonian terms for perturbations, we can find solutions for the atomic structures of strontium atoms in a hierarchy of interactions in decreasing strength: Central Field, residual electrostatic, spin-orbit, hyperfine structures. Those states are specified by quantum numbers n, l, S, I, J and can be written in the following notion for an energy level:

$$n_1 l_1 n_2 l_2 \cdots {}^{2S+1}L_J,$$

where the list of principal quantum numbers n and angular momentum quantum numbers l specify a Central Field configuration as $n_1 l_1 n_2 l_2 \cdots$, S is the total spin angular momentum, L is the total orbital angular momentum and J is total angular momentum quantum number. For example, the ground electronic configuration of strontium is $5\mathrm{s}^1\mathrm{S}_0$.

According to the orientations of spins of two valence electrons (described by S), there are two kinds of energy levels: singlet (spins in anti-parallel orientations) and triplet state (spins in parallel orientations). The transition between singlet and triplet states are forbidden by the selection rules, but the rule is partially broken down by the spin-orbit coupling, which contributes to the narrow intercombination transitions. Two important cooling transitions used for laser cooling of strontium are the 461 nm (the blue cooling transition) for $^1\mathrm{S}_0$-$^1\mathrm{P}_1$ and the 689 nm (the red cooling transition) for $^1\mathrm{S}_0$-$^3\mathrm{P}_1$. Atoms excited from the ground state $5\mathrm{s}^1\mathrm{S}_0$ to the $5\mathrm{s}5\mathrm{p}^1\mathrm{P}_1$ state can decay into the $5\mathrm{s}4\mathrm{d}^1\mathrm{D}_2$ state and then further decay into two of the triplet states: $5\mathrm{s}5\mathrm{p}^3\mathrm{P}_1$ and $5\mathrm{s}5\mathrm{p}^3\mathrm{P}_2$. The $^3\mathrm{P}_1$ state decays to the ground state with a lifetime around 0.1 ms, while the $^3\mathrm{P}_2$ state is metastable with a lifetime of two hours, which requires

repumping to close the cycle. The $5s5p^3P_0$ state is the extremely long lived "clock" state and the transition from $^1S_0$ ground state to the $^3P_0$ state is commonly referred as the "clock" transition. This $J = 0$ to $J = 0$ transition is strongly forbidden in ^{88}Sr, but slightly permitted in ^{87}Sr with a lifetime of several hours because of the hyperfine interaction. As ^{87}Sr has a non-zero nuclear spin $I = 9/2$, each energy level $^{2S+1}L_J$ will split into $2J + 1$ sublevels e.g. the $^3P_1$ gives rise to three hyperfine levels with total angular momentum quantum number $F = 7/2$, $9/2$ and $11/2$. An external magnetic field splits each of these into $2F + 1$ states. Levels with $J = 0$ have $F = 9/2$ e.g. the ground state $^1S_0$ and the clock state $^3P_0$. The hyperfine interaction, between the nuclear magnetic moment and the magnetic field that the electrons create at the position of the nucleus, causes a small amplitude of the $^3P_1$ wave function to be admixed into the $^3P_0$ wave function. The amplitude equals the matrix element of the hyperfine interaction between the levels over their energy separation, which is small but nonzero. That is why ^{87}Sr must be used for optical lattice clocks, even it is less abundant.

One important feature of ^{88}Sr is that it has an extremely small scattering length, so a cold cloud of ^{88}Sr atoms can be treated as a system of non-interacting particles[46]. Lack of cold collisions contributes to the absence of decoherence. Although small scattering length is not good for evaporative cooling, ^{88}Sr can reach Bose-Einstein condensation by sympathetic cooling[20]. Compared with ^{88}Sr, hyperfine structures in ^{87}Sr add complexity to the laser cooling and trapping of ^{87}Sr atoms and ^{87}Sr is less abundant, which make ^{88}Sr a better choice in experiments for interferometers and quantum degenerate gases.

1.3.2 Applications of strontium

Cold strontium atoms have important applications in physics and precision measurements, especially high-precision frequency metrology[44, 11] as well as force sensing at the micrometer scale [68]. Strontium is also important for matter-wave interferometry and experiments with degenerate quantum gases. Optical-lattice clocks using strontium are among the most precise time-keeping devices in the world[82, 51].

Currently atomic clocks use microwave transitions between hyperfine levels of ground electronic configuration of caesium, as the basis for the primary standards of time throughout the world. However, clocks using narrow optical transitions can have a much higher Q-factor than a microwave clock. Alkali metals do not provide optical transitions that are as narrow as in strontium, therefore it is expected that optical-lattice clocks, or trapped ions based on strontium or similar species, will eventually

replace atomic fountain clocks as the primary time standards. Strontium optical-lattice clocks are suitable for transportable clocks since they can be compact and less sensitive to orientation than atomic fountains.

When it comes to interferometry, strontium makes it possible to produce an atomic beam with a high flux and low temperature that is very suitable, in particular for new schemes in which beam splitting of the matter waves uses narrow single-photon transitions rather than the Raman (two-photon) transitions used in current work with alkalis. The lack of s-wave collisions between quantum degenerate fermions reduces the perturbation in both interferometers and optical clocks because of Pauli blocking[50].

There is research on strontium[72], or mixtures of strontium with other species[56] to study interacting quantum systems. The bosonic isotopes of strontium lack electronic and nuclear spin in the ground state thus simplifying resonant photon-scattering phenomena to Rayleigh scattering (with no Raman scattering), and so bosonic isotopes are used for experiments on coherent backscattering [9] and the investigation of phase-breaking mechanisms in the multiple-scattering regime[19]. In conclusion, there is great current interest in strontium and it is currently regarded as a good workhorse for atomic clocks, matter-wave interferometry and fundamental studies of ultracold quantum matter.

1.4 Motivation and research gap

Laser cooling of strontium towards quantum degeneracy involves multiple stages: an oven generating an atomic beam, transverse collimation by optical molasses, Zeeman slowing, collecting atoms in a blue 3D MOT, loading into a red MOT and further sub-Doppler cooling techniques. The number of atoms is reduced at each stage, so the initial loading rate (into blue MOT) is a key characteristic for many applications. A high loading rate can shorten the loading time of a MOT, decrease the duty cycle in optical-lattice clocks, minimise the Dicke effect[23] and increase the number of atoms in samples of degenerate quantum gases. A recently published paper[80] reports the demonstration of a high-flux source of cold strontium atoms with a loading rate of $6 \times 10^9\,\mathrm{s}^{-1}$, but uses a large and complicated apparatus. Zeeman slowers are widely used for strontium and sodium experiments. A commercially available source (AOSense, US) is well engineered to minimise its size, with a length of 25 cm, but it is very expensive.

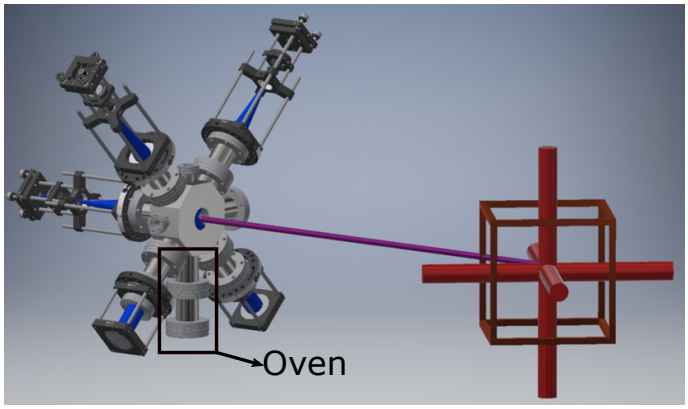
There are numerous proposals to make transportable strontium-based cold-atom instruments including for space-based applications, such as the ongoing project on Space Optical Clock project[14]. This prompted us to consider how to make a source of cold strontium atoms that is more compact, but which still has a high loading rate of cold strontium atoms. The cost, size and complexity drawbacks of using a Zeeman slower and the trial of using a 2D MOT in sodium done by Ref [40] inspired our design of a smaller high-flux source of cold strontium atoms that uses a 2D MOT instead of a Zeeman slower. Two-dimensional MOTs are widely used as sources of cold potassium, rubidium and caesium, while Zeeman slowers are widely used for strontium and sodium experiments, where atomic beams are usually produced by effusion of atoms from an oven. A novel method using a 2D MOT configuration was demonstrated for sodium by Lamporesi *et. al.* , Trento, Italy[40], which we refer to as the Italian design in the following. The key feature of the Italian design was an arrangement of laser beams and magnetic field gradient equivalent to a combination of a short Zeeman slower and 2D MOT, so that there was no line of sight from oven to the final scientific chamber. It was verified that this compact 2D MOT method gives similar results to a traditional Zeeman slower in experiments carried out by the team of Professor Vanderlei Bagnato, in Sao Paulo[58] by direct comparison of both methods on the same apparatus. They added the Italian design to their existing apparatus for Zeeman slowing sodium atoms and measured the loading rate and the number of atoms in the final 3D MOT for each approach. This direct comparison in the same apparatus showed that a 2D MOT provides a flux of atoms comparable with that from a Zeeman slower.

1.4.1 Our design

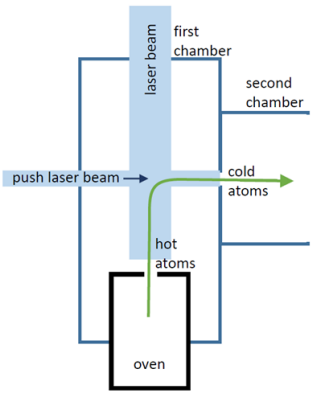
We set out to adapt the Italian design for experiments with strontium since it has been demonstrated to work for sodium. The proposed design (Fig 1.8) is a compact source of cold strontium atoms using a two-dimensional magneto-optical trap (MOT) with a 'push' laser beam (a 2D+ MOT), avoiding the usage of a Zeeman slower completely by directly trapping atoms in a MOT. The 2D+ MOT replaces the transverse optical molasses and Zeeman slower[3].

A more detailed introduction to each component used in Fig 1.8 is presented in Chapter 2. The advantages of the proposed scheme include:

[3]Our solution using a MOT for direct trapping of strontium atoms is similar to that reported in Ref [53], but we independently proposed and started the experiment in January 2016.



(a) Proposed 2D+ MOT scheme



(b) Side view

Figure 1.8: (a) Atoms are launched upwards into the 2D MOT. Decelerated atoms are pushed out into a science chamber (represented by three red MOT beams)(b) The 2D MOT deflects and decelerates atoms and the push beam directs the cooled atoms horizontally. There is no optics in direct line of sight to the oven so we avoid the strontium coating problem.

1. Uncooled atoms, including unwanted isotopes, do not enter the science chamber.
2. The flux of cold atoms into the science chamber can be switched off.
3. The length of the source is reduced to 24 cm.
4. No optics are in direct line of sight to the oven so coating is avoided.

As the capture velocity for a MOT is $\sim 20\,\mathrm{m\,s^{-1}}$ (with $\delta = -\Gamma$) is much lower than that for Zeeman slower $> 150\,\mathrm{m\,s^{-1}}$, a high flux of thermal atoms is required from the oven. A simple design of the atomic oven is presented in Chapter 2 with other parts of our apparatus and characterised in Chapter 3.

To control the frequency of the laser system we developed a novel technique, Zeeman-tunable modulation transfer spectroscopy, which gives stable operation and allows testing to find the best set of parameters for direct trapping of strontium atoms.

Chapter 2

Apparatus: oven and vacuum system

Neutral atoms traveling through vacuum are good platforms for many studies and ever since the early days of atomic physics, ovens have been used to produce atomic beams[62], such as the seminal work of Stern and Gerlach[28]. Nowadays, neutral beams are an important feature of many cold atom experiments[20].

The principles for the production of most atomic beams are broadly similar for many metallic elements. Traditionally the source material is heated in an enclosed volume and vaporised atoms are allowed to effuse through a small hole into a vacuum region, as shown in Fig 2.1; here, 'small' means that the flux of atoms leaving does not significantly reduce the vapour pressure inside the oven. However, the design of the container (oven body), opening (nozzle), heating element and required temperature vary greatly among different substances.

The oven presented in this chapter has been designed to provide a high flux of the alkaline-earth metal strontium which must be heated to $>450\,^{\circ}\mathrm{C}$ to achieve a sufficient vapour pressure (Table 1.3). This is similar to experiments with the alkali metal sodium, but in contrast to experiments with heavy alkalis such as rubidium, for which the use of dispensers is common. Heated dispensers have been used for spectroscopy of strontium but they achieve only low vapour pressures, e.g. 10^{-7} mbar[17]), which is not sufficient for our purpose of ultimately producing a high-flux source of laser-cooled strontium atoms.

Although direct loading of a MOT from an oven was used in early work on strontium at JILA, it proved to be complicated for several reasons, including the frequency shifts and other deleterious effects arising from the black-body radiation[1] at high temperatures [79]. In this work we show that with careful attention to details, it is

[1] which are bad for optical-lattice clocks

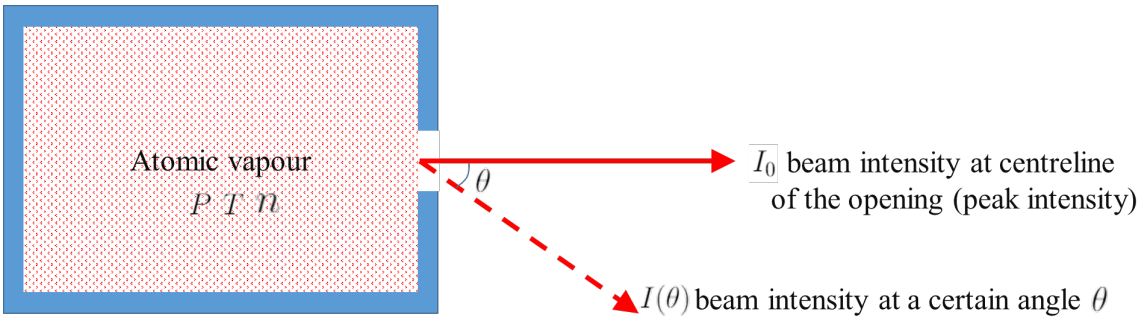


Figure 2.1: A simple model of the atomic oven is an enclosed volume containing hot vapour and atoms effuse out of the oven through an aperture in an infinitely thin wall. The principle of operation of a simple atomic beam source is that atoms pass through a small opening in a container enclosing a sample of the metal. The vapour is characterised by the quantities pressure P, temperature T and density n.

straightforward to make a compact atomic beam of strontium. Another approach has been tested recently at Birmingham University[38] is the laser ablation of strontium, or strontium oxide, to produce puffs of vapour; this has been used to load small numbers of atoms into a magneto-optical trap but has not yet been fully developed.

2.1 Survey of previous oven designs

This chapter focuses on the design and analysis of a strontium atomic oven and how this affects the flux and collimation of the atomic beam. Before embarking on the design of our compact strontium oven, we surveyed the strengths and drawbacks of existing approaches.

2.1.1 A simple source: an externally heated tube

The simplest oven design is to put a heater around a metal tube, where the tube is part of a standard stainless steel vacuum apparatus. This is the approach used in the recent work at USTC, China[53], as shown in Fig 2.2. The overall design of that apparatus has strong similarities to what we planned independently at the start of this project, in 2015, but fortuitously we focused our efforts on complementary aspects such as optimising the oven design. This basic oven has an aperture of 16mm diameter, without any further means of collimation, which places a severe limitation on the flux of the laser-cooled strontium source using this oven. The lack of directionality is wasteful and so the oven temperature was operated below 510 °C to conserve the strontium supply even though the oven holds around 5 g of metal. Furthermore, this

type of design puts a considerable amount of heat into the surroundings which is undesirable near optical systems.

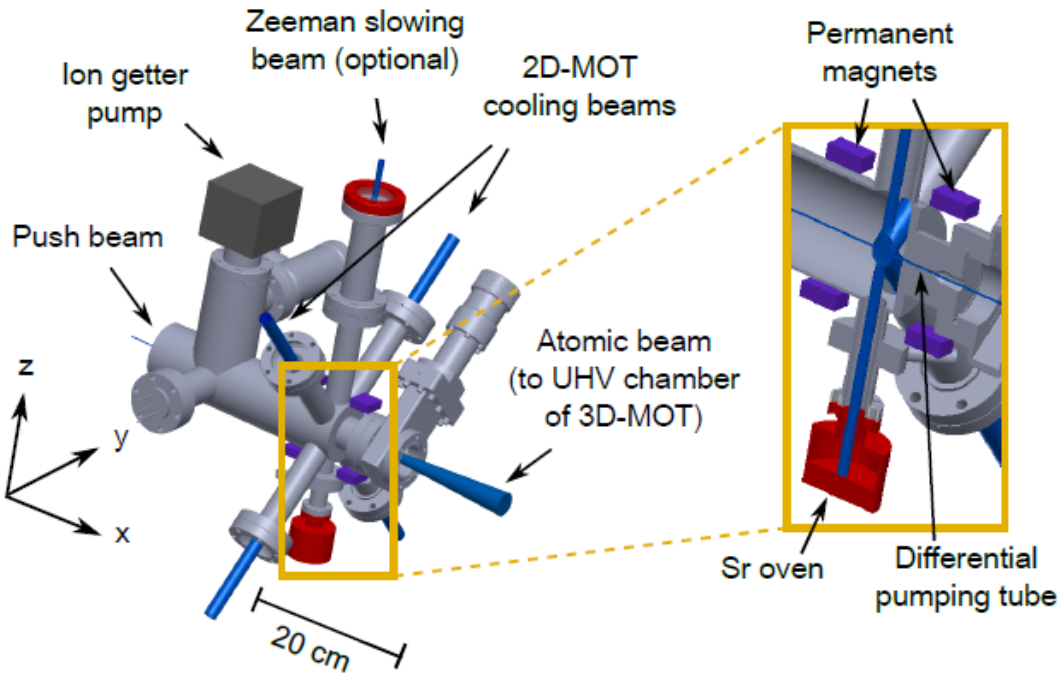


Figure 2.2: The strontium vapour source in the apparatus at the USTC, China, is an externally heated tube, shown as the red tube at the bottom of the picture taken from Ref [53].

2.1.2 A traditional atomic oven with in-vacuum heaters

The oven shown in 2.3 is a complicated design taken from [64], and that paper gives a clear exposition of the design considerations for traditional ovens. This oven is mounted on a conflat flange (standard DN40) and it is heated in a vacuum environment with tantalum wires threaded through an alumina tube. There is no heat convection because the heating element is in vacuum, but does require the designing of electrical vacuum feedthroughs (which adds to the cost). The thermal shield is aluminum which limits the maximum working temperature to under 660 °C. To collimate the output, the nozzle consists of many steel capillaries, which reduces the solid angle over which an atom may effuse from the oven. More detailed discussions about reasons for using array capillaries can be found in Sec 2.3. Overall this oven has a lot of complexity and many small components.

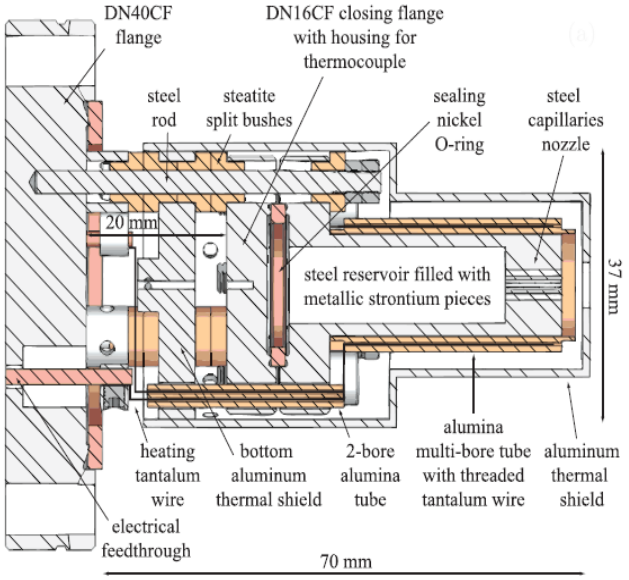


Figure 2.3: This figure presents an overview of the oven designed by Tino's group[64].

2.1.3 Previous re-entrant oven design

The re-entrant design shown in Fig 2.4 represents a good compromise between simple constructions and efficient operations. This design was developed for strontium by the team of Professor Killian at the Rice University, Texas, and is described in the thesis of Camargo[18]. This provided inspirations for our design. Note that only one of the heaters is outside the vacuum and there are several electrical feedthroughs for heaters and thermocouples which are not shown in the figure. It has two independent heaters on the oven to maintain an adequate temperature difference (50 °C) or more [80]) between the nozzle and the bottom of the strontium reservoir. This is done to prevent clogging of the nozzle, although it is not clear whether this is folklore or fact. Blocking of exit tubes is less likely a problem with strontium metal than for other species since it sublimes, so there is no liquid metal that can flow into gaps (however this is not proven). This strontium oven is also mounted on a CF40 flange. The multi-channel nozzle is made of hypodermic needles tightly packed with smaller diameter needles filling in excess space.

2.2 Our re-entrant oven design

The design details of a simple and efficient high-flux oven are presented in this section. We have made two prototypes: one manufactured by a local engineering company

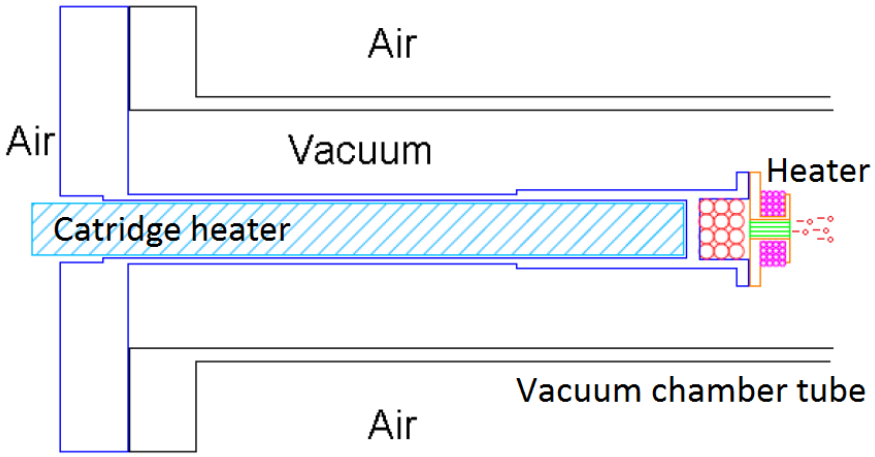


Figure 2.4: A re-entrant oven design adapted from Camargo's thesis[18]. A cartridge heater rod is pushed towards the bottom of a strontium reservoir and a coil heater is wrapped around the multi-channel nozzle.

(Prototech), and the other one is a simplified version that was made in the Oxford Physics Workshop.

2.2.1 Oven body

Our oven design has no electrical feedthroughs into the vacuum but instead, it uses six heaters inserted from the back of the oven. In these customised cartridge heaters, the hot element is localised near the tip. Heats are close to the nozzle to form a temperature difference between the nozzle and strontium reservoir. Thermocouples used to stabilise the temperature of the oven were installed in the same way. There are no other heaters or wires placed in the vacuum. Another innovative aspect of the design is the usage of a graphite nozzle which is simple to assemble. In principle the nozzle can be removed for refilling of the oven. We chose graphite for manufacturing our nozzles, which is much softer than stainless steel, and thus favourable for machining (more details in Sec 2.2.2).

Fig 2.6a shows the CAD model for the oven manufactured by Prototech. The delivered product is shown in Fig 2.6b and the black cap on the top is one version of the graphite multi-channel nozzle. In Fig 2.6a, six drilled holes (red) equally spaced in one circle are 4 mm diameter holes for heaters and the other two holes (blue) are for the thermocouples. The thermocouple holes are of are of different depth, so that one thermocouple can reach the nozzle part, and the other measures the temperature at the bottom of the strontium reservoir. The main body is joined to the flange by a thin tube to reduce heat conduction. The total length is 112.7 mm (including

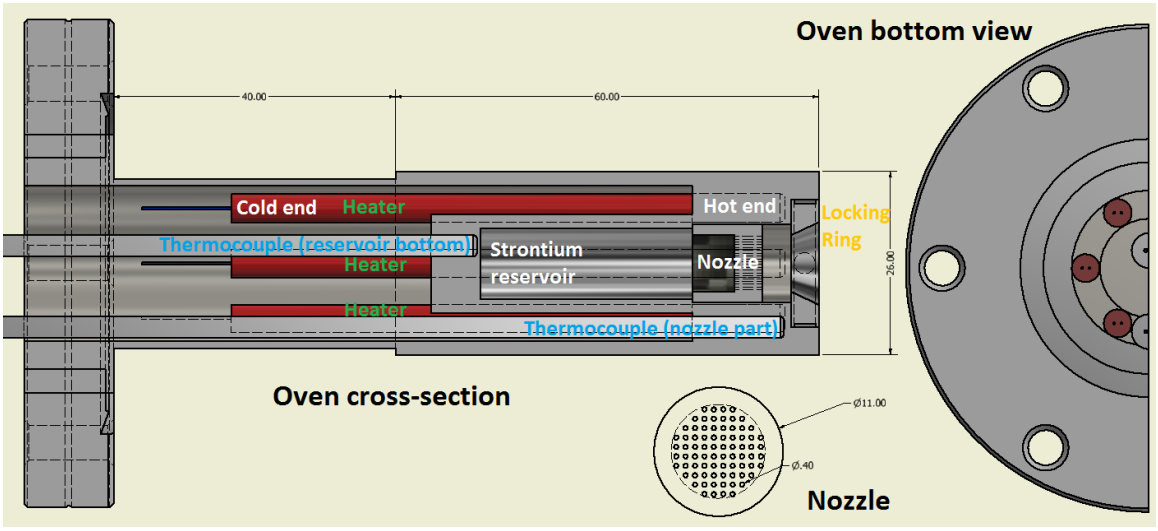


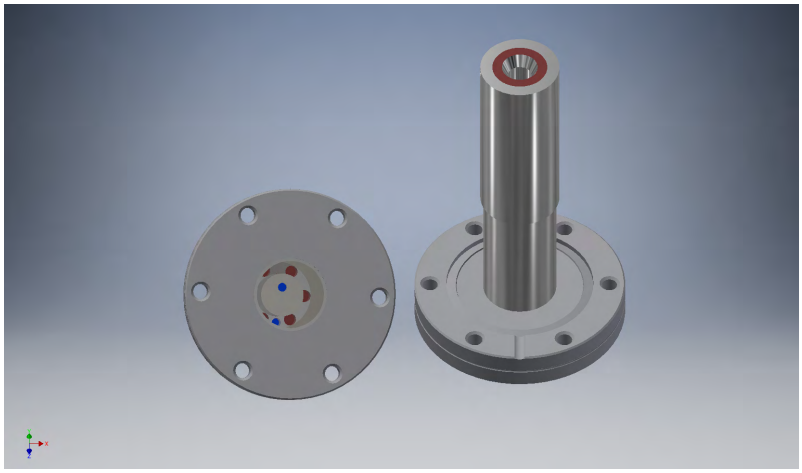
Figure 2.5: Our re-entrant oven design

the CF40 flange) and the outer diameter of the oven is 26 mm (24 mm for the thin wall section). Future designs could decrease the width of the thin section to further decrease conduction, although the current prototype performs well.

The six heaters are evenly distributed so that the temperature across the oven is approximately cylindrically symmetric. Detailed information about heaters and thermocouples can be found in Sec 2.4. Each heater has a hot end and a cold end. The cold end is connected with electrical leads, while the hot end is in contact with the top part of oven body, where the nozzle is held. This feature of the design leads to a large temperature gradient between nozzle and bottom of the oven. There is another 3.3mm hole at the bottom of the oven for a second thermocouple, which allows us to measure the temperature difference from top to bottom of oven.

The design of the oven made in the Oxford Physics Department workshop was simplified to reduce the machining difficulties. The Prototech oven is made of two pieces welded together: the strontium reservoir and a thin-wall connection tube. We originally suggested machining the whole oven from one piece of stainless steel but it is difficult to source 3 mm and 4 mm drill bits long enough to bore the required holes (and also difficult to drill long straight holes). The workshop oven is intended for spectroscopy at a lower temperature ($350 - 400°C$) than that for a MOT, so there is less need to reduce the heat conduction out of the oven and a shorter tube is sufficient. The total length is cut down to 90 mm (including the CF40 flange) and the outer diameter is 26 mm.

The CAD model of the workshop oven is shown in Fig 2.6d and a photograph of the final device is shown in Fig 2.6c. Products from the workshop were cleaned



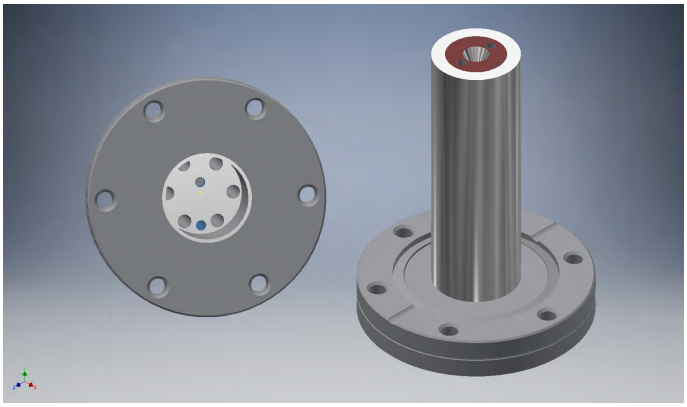
(a) Prototech oven CAD model



(b) Prototech oven



(c) Workshop oven



(d) Workshop oven CAD model

Figure 2.6: The CAD model and pictures of the two ovens that were tested. (a) shows the CAD model for the oven from Prototech, which has a thin waist connecting the top strontium reservoir and the flange. (b) a picture of the delivered Prototech oven. The black cap on the top is one of the graphite nozzles. (C) is the oven machined by Oxford Physics workshop. (d) is the CAD model for the Workshop oven, which does not have a thin joining tube and the length is shorter than the Prototech oven because of the limited depth of hole that could be drilled in the workshop.

thoroughly before being put in the chamber, to remove any oil residues (first washed in an ultrasonic bath with a 1:9 mixture of neutracon detergent and water, followed by a second bath in high-grade acetone).

2.2.2 Nozzle

There are many possible nozzle designs for atomic ovens. A simple hole is adequate in some cases, however the common practice is to have an array of parallel holes, or channels, to give a high flux whilst collimating the atomic beam. The theoretical treatment of the atomic flux out of a single channel, or aperture, is presented in Sec 2.3, but in practice it typically takes trial and iteration to manufacture. We had several different types of nozzle manufactured for testing: three multi-channel graphite nozzles: nozzle A (Prototech, shown in Fig 2.7a), nozzle B (Fig 2.7b) and nozzle C (Fig 2.7c) and two simple stainless steel nozzles (Oxford Physics mechanical workshop shown in Fig 2.8a and Fig 2.8b). The graphite nozzles are fragile and must be handled with care.

The nozzles made in the Oxford Physics workshop have a stainless steel cap with a hole drilled in the middle: nozzle 1 has a 4 mm diameter hole and nozzle 2 has a 1 mm diameter hole, as shown in Figs. 2.8a and 2.8b respectively. The depth of the hole is 10 mm in both nozzles. Nozzle 1 was installed on the workshop oven, shown in Fig 2.6c. Nozzle 2 gives better collimation, but reduced total flux.

2.3 Atomic flux calculation

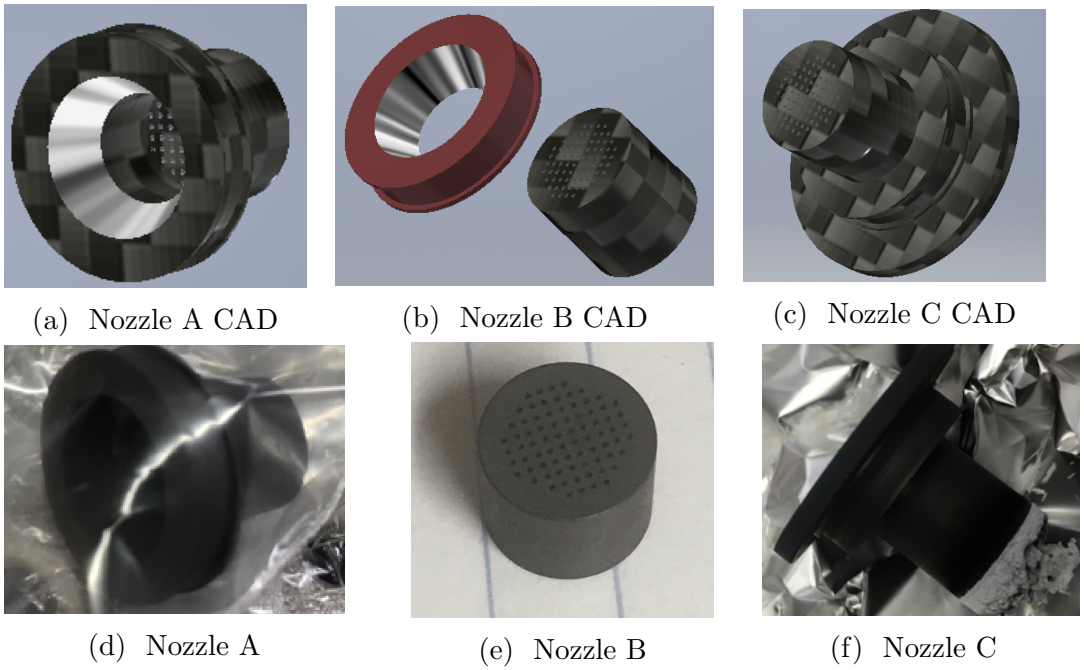
To select between various choices of nozzle design, requires understanding how the geometry of the nozzle affects the total atomic flux and its collimation, when there is a hot vapour of strontium atoms at the input end of the channels.

2.3.1 Velocity distribution

Atoms enclosed in a volume, as shown in Fig 2.1, with pressure P and temperature T, have a velocity distribution described by[57]

$$f(v) = \frac{4v^2}{\sqrt{\pi} v_p^3} \exp\left(-\frac{v^2}{v_p^2}\right), \tag{2.1}$$

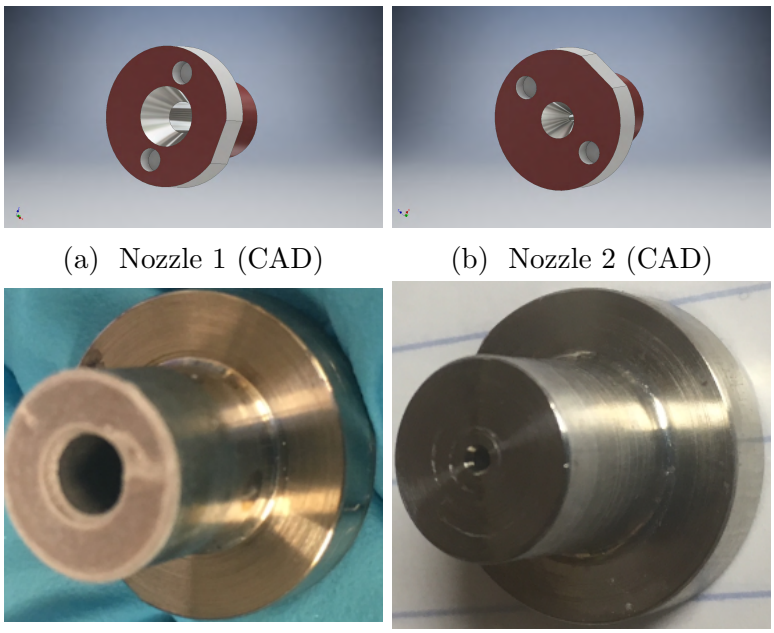
where $v_p = \sqrt{2k_B T/m}$ is the most probable speed in the gas, k_B is Boltzmann's constant, and m is the mass of the atom. The root mean squared velocity of atoms in this case is



(a) Nozzle A CAD (b) Nozzle B CAD (c) Nozzle C CAD

(d) Nozzle A (e) Nozzle B (f) Nozzle C

Figure 2.7: The CAD models and pictures of graphite nozzles machined by Prototech. All three nozzles share the cylindrical part, which has 76 holes of 0.4 mm diameter, collimating the beam. All are machined from a single piece of graphite. Nozzle A shown in (a) and (d) has a slotted cap, which is made on the same piece of graphite with the cylindrical array of capillaries. Nozzle B shown in (b) and (e) consists of two parts: the cylindrical array of capillaries and one slotted locking ring to secure the position of the cylinder. Nozzle C shown in (c) and (f) shares similar structure to Nozzle A in its cylindrical structure with small-bore holes drilled out. The major feature of Nozzle C is its locking cap, which increases the surface area of the nozzle and contributes to a larger heat loss by radiation; this nozzle's temperature increases more slowly than others, for the same heater power, and it clogged once because of a too rapid heating procedure, as shown in (f). The white powder shown in the image is strontium oxide.



(a) Nozzle 1 (CAD) (b) Nozzle 2 (CAD)

(c) Nozzle 1 (d) Nozzle 2

Figure 2.8: The CAD models and pictures for the stainless steel nozzles made by the Physics Workshop. Nozzle 1 shown in (a) and (c) has a 4 mm diameter hole in the middle and the two M3 threaded tap on the top are for pulling the nozzle from the oven. Nozzle 2 shown is (b) and (d) has a 1 mm diameter hole instead. The nozzles are secured using an M3 grub screw on the side of the oven.

$$v_{rms} = \sqrt{\langle v^2 \rangle} = \sqrt{3k_B T/m}. \tag{2.2}$$

With an opening in the container, atoms effuse out to give an atomic beam having a velocity distribution in this form [48]

$$[f(v)]_{\text{beam}} = \frac{2v^3}{v_p^4} \exp\left(-\frac{v^2}{v_p^2}\right), \tag{2.3}$$

where, v_p is the most probable velocity for the enclosed vapour (as defined above). The most probable velocity in an effusive beam is $[v_p]_{\text{beam}} = \sqrt{3k_B T/m}$, which is coincidentally the same as 2.2. The root-mean-squared velocity of atoms in an effusive beam is also higher than that in a gas, $[v_{rms}]_{\text{beam}} = \sqrt{2}v_p = 2\sqrt{k_B T/m}$.

The velocity distribution of the atom flux is shown in figure 2.9 for oven temperatures in the range from 450 °C to 650 °C, and corresponding root-mean-square velocities are listed in Table 2.1.

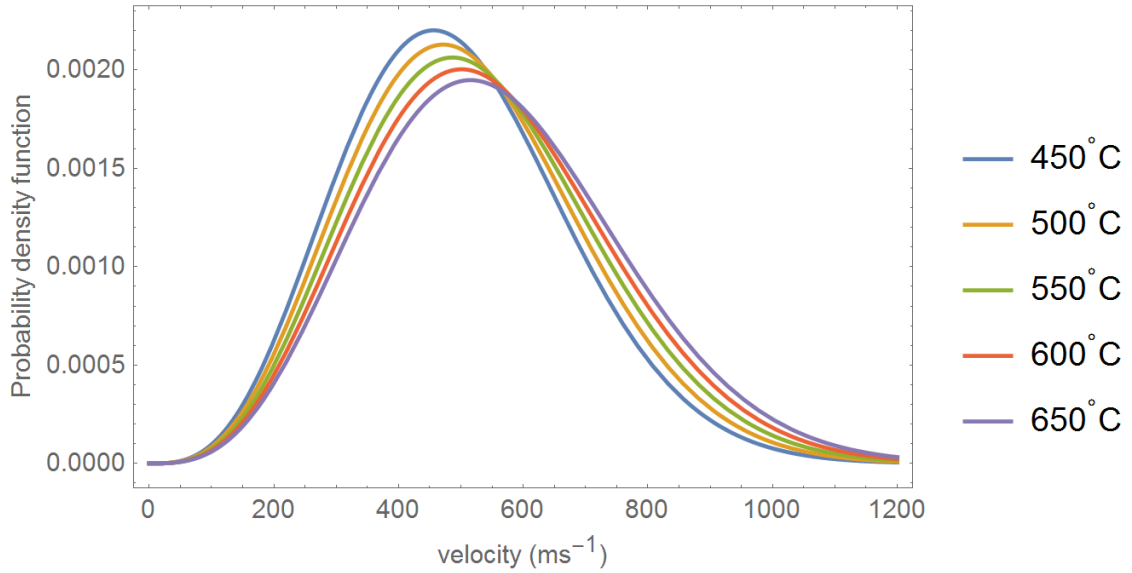


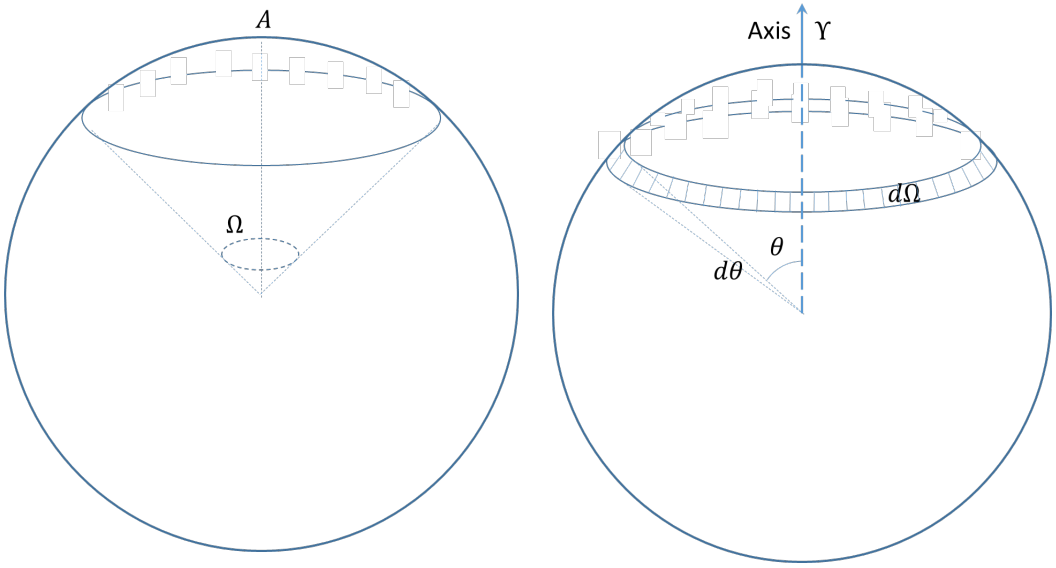
Figure 2.9: The velocity distributions of strontium-87 atoms in an effusive beam at different temperatures, as given by eqn 2.3 (normalised).

2.3.2 Flux out of an aperture

The pressure exerted by a vapour inside an enclosed chamber is caused by collisions of the atoms with the walls. This can be calculated from kinetic theory as follows.

Oven temperature T(°C)	450	500	550	600	650
Referenced work at this T	[64]	[53]	[80]	[31]	[3]
$v_{rms}(\mathrm{ms}^{-1})$	526.6	544.5	561.9	578.8	595.0

Table 2.1: The root mean squared velocity of atoms in an effusive beam $[v_{rms}]_{\mathrm{beam}}$ at different temperatures that are typically used.



(a) Solid angle Ω

(b) Element of the solid angle $d\Omega$

Figure 2.10: (a) A solid angle Ω in a sphere (radius r) is defined as the ratio of surface area and radius squared $\Omega = A/r^2$ in units steradians (sr). (b) The shaded area on a unit sphere represents the element of solid angle $d\Omega$, for cylindrical symmetry (no ϕ dependence) which can be expressed as $2\pi \sin\theta \, d\theta$.

The number of atoms with velocity between v and $v + dv$ and direction between θ and $\theta + d\theta$ (with element solid angle $d\Omega$, as illustrated in Fig 2.10a.) is equal to

$$n\frac{d\Omega}{4\pi}f(v)dv, \tag{2.4}$$

where $d\Omega = 2\pi \sin\theta d\theta$ (Fig 2.10b).

As shown in Fig 2.11, atoms travelling at angle θ to the normal and incident of an area A of the wall sweep out a volume of

$$A\cos\theta \, v \, dt. \tag{2.5}$$

So the number of atoms hitting the area A per unit time with velocity between v and $v + dv$ and angle between θ and $\theta + d\theta$ is

$$\frac{1}{2}nAvf(v)dv \cdot \cos\theta \sin\theta d\theta. \tag{2.6}$$

If an aperture with area A is opened on the chamber's wall, the total atomic flux Φ_{total} through this aperture (number of atoms going per unit time), can be evaluated as

$$\begin{aligned}\Phi_{total} &= \frac{1}{2}nA\int_0^\infty vf(v)dv \cdot \int_0^{\pi/2}\cos\theta\sin\theta d\theta, \\ &= \frac{1}{4}nA\langle v\rangle, \end{aligned} \tag{2.7}$$

where the mean velocity $\langle v\rangle$ is defined as

$$\langle v\rangle = \int_0^\infty vf(v)dv = \sqrt{\frac{8k_BT}{\pi m}}. \tag{2.8}$$

The angular intensity $I(\theta)$ is defined as the number of atoms effusing out from the source with direction angle θ (to centre line axis Υ) per solid angle per unit time, which for an infinitely thin aperture, is

$$\begin{aligned} I(\theta) &= \frac{n}{2}\int_0^\infty vf(v)dv \cdot \frac{\cos\theta\sin\theta d\theta}{d\Omega}, \\ &= \frac{1}{4\pi}n\langle v\rangle\cos\theta, \\ &= I_0\cos\theta, \end{aligned} \tag{2.9}$$

where, the peak (angular) intensity is

$$I_0 = I(0) = \frac{\Phi_{total}}{\pi}. \tag{2.10}$$

It is useful to express the angular dependence as the function $j(\theta)$

$$j(\theta) = \frac{I(\theta)}{I_0}. \tag{2.11}$$

For an infinitely thin-wall aperture, this is $j(\theta) = \cos\theta$. Each atom hits the wall carrying a momentum of $2mv\cos\theta$, so the total momentum transferred to the wall per unit time divided by area A, gives the pressure as

$$\begin{aligned} P = \frac{F}{A} &= \int_{v=0}^\infty\int_{\theta=0}^{\pi/2} 2mv\cos\theta(\frac{1}{2}nvdt\cos\theta f(v)dv\sin\theta d\theta), \\ &= mnA\int_0^\infty v^2f(v)dv\int_0^{\pi/2}\cos^2\theta\sin\theta d\theta = \frac{1}{3}mn\langle v^2\rangle. \end{aligned}$$

Using the expression for $\langle v^2\rangle$ from above and the standard result $P = nk_BT$ gives the total flux and peak intensity for a thin-wall aperture as

$$\Phi_{total} = \frac{PA}{\sqrt{2\pi mk_BT}}, \tag{2.12}$$

$$I_0 = \frac{PA}{\pi^{3/2}\sqrt{2mk_BT}}. \tag{2.13}$$

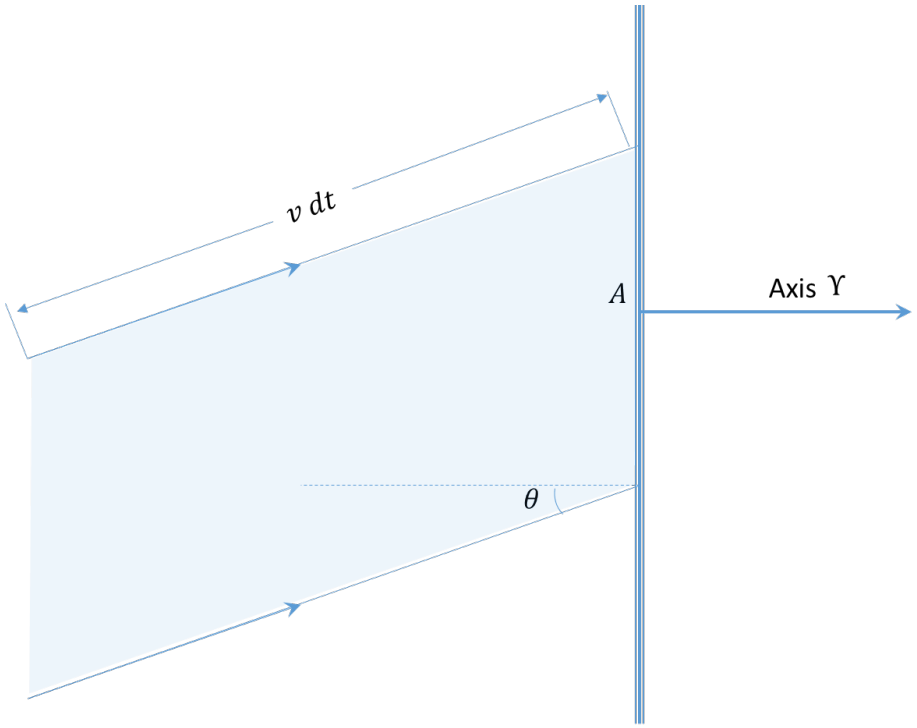


Figure 2.11: The shadowed area represents the volume that atoms at velocity v sweep off. The volume is the product of base area A and the height $vdt\cos\theta$.

There are various models for atomic vapour pressure over temperature and each works over a certain temperature range. We are aiming for oven temperatures over450 °C (723 K) and have experimentally reached 642 °C (925 K). The Boerboom model[13] for strontium vapor pressure covers the temperature range from $T = 775$ K to 925 K, is the best for our experiment. The pressure-temperature formula is given by

$$\log_{10} P = 9.753 - \frac{7628}{T}, \tag{2.14}$$

where P is in units of Pa and T in units of K. We draw the predictions of the three different models in Fig 2.12: Asano model[4] intended for 494-660 K, Prislkov model[4] intended for 673-873 K and Boerboom model intended for 775-925 K[13]. Although Boerboom model was not intended for describing pressure when temperature is under 775 K, it still agrees well with the Prislkov model, which is specified to range 673-873 K. This vapour pressure formula will be used to calculate the total flux and peak intensity.

Our design of nozzle has a 4 mm diameter corresponding to an area of $A = 1.26 \times 10^{-5}$ m^2. The flux increases exponentially with temperature, e.g. from around $\Phi_{total} \simeq 1 \times 10^{17}$ atoms/s at $T = 773$ K (500 °C) as in Table 2.2 to 2×10^{18} s^{-1} at 900 K, as

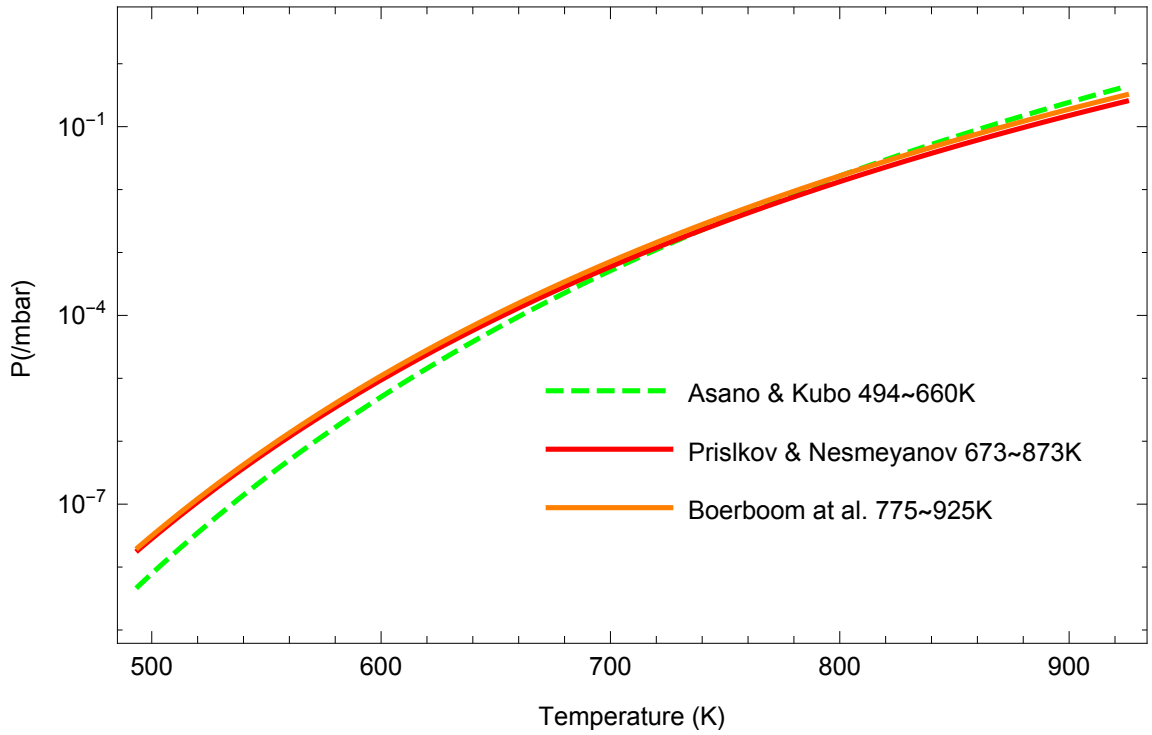
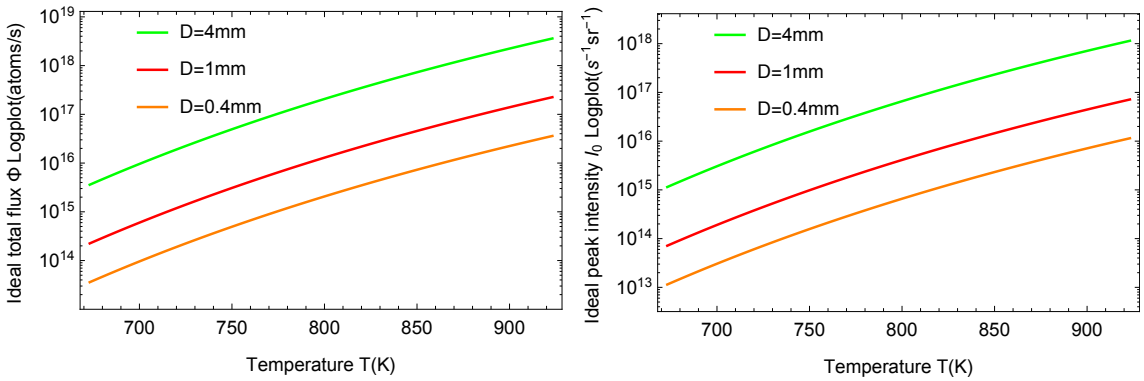


Figure 2.12: This curve is a log-linear plot for Pressure (mbar) against Temperature (K). The pressure of strontium vapour for a range of temperatures has been measured and analytically described in several references. These different analytical models are optimal for in specific ranges of temperatures. We are interested in the behavior from 400 °C to 750 °C, The models of Prislkov et al.[60] and Boerboom et al.[13] agree closely over the range 500-950 K. We use the Boerboom model for all calculations to avoid switching models for only a marginal improvement in accuracy.

Diameter of the aperture D	4 mm	1 mm	0.4 mm
Flux, Φ_{total} [atoms/s]	9.8×10^{16}	6.1×10^{15}	9.8×10^{14}
Peak angular intensity I_0 [$s^{-1}\,sr^{-1}$]	3.1×10^{16}	2×10^{15}	3.1×10^{14}

Table 2.2: Total flux and peak intensity at 500 °C for ideal apertures (infinitely thin wall) of different diameters.



(a) Ideal flux Φ_{total}-T (b) Peak intensity I_0-T

Figure 2.13: (a) The total flux out of an aperture and (b) the peak intensity over an range of temperatures at different aperture diameters (log-linear plots).

shown in Fig 2.13a. However, we do not have a hole in a thin-wall.

2.3.3 Effusion of atoms through a tube

While an aperture in an infinitely thin wall is meaningful for theoretical calculations, a more realistic case for determining the flux from an atomic oven in practice is effusion along a tube of finite length, L, as illustrated in Fig 2.14 (tube of diameter D). For the aspect ratio of $D/L \sim 0.1$ used in this work, a very small fraction of atoms go straight through without hitting the wall (proportional to D^2/L^2). The majority of atoms strike the wall are assumed to be re-emitted according to a cosine distribution [21], as in eqn 2.10. Atoms striking the wall before the halfway point have a large chance to be reflected back into the chamber; this reduces the flux out of the tube and explains why a thin tube collimates the atomic beam. A numerical simulation for effusing atoms' effusing out from a lithium oven is given in Ref [66].

2.3.3.1 Collision-less vs. continuum flow ('opaque' mode)

There are two regimes for atomic flux flowing out of a tube: the collision-less regime (molecular) and the opaque mode[65]. Two important factors in the calculations are

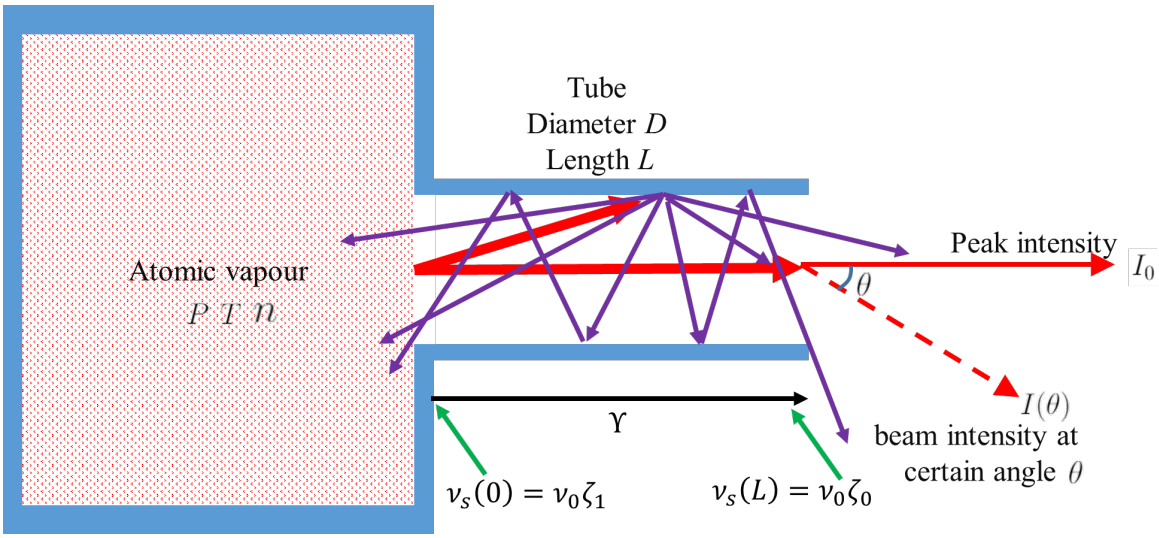


Figure 2.14: An illustration of the collimation of an atomic beam by a tube. Atoms striking the wall have a chance to go back to the oven body, while atoms going straight through do not. This gives an intuitive explanation that can be made quantitative[66]. Many atoms that strike the wall before the halfway point in the tube are reflected back to the left side.

the geometry factor β and Knudsen number K_{nL} [37] which are defined as:

$$\beta = \frac{D}{L} = \frac{2r}{L} \tag{2.15}$$

$$K_{nL} = \frac{\Lambda}{L} \tag{2.16}$$

where Λ is the mean free path (defined below). Free-molecular flow occurs when the mean free path is large compared with the length L, which corresponds to $K_{nL} \gg 1$ (or $K_{nL} \gg \beta$ if $\beta > 1$).

The angular distribution and centerline intensity start to deviate from the values calculated from collision-free scheme at $K_{nL} \leq 10$, at which point intermolecular collisions cause the angular distribution to widen and the collimation becomes worse. However, Clausing[21] reported that intermolecular collisions do not change the total flux significantly over range of $\beta \leq K_{nL} \leq 10$, or $D \leq \Lambda \leq 10L$. This corresponds to $\Lambda = D = 0.4$ at 940 K for the Prototech oven and $\Lambda = D = 4$ mm at 832 K, for the other oven (so that K_{nL} stays above β). Thus we can get accurate results using the collision-free scheme for flux calculations in Sec 2.3.3.3 rather than the more complicated formulae for the opaque mode[65].

2.3.3.2 Mean free path and flow regimes

The mean free path of atoms is given by[12]

$$\Lambda = \frac{1}{\sqrt{2}n\pi d^2} = \frac{k_B T}{\sqrt{2}\pi d^2 P} \tag{2.17}$$

where d is the diameter of the atom or molecule. Strontium atoms have a diameter of $d = 4.09 \times 10^{-10}$ m[45]. A plot of the mean free path as a function of temperature is shown in Fig 2.15.

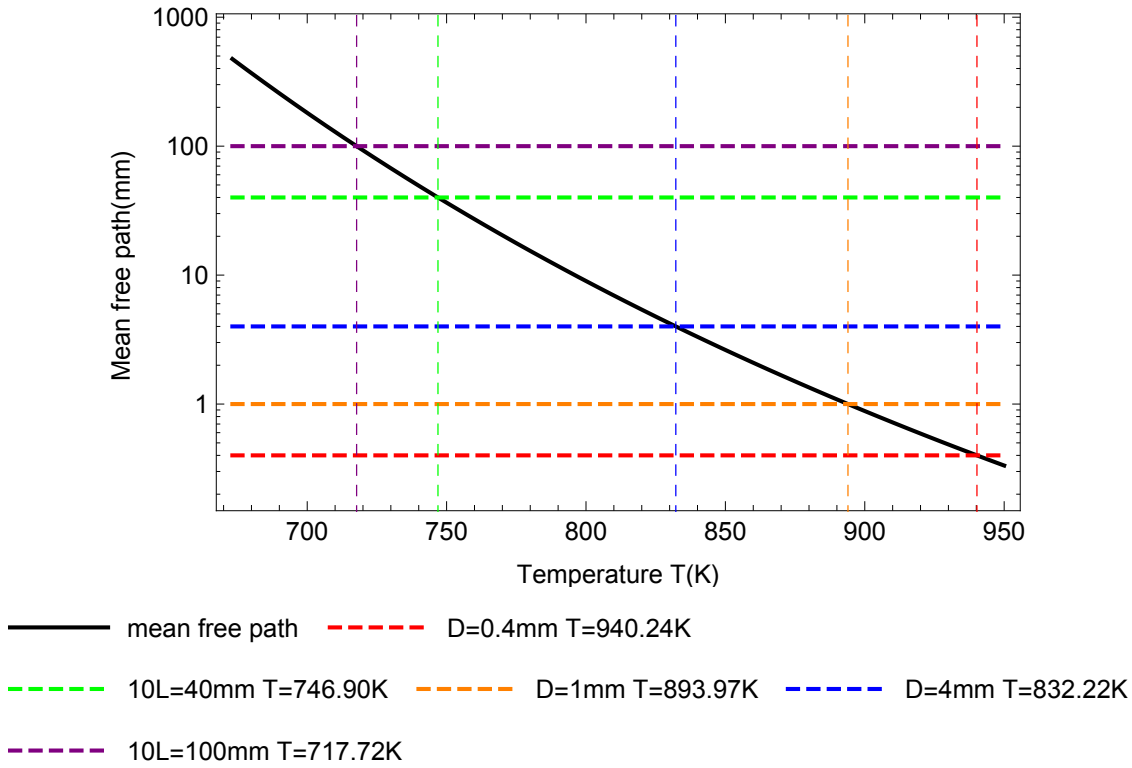


Figure 2.15: Mean free path of strontium vapour as a function of temperature is shown here. The grid of dashed lines refers to boundaries (D and $10L$) where the flow mode will switch, for different tubes (with different D and $10L$). For the Prototech nozzle, with $D = 0.4\,\text{mm}$ and $10L = 40\,\text{mm}$, the best temperature range is $T \leq 747\,\text{K}$, but $747\,\text{K} \leq T \leq 940\,\text{K}$ is acceptable but collimation would be compromised.

2.3.3.3 Collision-less flow (Free molecular flow)

One of the important assumption for treatment of the collision-free flow is that the rate of molecules striking at a unit area of wall, $\nu_s(\upsilon)$, follows a linear function

$$\nu_s(\upsilon) = \nu_0[\zeta_1 - (\zeta_1 - \zeta_0)(\frac{\Upsilon}{L})], \tag{2.18}$$

where v is the distance from entrance of the tube, as shown in Fig 2.14. The other important assumption is that the direction or re-emission of atoms after striking the tube's wall follows a cosine distribution[12]. As described previously, we use $I(\theta) = I_0 j(\theta)$ (where $j(\theta) = \cos\theta$ for the ideal hole). In order to describe the angular dependence $0 \leq j(\theta) \leq 1$ for a tube, we first define the following parameters[25],

$$\begin{aligned} q(\theta) &= \frac{L}{2r}\tan\theta, \\ R(q) &= \cos^{-1}(q) - q\sqrt{1-q^2}, \\ \alpha &= \frac{1}{2} - \frac{1}{3\beta^2}\Big(\frac{1-2\beta^3+(2\beta^2-1)\sqrt{1+\beta^2}}{\sqrt{1+\beta^2}-\beta^2\sinh^{-1}(1/\beta)}\Big), \end{aligned} \tag{2.19}$$

where L is the length of the cylindrical aperture and r is the radius. When $q \leq 1$ (where the angles are low enough for some atoms to pass through without hitting the wall)

$$j(\theta) = \alpha\cos\theta + \frac{2}{\pi}\cos(\theta)[(1-\alpha)R(q) + \frac{2}{3q}(1-2\alpha)(1-(1-q^2)^{3/2})], \tag{2.20}$$

and when $q \geq 1$ (large angles)

$$j(\theta) = \alpha\cos\theta + \frac{4}{3\pi q}(1-2\alpha)\cos(\theta). \tag{2.21}$$

The difference between these two formulae is the flux of atoms that do not collide with the walls. By integrating over the angle θ[65], we obtain the total flux out of the tube as

$$\Phi_{tube} = W\Phi_{total}, \tag{2.22}$$

where W is the transmission probability given by

$$W = 1 + \frac{2}{3}(1-2\alpha)(\beta - \sqrt{1+\beta^2}) + \frac{2}{3\beta^2}(1+\alpha)(1-\sqrt{1+\beta^2}). \tag{2.23}$$

The transmission probability W and angular dependence $j(\theta)$ are both only dependent on the geometry factor $\beta = D/L$ defined by aspect ratio of the tube, and independent of mean free path, temperature, pressure, categories of atoms. This independence is lost when the temperature rises up to reach the opaque mode. The transverse and longitudinal velocity can be determined from the angular dependence $j(\theta)$ and the beam velocity $f_b(v)$, but cannot be expressed as an explicit function.

With these formula, we can work out the angular dependence $j(\theta)$ (Fig 2.16), W (Fig 2.17), the total flux (Fig 2.18) and peak intensity $I(0) = I_0 j(0)$ (Fig.2.19) for different nozzles (different β) as a function of temperature. Important results for the comparison between the performance of nozzles at 500 °C are summarised in Table 2.3, and these results show why a multi-channel nozzle is a good choice.

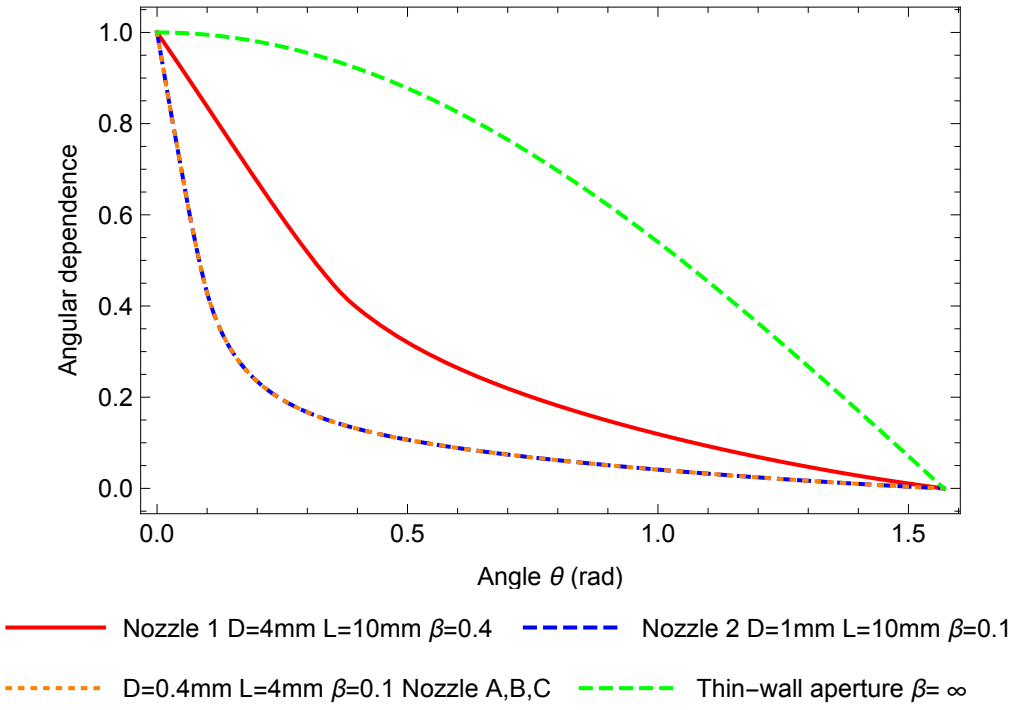


Figure 2.16: Angular dependence $j(\theta)$ over as a function of angle (Eqns 2.20 and 2.21). We can see that smaller β gives a more collimated atomic beam (smaller divergence).

D /mm	4	1	0.4	D=0.4
L /mm	10	10	4	4
No. of channels	1	1	1	76
β	0.4	0.1	0.1	0.1
W	0.31	0.11	0.11	0.11
K_{nL}	1.9	1.9	4.7	4.7
Total flux Φ_{total} (atoms/s)	3.0×10^{16}	6.7×10^{14}	1.1×10^{14}	8.1×10^{15}
Peak intensity I_θ ($s^{-1}sr^{-1}$)	3.1×10^{16}	2.0×10^{15}	3.1×10^{14}	2.4×10^{16}

Table 2.3: Comparison between different nozzles at 500 °C. Multi-channel nozzle has comparable flux as the nozzle with large-size hole, but much better collimation(peak intensity over total flux). The 1mm-single-drilled-hole nozzle has similar performance for collimation, but has much less flux compared with a multi-channel nozzle.

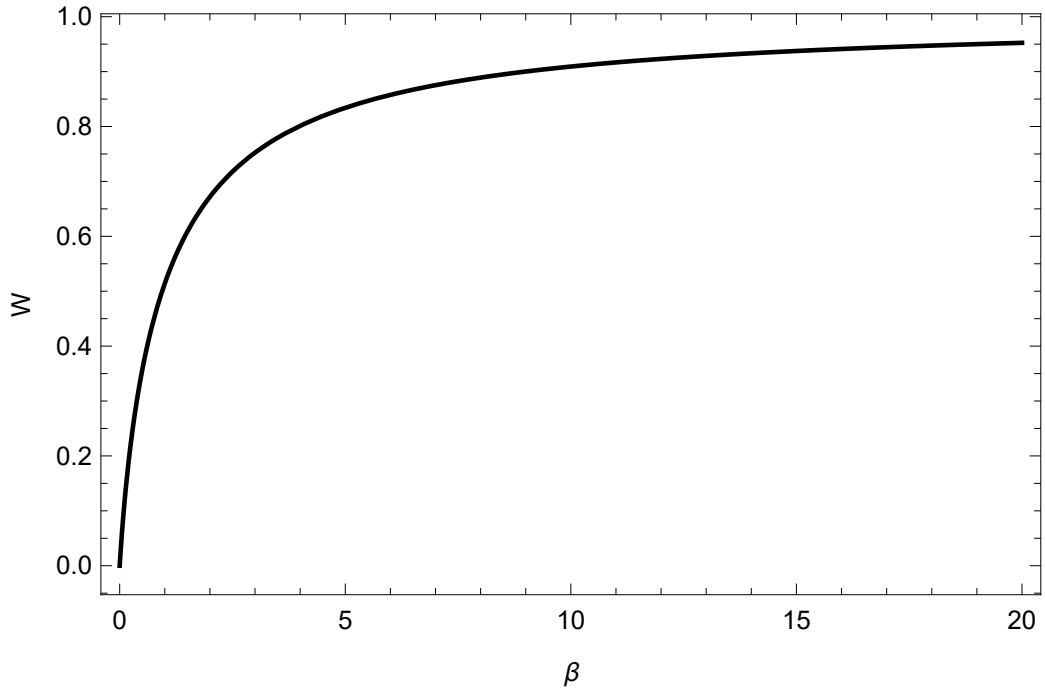


Figure 2.17: The transmission probability W depends and only depends on the geometry factor β ($W - \beta$ curve). As expected $W \to 1$ as $\beta \to \infty$.

2.3.4 Hydrodynamic flow (opaque mode)

As the mean free path decreases with increasing temperature (Sec 2.3.3.2), a hydrodynamic mode treatment is studied in Chapter 3 for cases where the Knudsen number is less than 10, but still greater than 1. For cases where the Knudsen number is less than 1, there is no analytical expression to describe the problem and numerical simulation is the only solution to study the total flux and angular dependence. In most atomic source applications, for collimation of atomic beams, the oven is working in a collision-free scheme. We explored opaque mode treatment and noticed some error in a few traditional references, which are reported in Chapter 3.

2.4 Heaters and the temperature control system

We obtained customized heaters directly from a Chinese supplier (Laiyuan) and a picture of a set of six heaters is shown in Fig 2.20b. Each heater is 4 mm in diameter and 78.5 mm in length (Fig 2.20a). The maximum temperature rating of the heater tube is 800 °C. The heating occurs in the top 16 mm (this tip is referred to as 'hot end'). The 5-inch-long leads are protected with fiberglass, which is rated up to 450 °C, which is used to connect to the cold ends. Each heater can produce 20 W of heat

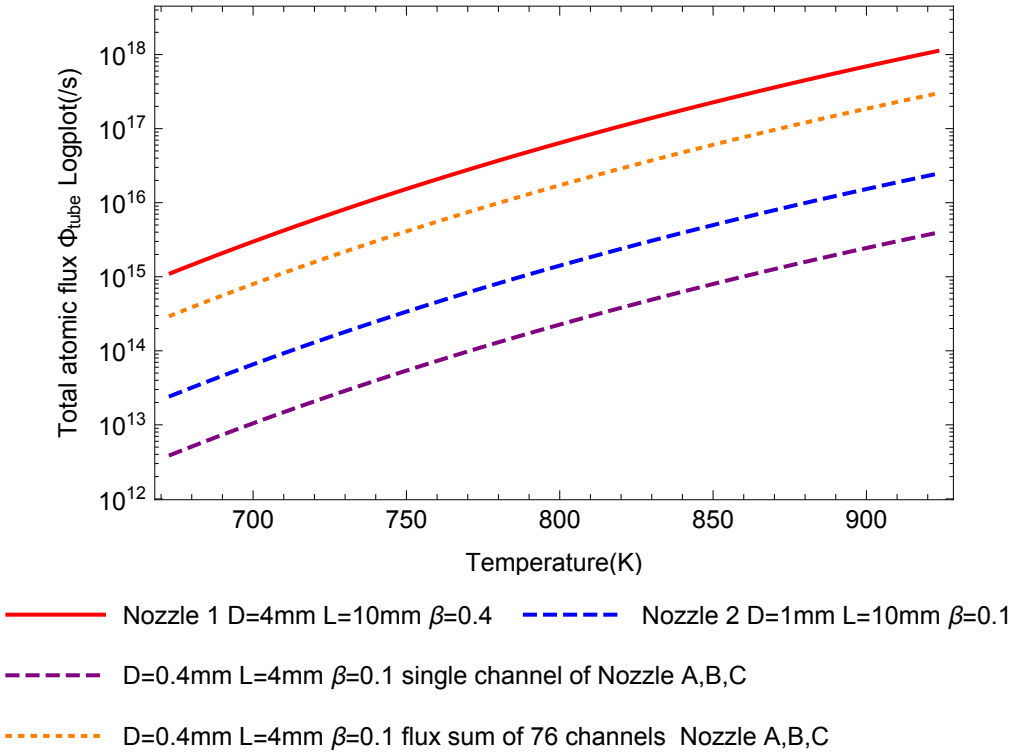


Figure 2.18: Total flux Φ_{total} over a range of temperature from 673.15 K to 923.15 K. The multi-channel nozzle (orange dotted line) has comparable flux with nozzle 1 (4mm diameter hole) and much more flux than nozzle 2 (1mm diameter hole). Considering the multi-channel nozzle's collimation, it is the best choice.

with a 24 V DC power supply. The total 120 W, from all six heaters together is more than sufficient for this project. The thermocouples we used were 3 mm in diameter, 150 mm in length and rated up to 1100 °C (RS Pro K-type Thermocouple, 397-1264).

We stabilize the temperature using an on-off PID temperature controller unit (Red lion T1621110). This unit takes an input from a K-type thermocouple and drives a solid-state relay that controls the current to the heaters. This relay is rated to 2 kW (RS 200-2058, 100 VDC, 20A) which far exceeds the maximum power for the six heaters (120 W).

To remotely monitor the temperature of the oven, a data logging system was set up (based on software from Elliot Bentine[8]). The low voltage from the thermocouple was amplified by a small break-out PCB board (AD8495 Breakout board from Adafruit) connected to an Arduino board. The Arduino board is programmed to send the data via a serial connection through a USB cable to a the data-logging program on a PC, which in turn sends the data to a time series database (InfluxDB). This enables access to the data from anywhere on the network in the department, and

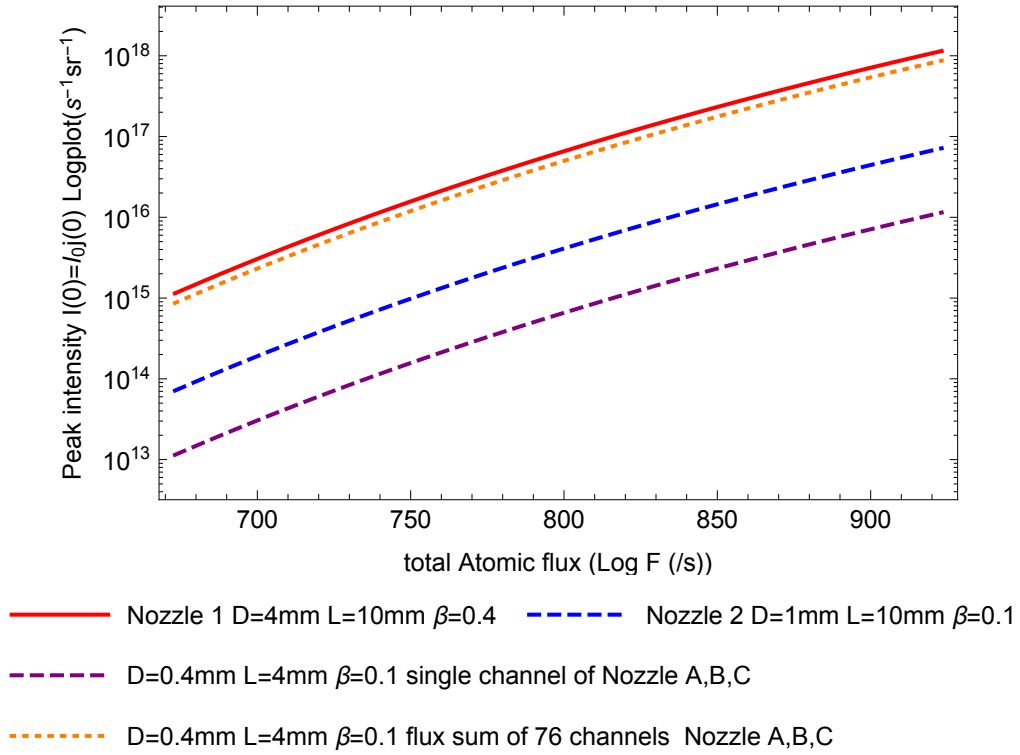


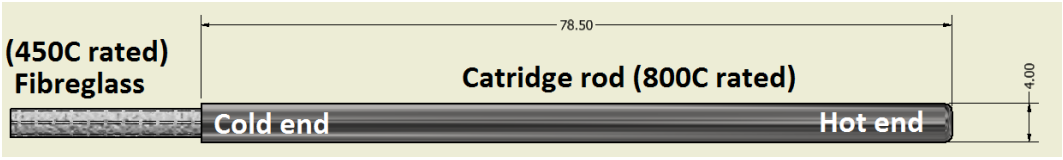
Figure 2.19: The peak intensity $I(0) = I_0 j(0)$ over a range of temperature from 673.15 K to 923.15 K. With smaller hole size, the peak intensity drops. In our Prototech nozzles, one single channel have a very limited peak intensity, but the total flux adds up to give a similar peak intensity to a large-size hole, but with better collimation, provided by a multi-channel arrangement. This supported the usage of the multi-channel nozzle.

beyond. We typically plot the acquired data using the Grafana web application.

The electronics for the cold-atom source has been boxed-up into a unit. The diagram of the control loop is shown in Figs. 2.21a. The unit contains the T1621110 temperature control unit, six thermocouple inputs with each channel having a signal conditioning amplifier, and a 16-channel Arduino board with a USB connection port to the computer. In addition to temperature readings, the system records the vacuum pressure using the monitoring signal from the ion pump controller and vacuum gauge, and data logger send alerts when set limits are exceeded. At least four thermocouples are attached to various positions on the chamber and coils to ensure fail-safe operation.

2.5 The vacuum system

Both ovens (from Prototech and the Workshop) were tested before the laser system was set up by loading strontium in, heating them and observing by eye that the

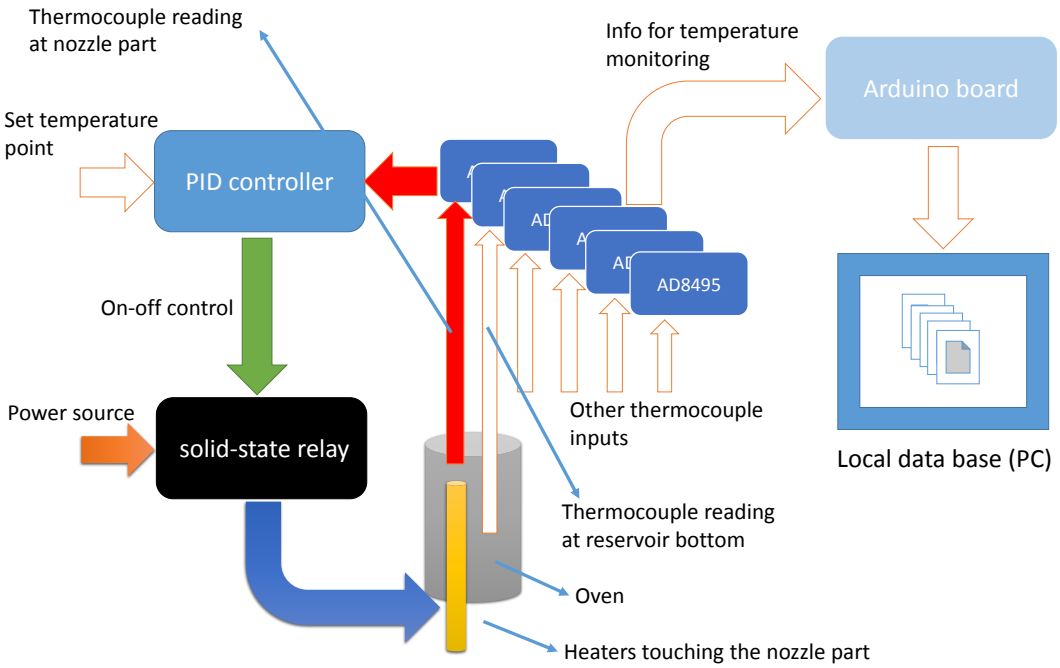


(a) The heater structure.

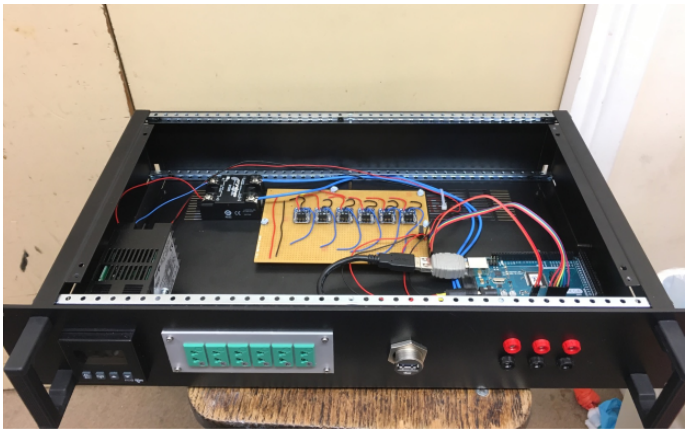


(b) Image of the a set of six heaters.

Figure 2.20: (a) The dimensions and structure of the heater. The rod is made of stainless steel and the heater body is rated to 800 °C. Resistive wires are at the hot end and there is no heating at the cold end apart from heat conduction from hot end. The temperature at the cold end can remain moderate as the length of the rod is designed to be long enough; (b) The set of heaters can provide up to 120 W of power for the oven.



(a) Diagram of the control electronics.

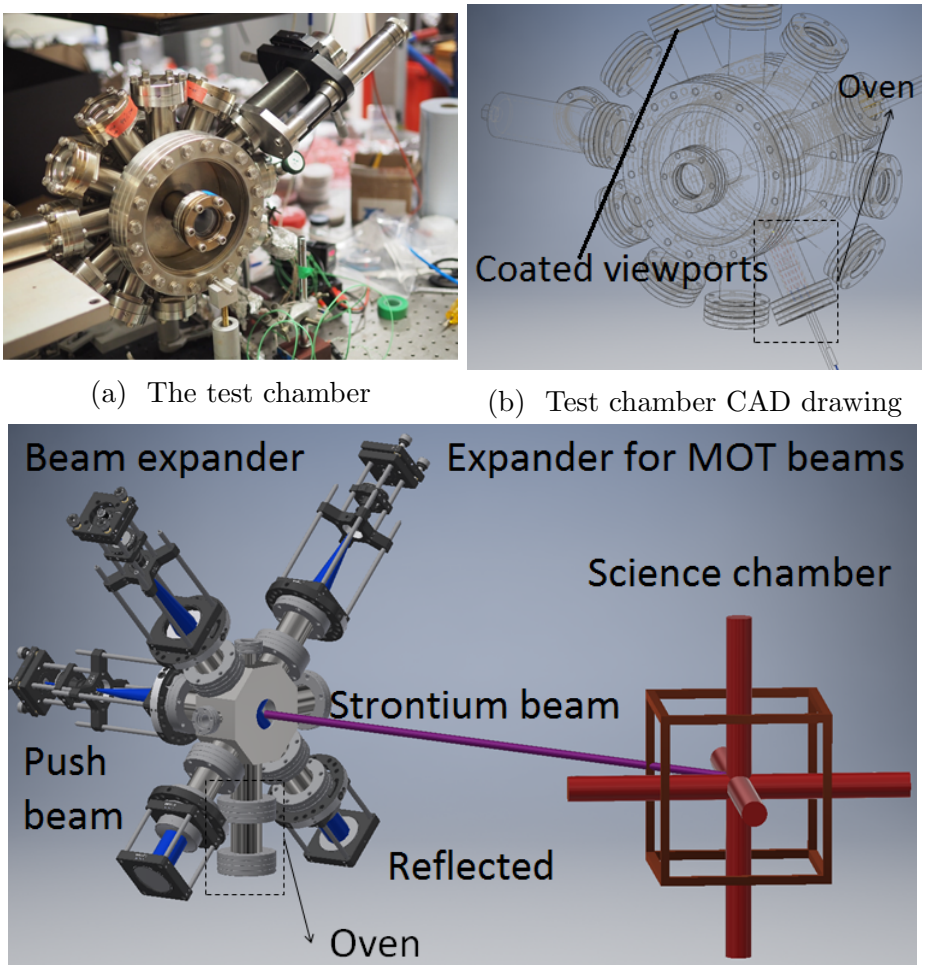


(b) The home-made electronics box.

Figure 2.21: (a) shows the diagram for control loop. The control logic is based on the PID controller. Temperatures signals taken by thermocouples are amplified and read in by the Arduino board, which then are transferred into a local data base. (b) shows the top view of the electronics box. All inputs and outputs are integrated on the front panel of the rack unit box so that electronics inside can stay covered and sealed, which provides a robust control system.

viewports of a test chamber (Fig 2.22a and 2.22b) became coated with strontium - even a thin layer of deposited metal (of a few times the skin depth at optical frequencies) forms a mirror. Thus we verified the basic operation of each oven before installing them in their intended vacuum systems.

A schematic for our strontium cold-atom source is shown in Fig 2.22c . The oven produces a thermal atomic beam that is directed upwards towards the 2D+ MOT, which cools atoms and pushes them out (as purple line) for further experiment.



(a) The test chamber

(b) Test chamber CAD drawing

(c) The proposed $2D^+$ MOT scheme

Figure 2.22: (a) and (b) show the 12-port test chamber. The first observation of a thin layer of deposited strontium on viewports showed both ovens are working properly. (c) a schematic of the design of our strontium cold-atom source (with blue laser light). The atomic beam coming out of the oven moves upwards, is cooled by the 2D+ MOT, then a push beam pushes the cooled atoms out of the trap toward the second chamber, which is represented by a red cube in (c).

2.5.1 MOT chamber

2.5.1.1 Main chamber

The chamber (Fig.2.23) is manufactured by VG Scienta using 316LN non-magnetic steel. Its dimensions have been optimised to be compact while still allowing for CF40 viewports[77], and optical access via tubes with an inner diameter of 34 mm. The final set-up is shown in Fig 2.24a

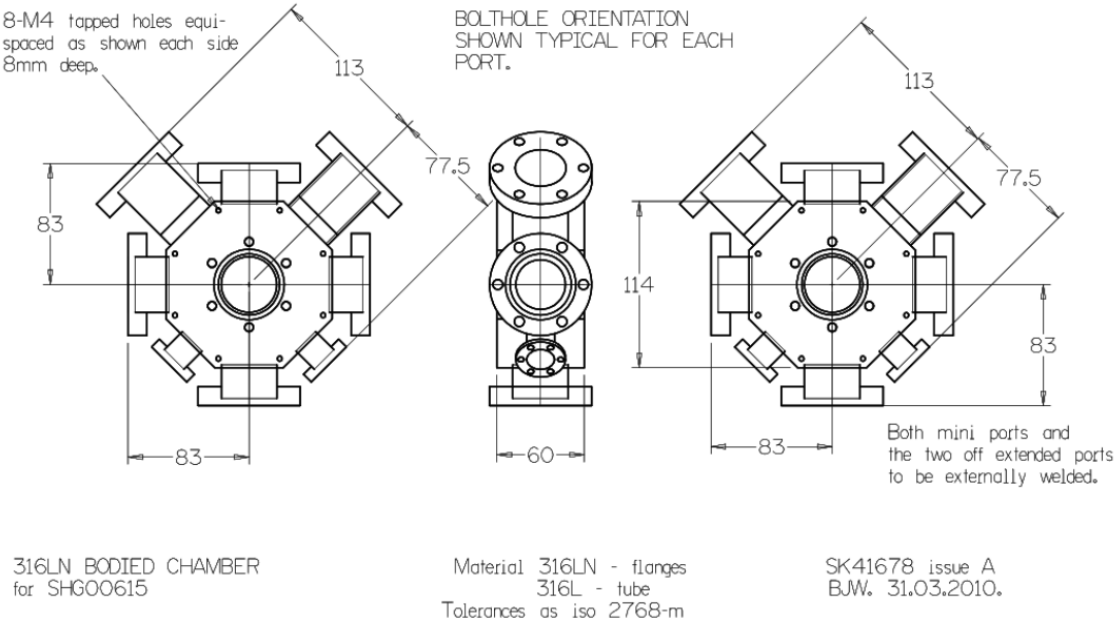
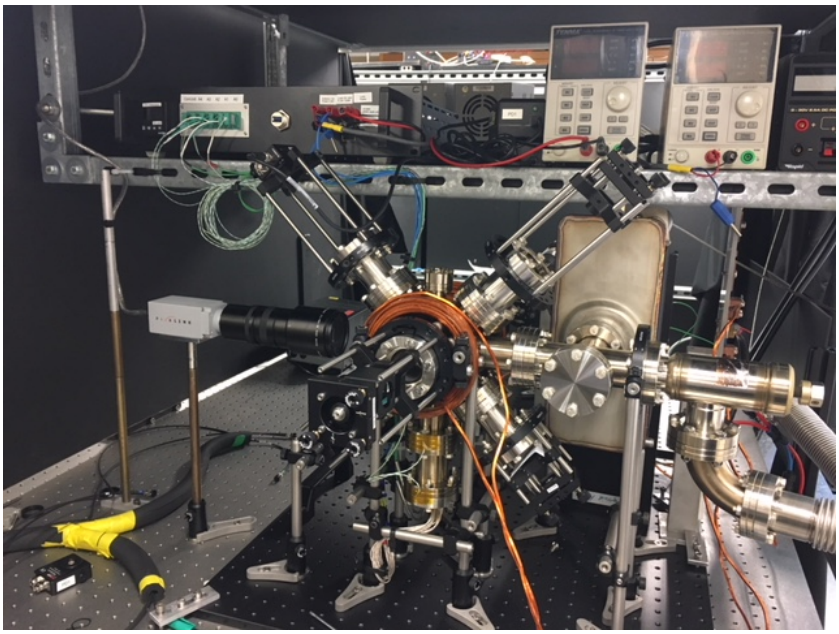


Figure 2.23: The MOT chamber was designed originally by Dimitrios Trypogeorgos for use as a 3D MOT with a minimised size, but it can still have CF40 ports (picture from Ref [78].

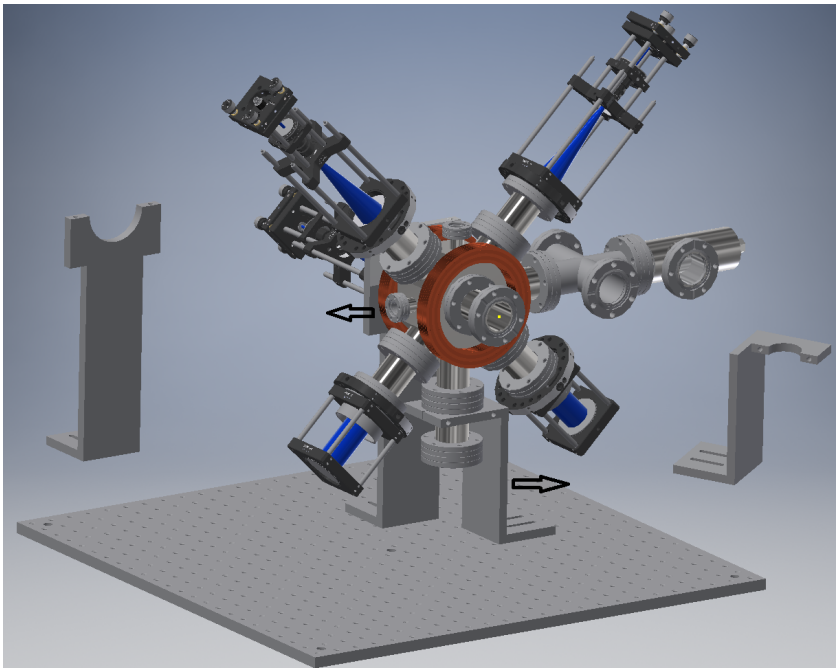
The small chamber makes it hard to avoid strontium coating on viewports that are on a line of sight to the nozzle. So extensions were added extensions to move the viewports away from the strontium oven; these tubes were 60mm CF40 nipples (FN-C311A-60 fixed and FN-C313A-60 rotatable, Kurt J. Lesker). A standard CF40 four-way cross (C-0275, Kurt J. Lesker) provided ports for connecting to an ion pump and an all-metal angle valve, where a turbo pump was connected to pump down the system.

2.5.1.2 Coils for the MOT chamber

A MOT for strontium operating on the blue transition requires a high field gradient of up to 75 G/cm[53]. This gradient is commonly generated by a pair coaxial coils



(a) The integrated apparatus.



(b) Original idea for supporting the chamber.

Figure 2.24: (a) shows the full apparatus with cage-mounted optics, vacuum components, viewports, control box and various thermocouples are attached to the chamber to monitor the temperature change. (b) shows the intended supporting design. But we then moved to standard Thorlabs posts and cage systems, which is shown in (a), to save time and cost.

with currents running through them in opposite directions so that the magnetic field is zero at the centre, producing a quadrupole field. Each coil has 25 turns wrapped from a 3.7 mm square hollow tubing with cooling water running through and overall dimensions: ID=102.5 mm, OD=139.5 mm, thickness 18.5 mm. The coils are mounted as shown in Fig 2.24a. The maximum current in the quadrupole coils is 200 A, which is limited by power dissipation in the coils. The magnetic field generated by a coil is

$$B = \frac{n\mu_0 R^2 I}{4\pi} \frac{1}{(z^2 + R^2)^{3/2}}, \tag{2.24}$$

where z is the the distance from the coil centre along the axis of symmetry, n is the number of turns. With 100 A of current applied, the magnetic field and its gradient are shown generated by the pair coils are shown in Fig 2.25. The gradient is nearly constant through the centre.

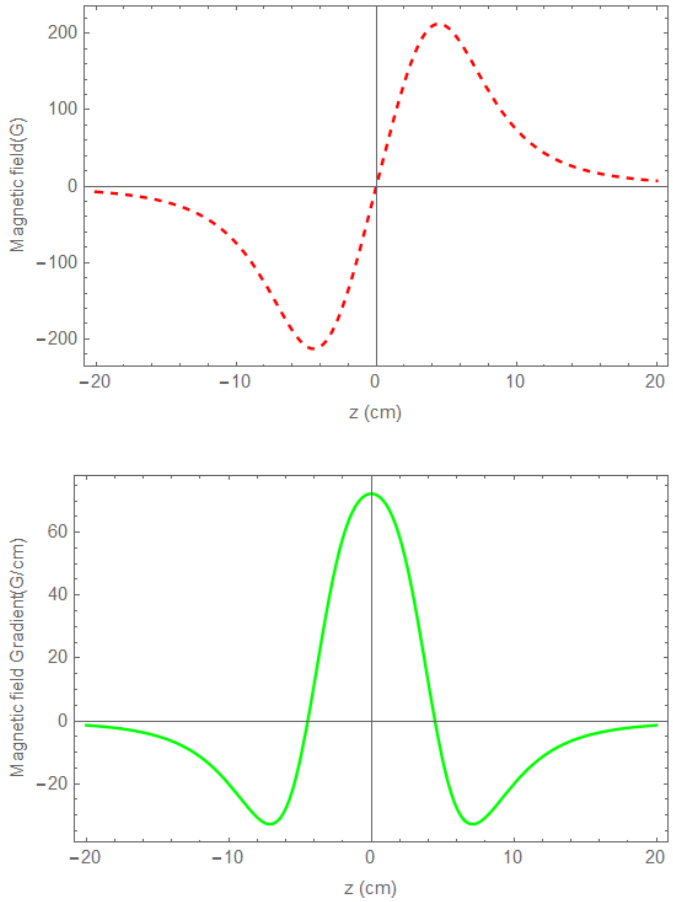


Figure 2.25: The magnetic field and the gradient generated by the quadrupole coils ($I = 100$ A). The gradient is 72.3 G/cm at $z = 0$ with the current $I = 100$ A.

2.5.2 Supporting and viewports

A set of supporting frames have been built to fit the compact source and to ensure open access to all viewports and flanges. One stand is for clamping down the standard CF40 flange at the back and the other stand is for holding the bottom flange while clamping the tube at the same time (Fig 2.24b). The two stands fix the chamber in three dimensions, while giving enough access for doing up the vacuum flanges, or setting up optics. However, in later work we moved over to mounts made from commercial components (from Thorlabs): posts, post holders, post construction accessories which are compatible with the (Thorlabs) cage system and flange-cage adapters for optics, as shown in Fig 2.24a. The use of catalogue items eliminated the need for machining.

Uncoated viewports were measured to have 94% ttransmission, but an AR coating is required because laser beams are retroflected to form the MOT, so we must minimise losses to keep the optical forces balanced in both directions. Therefore, to use the blue light efficiently we installed anti-reflective (AR) coated viewports. There are two types of AR coating that are commonly provided by suppliers: broadband anti-reflective coatings (BBAR) which have four layers and cover a large range (e.g. 400-700 nm), and simple coatings with just a single layer of quarter-wave optical thickness (QWOT). Since we are working at a single wavelength (461 nm), a QWOT is the best choice. We selected Kodial zero length Viewports (Torr Scientific, VPZ38AR NW35CF, QWOT) mounted in 304L stainless steel, from Torr Scientific Ltd, which can withstand 350 °C. Silver plated bolts are used to assemble the vacuum system since these do not require messy lubrication which can contaminate the inside of the vacuum components if not handled very carefully (bolts used are 35 mm M6 CFBM6-35, 25 mm M6 CFBM6-25 and 20 mm M4 CFBM4-20, from Scanwel).

When the vacuun needs to be opened we fill it with argon gas to prevent oxidization of the strontium. However, strontium is not as reactive as alkalis such as rubidium and a short exposure to air (of the order of a few seconds) does not affect the subsequent performance of the oven, particularly because the oven has a small aperture which limits the permeation of air. (We used a BOC 11-X pureshield argon cylinder, Industrial Grade, 2.36 m^3 with a G-tech single-stage argon regulator.)

2.5.3 Spectroscopy chamber

We used modulation transfer spectroscopy with a tunable magnetic field to generate an error signal for locking the frequency of the strontium cooling beams. This

allows measurements of the loading rate over a range of frequency detunings[2]. The spectroscopy chamber (Fig 2.26) has two CF40 four-way cross (Kurt Lesker C-0275) connected together. A T-piece and an all-metal angle valve are used to connect the turbo-pump. The spectroscopy beam passes close to the aperture of the oven. The spectroscopy beam passes through two opposing viewports (Torr Scientific, VPZ38AR NW35CF, QWOT). An standard 55 mm-long nipple is used to ensure that the probe and pump beam can pass through the atomic flux just next to the nozzle where the density is high.

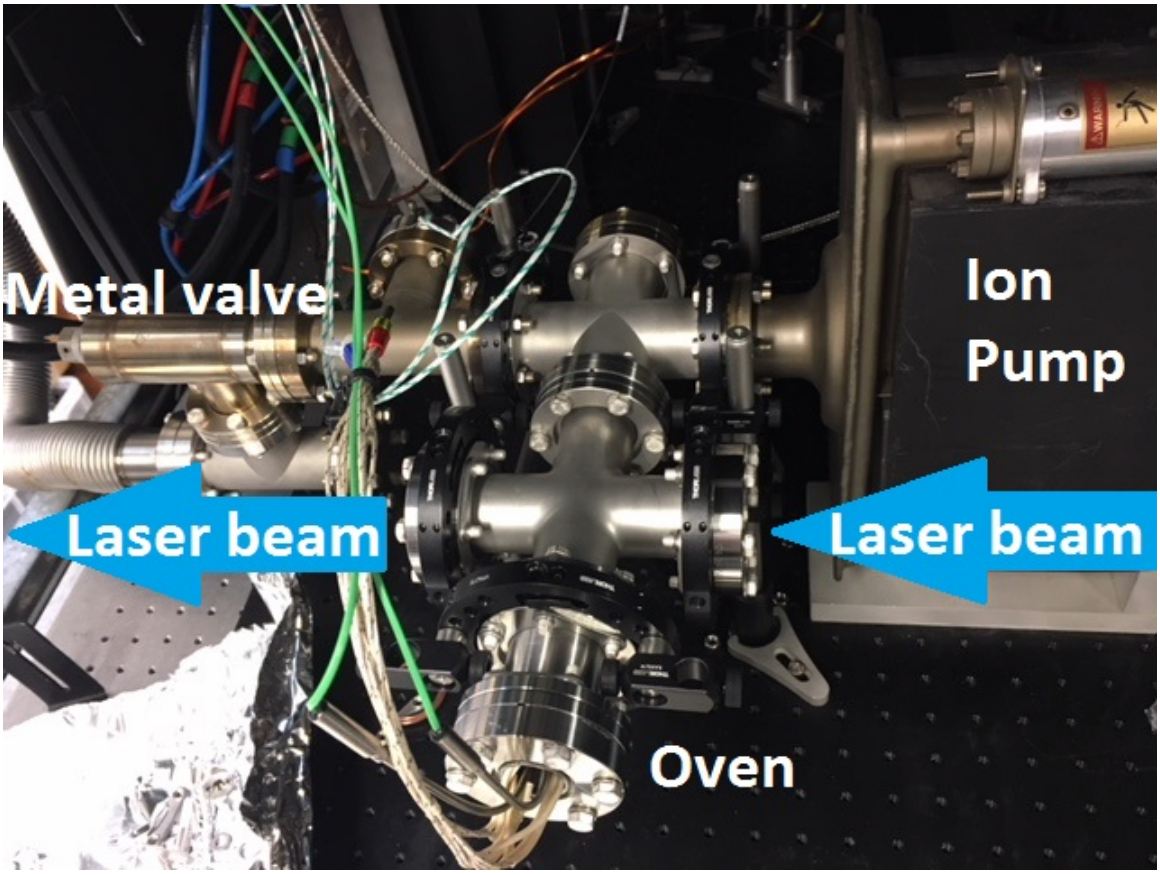


Figure 2.26: Spectroscopy chamber consists of two four-way crosses, a metal valve, an ion pump, an oven and three viewports. Laser beams are sent through the two viewports on the sides.

2.5.3.1 Oven for the spectroscopy chamber

Our initial trial using the Workshop oven in the spectroscopy chamber was not successful because with a 4 mm diameter hole the nozzle created too much vapour in the

[2]Ref.[67] reported a similar scheme for rubidum to our locking technique, while our tunable MTS approach has been proposed and realised by us independently since March, 2019

chamber. Also the strontium flakes came stored in mineral oil, and residue from this oil were vaporised into the chamber giving a high background pressure that scattered atoms from the atomic beam.

We purchased a second oven from Prototech for the spectroscopy chamber (with and a graphite nozzle) and used 99.9%-pure dendritic pieces of strontium (purified by distillation, Sigma-Aldrich 460346-5G), which was delivered in a sealed glass tube filled with a protective argon gas.

The heaters are provided by the Chinese company, Laiyuan, have a maximum working temperature of 800C (tested by the supplier in air) and the maximum voltage applied should not exceed 26.4 V. It is important that the holes drilled in the oven body are well matched to the size of the heaters. The difference between diameter of the heaters and the holes was designed to be 0.15mm. If heaters are not in good contact with the oven body, they can be burned but we also had problems with heaters becoming stuck inside the holes (this made it more cumbersome to reload etc. but was not insuperable).

2.5.3.2 Coils for the spectroscopy chamber

We wound the coils to give the required magnetic field strength over the spectroscopy chamber. The number of turns is 170 and maximum current can be applied is 3 A and the coil can generate 20 G for 1 A current. The heat generated by the coils was sufficiently removed by convection of air on the surfaces of the coils.

2.5.4 Pumping

We used a turbo pump (Pfeiffer hicube eco 80Hi-cube with compact full-range Gauge FPM sealed PKR 251) to pump down both chambers to below 10^{-7} mbar and then switched to an ion pump connected with each chamber (919-0355 VacIon plus 40L/s pump), which are controlled by ion-pump controllers (Minivac 9290291 with a Fisher connection).

2.6 Conclusion

The design and construction of a re-entrant strontium oven is presented in this chapter. The use of graphite nozzles and the absence of vacuum feedthroughs cuts down the cost. A detailed procedure for oven assembly and strontium loading is given in the appendix. Theoretical calculations of the atomic flow show that the multi-channel nozzle gives good collimation of the beam and a high flux. It is important

to note that the collision-free scheme only holds for a certain temperature range, and this has implications for the operating temperature of the oven. Details of the temperature-stabilisation system based on a PID controller are also given, together with the remote data logging that is used for management of experimental data and supervising ovens. This apparatus will be used to load a two-dimensional magneto-optical trap for strontium, and the characterisation of this system will be described in Chapter 3 of this thesis.

Chapter 3

Characterisation of the oven

The re-entrant oven design presented in Chapter 2 has been tested and characterised, and the results are presented in this chapter. Although simple, and without vacuum feedthroughs, the new oven still has low power consumption. The measured atomic flux and beam collimation closely follow our theoretical estimations. We also analysed the thermal losses in the oven and found that radiative heat loss become more comparable to the heat loss by conduction under higher temperature, but the heat loss by convection is dominant. This chapter also presents an analytical model describing the transverse absorption spectroscopy of an atomic beam, which agrees well with our experimental data.

3.1 Thermal performance of the oven

3.1.1 Thermocouple measurements

There are five thermocouples attached to the oven and MOT chamber that monitor the temperature at: the oven's heated end, the strontium reservoir (oven body), the bottom flange welded to the oven, the vacuum tube surrounding the oven, the far-end of the MOT chamber, and the surface of one of the quadrupole-field coils for MOT trapping. The strontium reservoir (oven body) is the key part where the strontium metal pieces are heated to create a vapour. (The reservoir temperature is also referred as the 'oven temperature' in following chapters.) Temperatures measured by those thermocouples are shown in Fig 3.1, for operations above 400 °C. Data for a wider range can be found in the Appendix A.1.

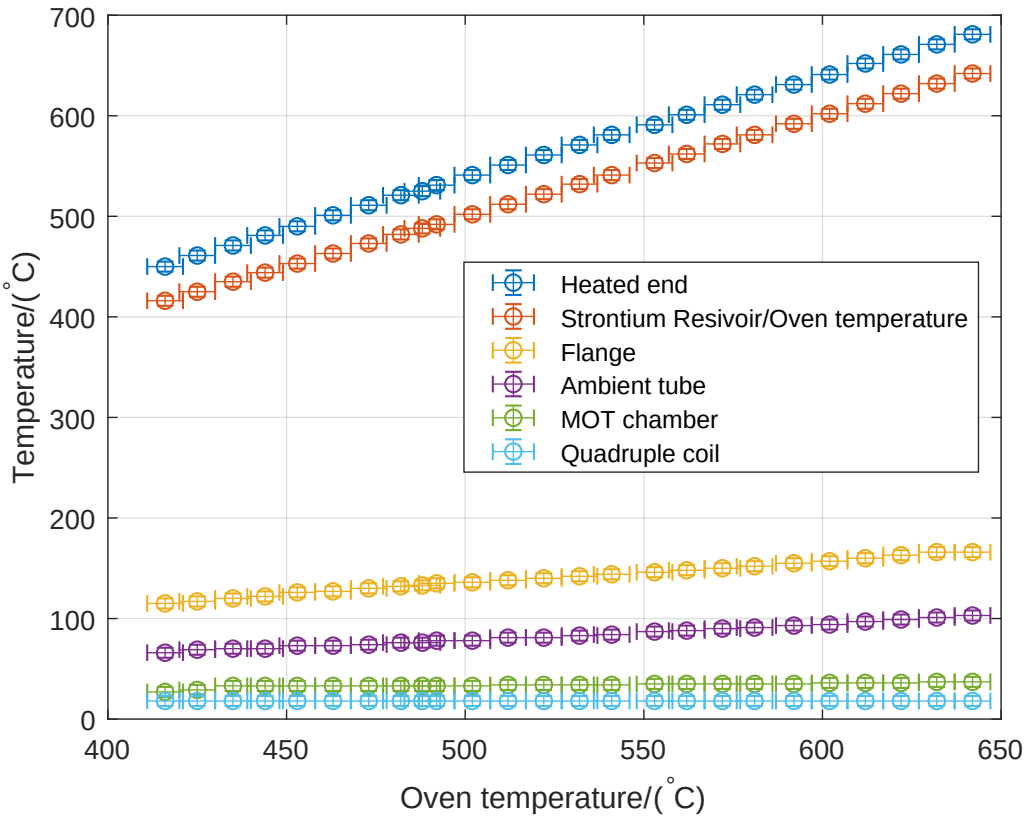


Figure 3.1: The heated end of oven, in contact with the hot end of the heaters, is hotter than the oven reservoir by about 40 °C. A thin-wall tube connecting the base flange and the oven body limits the heat flow and reduces the heat loss by conduction. It also ensures that the flange's temperature does not rise above 200 °C. The tube around the oven is heated by both radiation and conduction. The far end of the MOT chamber stays around 35 °C, which is close to the room temperature (about 22 °C). The quadrupole coils are water-cooled, so they would not be burned with high current going through. The uncertainty of temperature measurements comes from the inaccuracy of K-type thermocouples, which is ±5 °C.

3.1.2 Power consumption

The oven body is heated with cartridge heaters in order to generate enough strontium vapour. Heat sent in the oven equals to the power consumption of all the heaters, and dissipates into the apparatus and surrounding air. Once the thermocouple reading for the heated end has been stabilised by the temperature control unit (TCU) and oven temperature reaches equilibrium, the voltage and current can be read out from the bench-top power supply, providing one way to measure the total power consumption of the oven. The temperature of the oven is stabilised by the on-off PID TCU with a duty cycle percentage C, which refers to the fraction of time that the heaters are

switched on. For a power supply working with current I and voltage V connecting the TCU, the power of the oven at equilibrium state is

$$P = CVI \tag{3.1}$$

The power consumption is shown below in Fig 3.2.

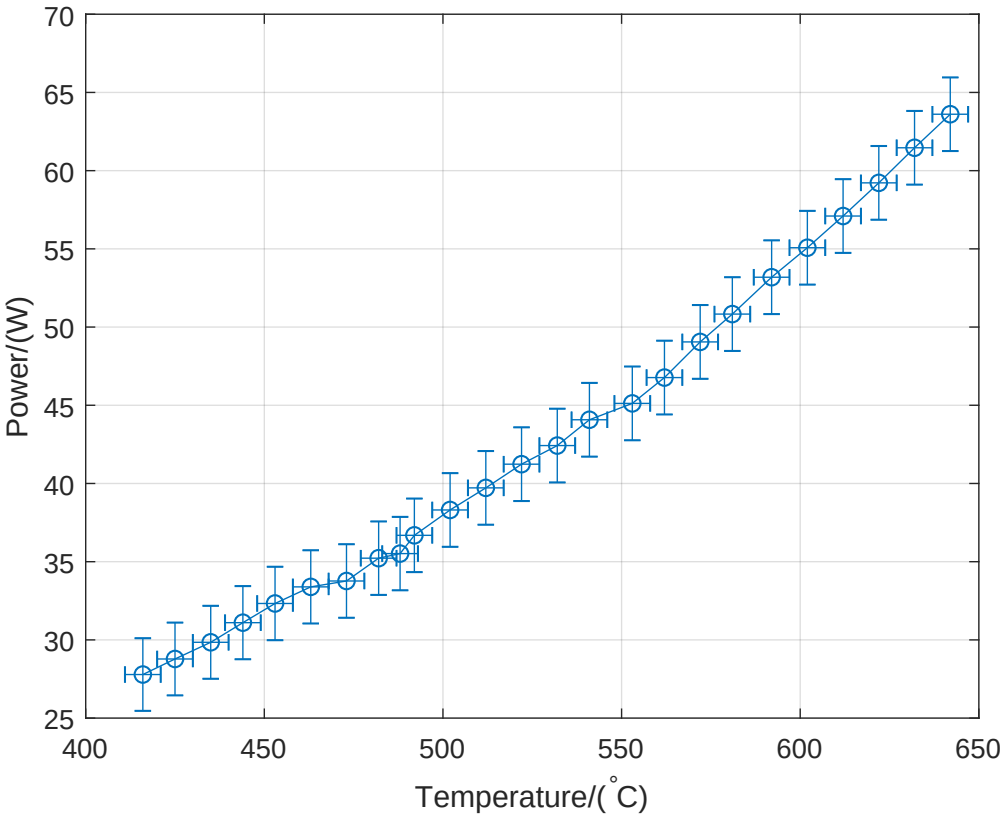


Figure 3.2: The power consumption is no more than 65 W when the oven temperature is below 650 °C.

3.1.3 Heat loss by conduction, radiation and convection

The heaters are powered by a programmable bench power supply (TENMA, 72-2540, 30 V and 5 A), from which the voltage and current can be read out. The total power input is equal to the total heat loss from:

- conduction through the oven body and along the metal connection to the chamber (the heat sink);
- radiation from the surface of the oven into the surrounding parts of the chamber;

- air convection.

We can estimated the heat loss by these mechanisms from the measured temperatures. The detailed structure of the oven is shown in Fig 3.3. The re-entrant oven can be

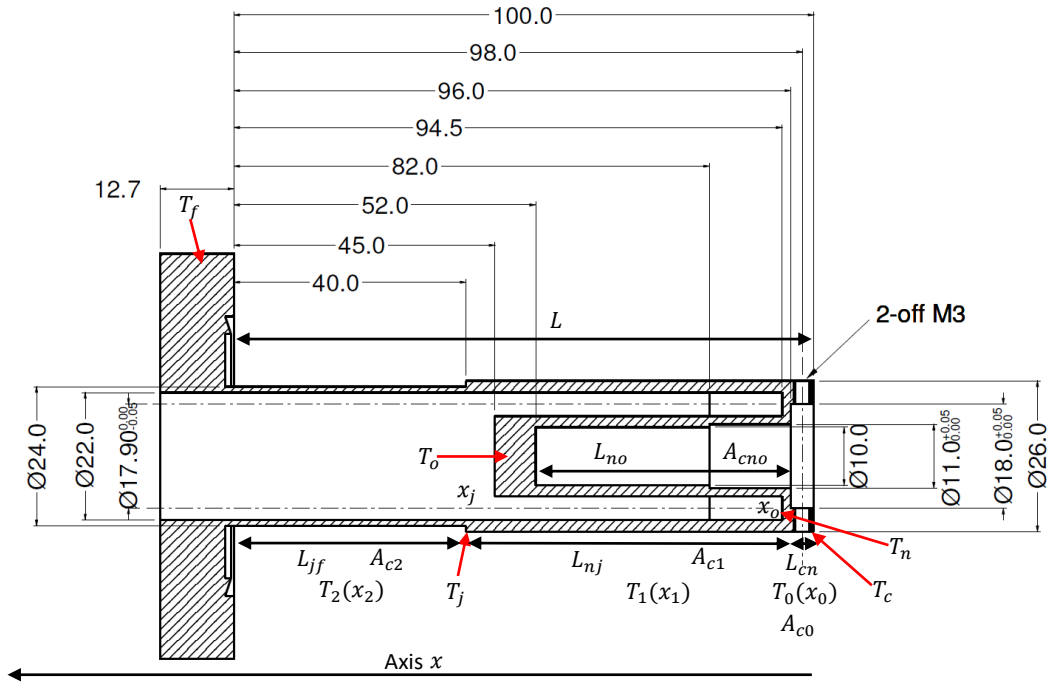


Figure 3.3: We can treat the oven as three cylindrical tubes connecting each other, marked as L_{cn}(cap to nozzle), L_{nj}(nozzle to joint) and L_{jf}(joint to flange). Thermocouples are used to monitor the oven temperature T_o and the temperature near nozzle and heaters T_n.

treated as two cylindrical tubes joined together, which are mounted on a standard CF40 flange with central hole. The thin-wall design reduces the heat conduction and a cylindrical heat shield around oven body reduces the power of radiation emitted into the chamber. Heat is lost by convection from the backside surface of the oven. To analyse, estimate and compare three heat loss mechanisms, we can begin with the simple case of a cylindrical tube, as shown in Fig 3.4, with inner diameter r_i, outer radius r_o and length L; the temperature is T_l at $x = 0$ and T_r at $x = L$. The cylindrical tube is under vacuum, so we can ignore the heat loss by convection. The cross-sectional area is

$$A_c = \pi(r_o^2 - r_i^2), \tag{3.2}$$

and an element of the surface area (as defined in Fig 3.4) is

$$dS = 2\pi r_o dx. \tag{3.3}$$

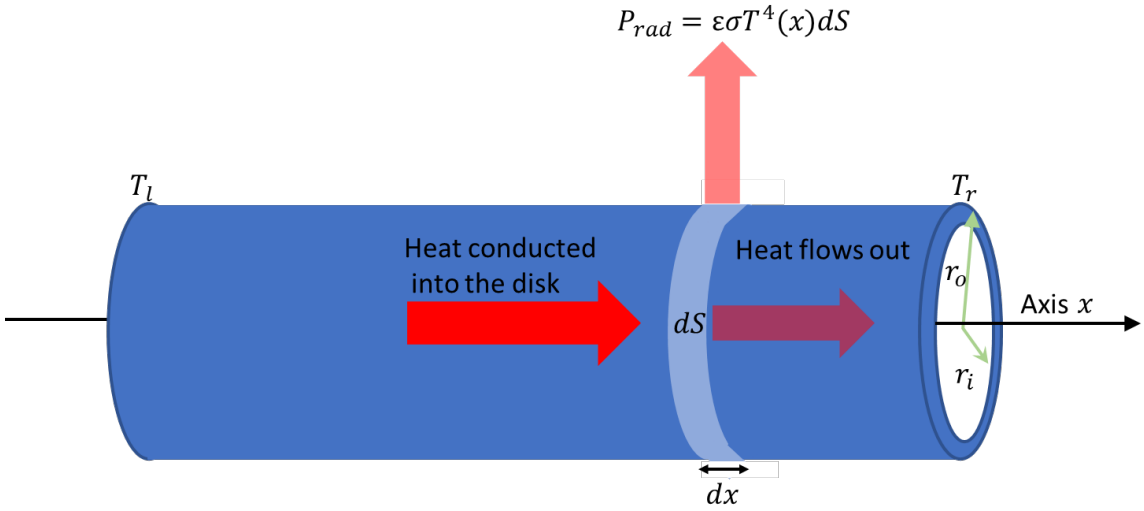


Figure 3.4: This is a simple cylindrical tube under vacuum without any heat loss by convection.

For a homogeneous uniform tube with cylindrical symmetry, Fourier's law gives the heat conduction rate at x as

$$\dot{Q}(x) = -\kappa A_c \frac{dT}{dx}, \tag{3.4}$$

where κ is the thermal conductivity of the material. The power radiated out from the surface element is

$$dP_{rad} = \varepsilon\sigma T^4 \, dS, \tag{3.5}$$

where σ is the Stefan-Boltzmann constant, and ε is the emissivity of the surface (stainless steel 304 for our oven).

In fact, the radiation emitted from the tube's surface is not fully absorbed by the surrounding chamber. A more realistic scenario is that the radiation is partially absorbed and partially reflected back to the tube's surface. One round of the radiation exchange has been shown in Fig 3.5. A grey-body with emissivity ε and absorptivity α has a reflectivity $\rho = 1 - \alpha$, according to Kirchhoff's law of thermal radiation[36], $\varepsilon = \alpha$. The net radiation loss from the surface can be calculated as the sum of a series reflections, as shown in Fig A.4 (and further details can be found in Appendix A.2). We inserted a cylindrical stainless steel heat shield between the oven and chamber as shown in Fig A.5, which reduces the radiative heat loss by about a factor of 2 (see Appendix A.3). We measured the ambient chamber temperature T_{am} with a

thermocouple. The radiation heat loss from surface element dS at position x is

$$dP_{lr} = \frac{\sigma}{2}\frac{\varepsilon,}{2-\varepsilon}(T^4 - T_{am}^4)\,dS \tag{3.6}$$

$$= \frac{\varepsilon\sigma\pi r_o}{2-\varepsilon}(T^4 - T_{am}^4)\,dx. \tag{3.7}$$

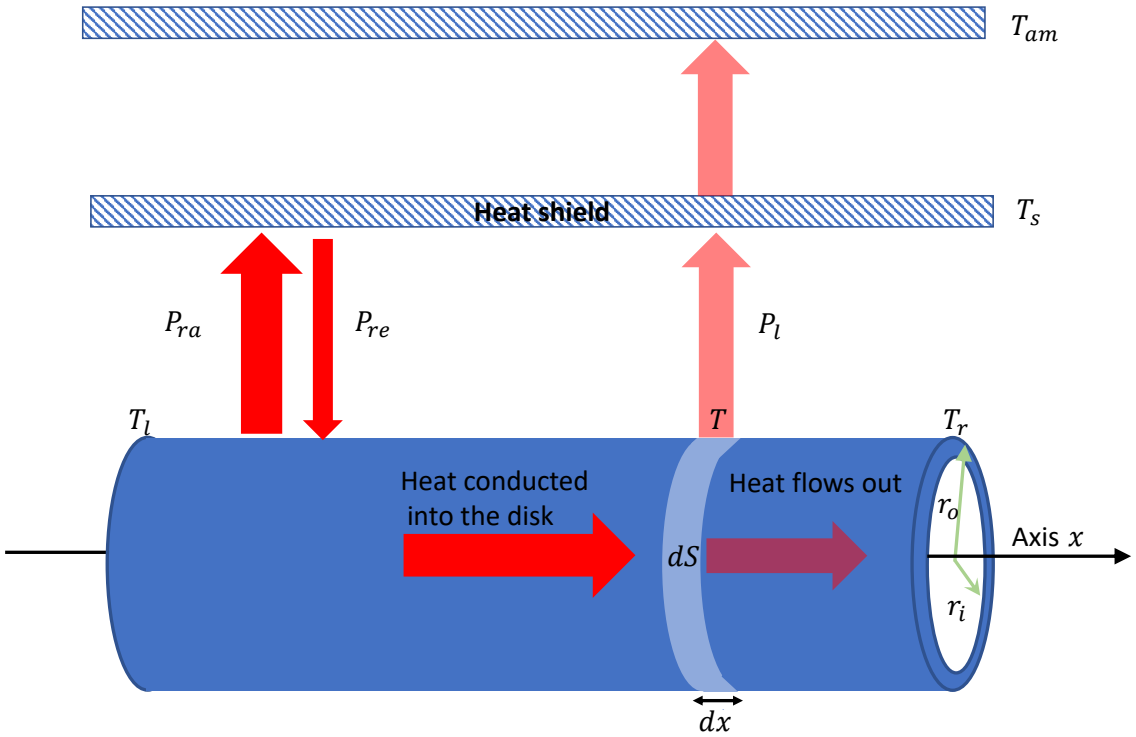


Figure 3.5: Heat exchange between the tube's outer surface and the surrounding chamber happens by radiation.

Heat conduction rate at x follows this condition:

$$\dot{Q}(x) = \dot{Q}(x + dx) + dP_{lr} + dP_{air}, \tag{3.8}$$

where dP_{lr} is the element of the radiative heat loss from the surface element dS, and dP_{air} is the heat convection from the inner side of the tube (since the inner side of the oven is exposed to air while the outer surface is in vacuum). Numerical simulation tools such as COMSOL could be used to find a precise temperature distribution, but simple estimates are sufficient to aid the design for better ovens.

For example, for the strontium reservoir part, radiation is contained inside the reservoir, and there is no convection as the reservoir is under vacuum. So, we can get

$$\dot{Q}(x) = \dot{Q}(x + dx). \tag{3.9}$$

Then, we can get the temperature distribution over the inner surface of the oven $T_{in}(x)$ as a linear function:

$$T_{in}(x) = \frac{T_o - T_n}{L_{no}} x + T_n. \tag{3.10}$$

For heat loss from the outer surface, we can do a similar estimation and use the linear distribution to describe it. An estimation can be found in Appendix A.4. The estimated heat loss by radiation, conduction and air convection is shown in Fig 3.6. The dominant heat loss is by air convection, while heat loss by radiation and conduction are comparatively small due to thin-wall oven body and the existence of the heat shield. Heat loss by radiation is less than that by conduction below 425 °C.

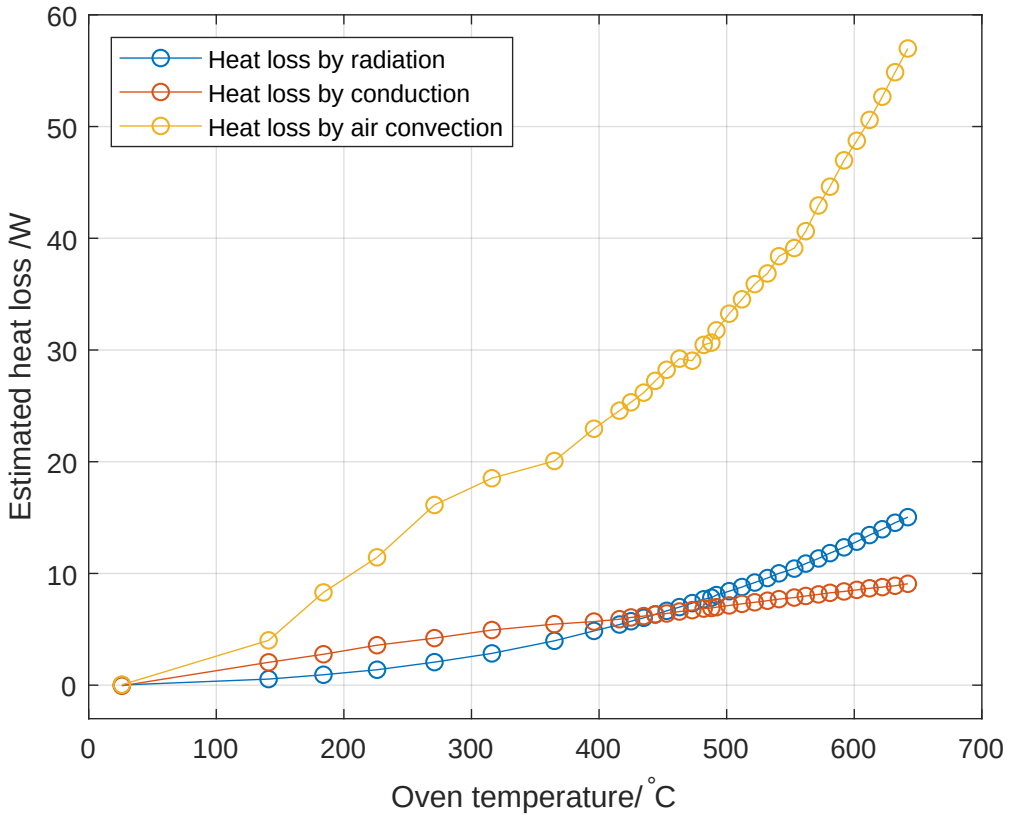


Figure 3.6: The dominant heat loss is by air convection, since part of oven is in contact with air directly. Heat loss by radiation surpasses that by conduction around 425 °C and they are both much smaller compared with heat loss by air convection, due to the thin-wall oven design and the existence of the heat shield.

3.1.4 Conductivity of strontium vapour

The thermal conductivity of strontium vapour can be calculated using the kinetic theory expression for a gas[12]

$$\kappa_{gas} = \frac{2}{3\sigma} c_{atom} \sqrt{\frac{k_{\mathrm{B}} T}{\pi m}}, \tag{3.11}$$

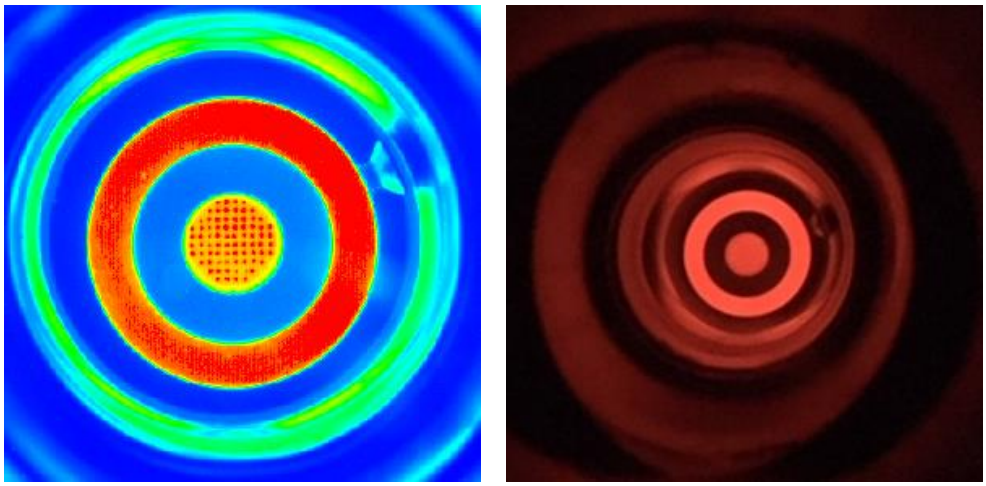
where $c_{atom} = c_{mol}/N_A$ is the heat capacity per atom, c_{mol} is the mole heat capacity, N_A is the Avogadro constant and σ is the collision cross section of the atoms. The thermal conductivity of a gas is independent of pressure. We can work out that the thermal conductivity of strontium at 900 K is $10\,\mathrm{mW\,m^{-1}\,K^{-1}}$. This is negligible compared to heat transfer by conduction along by the solid oven body or the heat loss by radiation.

3.1.5 Nozzle temperatures

We present two images of heated oven in Fig 3.7, which were taken through a viewport opposite to the oven. In Fig 3.7a, red regions refer to higher pixel counts and green regions refer to lower pixel counts, while blue regions are background pixels with nearly zero counts. The array of red circles in a honeycomb pattern is due to the radiation from the oven reservoir leaking through the nozzle holes, and the orange part of the honeycomb pattern is the graphite nozzle. The red ring around is the top end of oven, which was measured to be at 700 °C by a thermocouple. The pale blue ring between the red ring and the honeycomb is the stainless steel cap mounted on the oven body for securing the position of the nozzle. It is obvious that the cap's radiative emission is much weaker compared to that from the oven top, and is also weaker than the radiation of the graphite nozzle. It means the stainless steel cap is colder than the surrounding parts of oven and the nozzle. It reveals that heat transfer by conduction between components in direct contact is not significant under vacuum and heat transfer by radiation is dominant.

In Fig 3.7b, the similar phenomena can be observed. The black ring between the orange circle and ring is due to the metal cap, which has a much lower temperature than the surrounding components. This again reveals that heat transfer by conduction between two surfaces in contact is very small in vacuum, as is well known.

So the nozzle heats up mainly by radiation exchange and at final equilibrium the absorption and emission are balanced. The geometry of oven around the nozzle is not complicated, but still subtle with a few small components. The equilibrium temperatures of the nozzle are depicted in Fig 3.8. Although our nozzle temperature is



(a) Flase color image. (b) Real color image

Figure 3.7: Pictures of the front face of the spectroscopy oven and nozzle taken when it is heated to 613 °C. (a) a picture by a standard CCD camera (PixeLINK PL-B741) with pixel counts in rainbow-coloured mode. (b) a picture taken by a cell-phone camera(Note that the glass viewports of the vacuum system would be opaque to a thermal imaging camera).

lower than the oven temperature by 30 °C, we did not observe any clogging apart from one test, in which we heated the oven temperature up to 600 °C within 30 minutes.

The emissivity of the material does not affect the nozzle's equilibrium temperature. If we change the material of nozzle from graphite ($\varepsilon_g = 0.98$) to stainless steel($\varepsilon_g = 0.22$), the nozzle's temperature would still be 461 °C at equilibrium, but low-emissivity material will require a longer time to reach equilibrium.

The major factor that limits the nozzle's temperature is how much surface area is facing towards the cold background since in these directions none of the radiated heat returns. Thus inserting the nozzle deeper into the oven can help to increase its temperature by reducing the solid angle of emission towards a cold background.

3.2 Flux measurement by absorption spectroscopy

3.2.1 Doppler-broadened absorption spectroscopy

As shown in Fig 3.9, a laser beam propagates horizontally through the vertical atomic beam, and the power of the laser beam after passing through the atoms is measured by a photodiode. By scanning the frequency of the probe beam around resonance, we record a Doppler-broadened absorption peak, which reveals information about the angular dependence of the atomic beam and its flux.

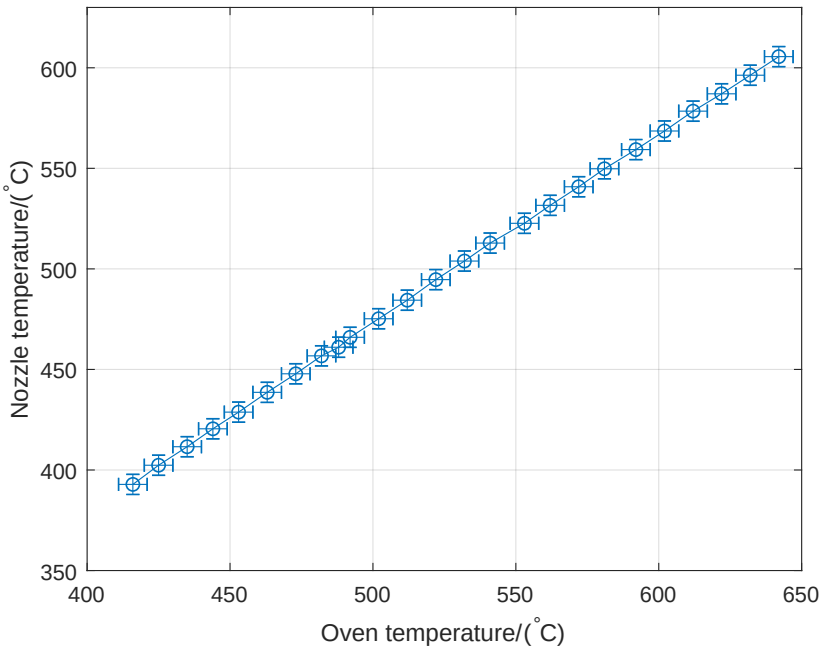


Figure 3.8: The equilibrium temperature of the nozzle under radiation has a nearly linear dependence on the oven temperature and is constantly lower than the oven temperature by 30 °C.

The number density and velocity distribution of atoms depend on the position z. we start the calculation of the spectroscopy signal from Beer's law. We first consider the absorption for a slice of atoms at position z, as shown in 3.10 and then integrate over the whole length. (This assumes that the laser beam passes through the centre of the atomic flux and the system is adjusted to achieve that.) For a slice of sample with thickness dz, volume number density $n(v)$ for atoms with velocities between v and $v+dv$, there are $n(v)dz$ atoms per unit area. Therefore, $n(v)\sigma dz$ is the fractional loss of intensity, where the cross-section $\sigma(\omega, I, v)$ characterises the probability of photon-atom interaction. According to Beer's law, the element change of the intensity dI is

$$\frac{dI}{dz} = -\kappa(\omega)I, \tag{3.12}$$

where $\kappa(\omega)$ is the absorption coefficient, which is dependent on the angular frequency of the light ω as

$$\kappa(\omega) = \int n(v)\sigma(\omega, I, v)dv, \tag{3.13}$$

$$\sigma(\omega, I, v) = \frac{\sigma_0}{1 + I/I_{sat} + 4(\omega - \omega_0 - kv\sin\theta)^2/\Gamma^2}. \tag{3.14}$$

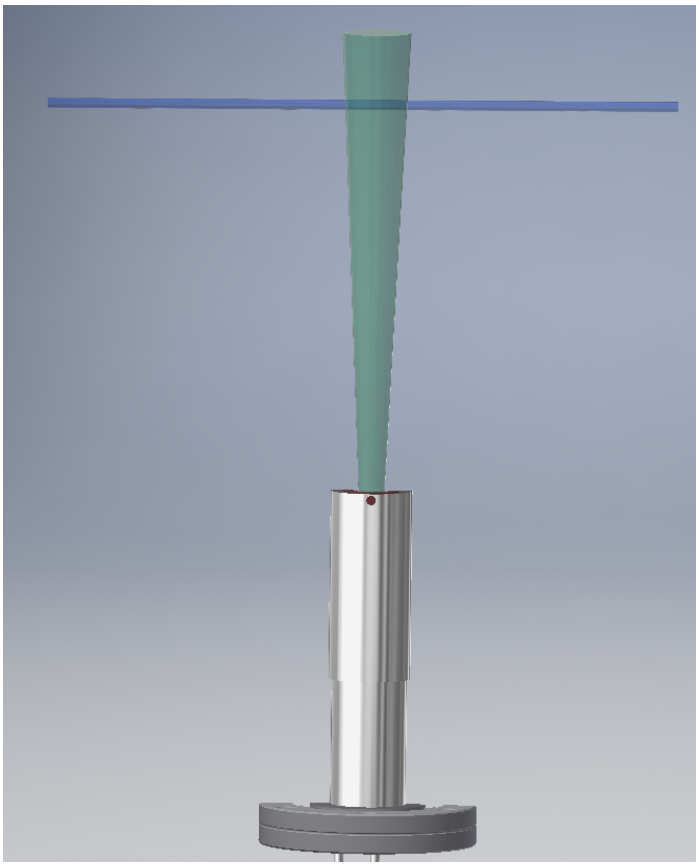


Figure 3.9: A horizontal laser beam travels through the vertical atomic beam and then the absorption signal is recorded by a photodiode.

where $k = 2\pi/\lambda$ is the angular wave number for the light. $n(v)$ can be derived by expressing the flux within the angle θ to $\theta + d\theta$ with two approaches. The volume of the ring is $2\pi|z|Rd\theta$, so the atomic flux at θ contributed by atoms with velocity between v and $v + dv$ can be expressed as

$$d\Phi_{ring} = n(v)v2\pi|z|Rd\theta. \tag{3.15}$$

This can also be expressed in terms of solid angle as

$$d\Phi_{ring} = f_n(v)I(\theta)d\Omega = f_n(v)I_0 j(\theta)d\Omega, \tag{3.16}$$

where $f_n(v)$ is the probability density distribution function of velocity for atoms in an atomic beam and $d\Omega$ is the element of solid angle for the ring. Then eqn. (3.16) can be written with $f(v)$

$$d\Phi_{ring} = f(v)I_0 j(\theta)d\Omega. \tag{3.17}$$

So, we can get that the number density of atoms $n(v)$ with velocity between v and $v + dv$ and within angle θ to $\theta + d\theta$ is given by

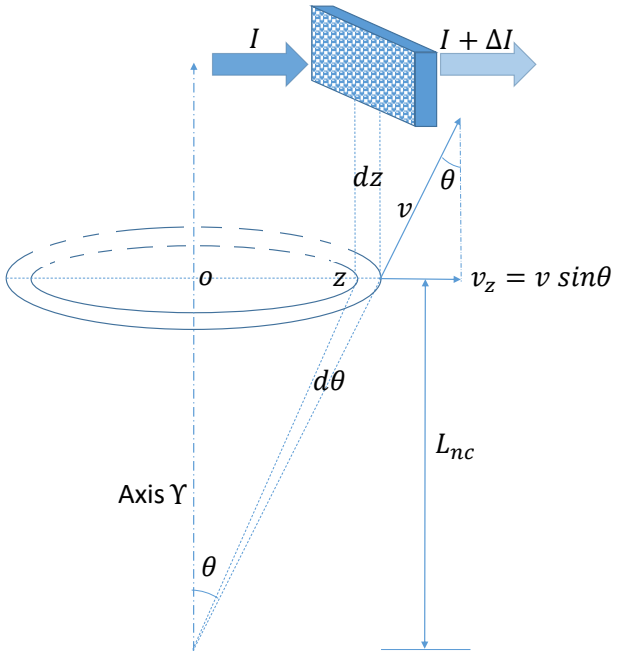


Figure 3.10: The geometry for a horizontal laser beam of intensity I interacting with atoms in a volume element at angle θ to the vertical axis (the centre line).

$$
\begin{aligned}
n(v)v2\pi|z|dz &= f_b(v)I_0 j(\theta)d\Omega, \\
n(v)v2\pi|z|Rd\theta &= f_b(v)I_0 j(\theta)2\pi\sin\theta d\theta, \\
n(v)v2\pi R\sin\theta Rd\theta &= f_b(v)I_0 j(\theta)d\Omega, \\
n(v) &= \frac{f_b(v)I_0 j(\theta)}{vR^2}, \\
n(z,v) &= \frac{f_b(v)I_0 j(\theta)}{v(L_{nc}^2+z^2)}.
\end{aligned} \tag{3.18}
$$

When the initial beam intensity I_{in} is very small compared with saturation intensity I_{sat}, the cross section can be treated as depending only on the frequency ω and the velocity of atoms v

$$
\sigma(\omega,v) = \frac{\sigma_0}{1+I_{in}/I_{sat}+4(\omega-\omega_0-kv\sin\theta)^2/\Gamma^2}. \tag{3.19}
$$

By integrating eqn. (3.12), we can get

$$
D_a(\omega) = -\int_z\int_v n(z,v)\sigma(\omega,I,v)dvdz, \tag{3.20}
$$

$$
I(\omega,L) = I(\omega,0)e^{-D_a(\omega)}, \tag{3.21}
$$

where D_a is called the absorption depth. The velocity component along the laser beam path is

$$v_z = \frac{z}{\sqrt{L_{nc}^2 + z^2}} v. \tag{3.22}$$

Hence carrying out the double integration on the right hand of eqn. (3.20) gives

$$\begin{aligned} D_a &= \int_z \int_v \frac{f(v) I_0 j(\theta)}{v(L_{nc}^2 + z^2)} \cdot \frac{\sigma_0}{1 + I_{in}/I_{sat} + 4(\delta - kv\sin\theta)^2/\Gamma^2} dv dz, \\ &= I_0 \int_z \int_{v_z} \frac{f\left(\frac{|v_z|\sqrt{L_{nc}^2+z^2}}{|z|}\right) j\left(\tan^{-1}(\frac{|z|}{L_{nc}})\right)}{|v_z|(L_{nc}^2 + z^2)} \cdot \frac{\sigma_0}{1 + \frac{I_0}{I_{sat}} + \frac{4(\delta - kv_z)^2}{\Gamma^2}} dv_z dz. \end{aligned} \tag{3.23}$$

where the frequency detuning $\delta = \omega - \omega_0$ and $v_z = v\sin\theta$.

$$\begin{aligned} dz \sin(\frac{\pi}{2} - \theta) = Rd\theta &= \frac{L_{nc}}{\cos\theta} d\theta, \\ dz &= \frac{L_{nc}}{\cos^2\theta} d\theta. \end{aligned} \tag{3.24}$$

Also, the absorption depth can be calculated by integrating over θ

$$\begin{aligned} D_a &= \int_\theta \int_v n(v)\sigma(\delta, v) dv d\theta, \\ &= I_0 \int_\theta \int_v \frac{f_b(v) j(\theta)\sin\theta}{v|z|\sqrt{L_{nc}^2 + z^2}} \frac{\sigma_0}{1 + I_{in}/I_{sat} + 4(\delta - kv\sin\theta)^2/\Gamma^2} dv dz, \\ &= I_0 \int_\theta \int_v \frac{f_b(v) j(\theta)\sin\theta}{vL_{nc}\tan\theta L_{nc}/\cos\theta} \frac{\sigma_0}{1 + I_{in}/I_{sat} + 4(\delta - kv\sin\theta)^2/\Gamma^2} dv \frac{L_{nc}}{\cos^2\theta} d\theta, \\ &= I_0 \int_\theta \int_v \frac{f_b(v) j(\theta)}{vL_{nc}} \frac{\sigma_0}{1 + I_{in}/I_{sat} + 4(\delta - kv\sin\theta)^2/\Gamma^2} dv d\theta. \end{aligned} \tag{3.25}$$

The expressions in Eqns 3.23 and 3.25 both yields the same lineshape but the integration with respect to θ is easier to handle numerically than the one with z. So, we can evaluate $D_a(\omega, T_v)$ for a given geometry of the nozzle (in the collision free-mode), under the temperature of the strontium vapour T_v, and the frequency detuning δ.

3.2.2 Measurements of atomic flux

With the oven temperature stabilised to T_o, the strontium vapour temperature stays at T_v. We can scan the laser frequency over 2 GHz to record the Doppler broadened lineshape $I(\omega, T_v) \propto \exp(-D_a(\omega, T_v))$. We can send part of the light into the etalon with a free spectral range of 300 MHz for the frequency calibrations. We use a polarising beam splitter (PBS) and quarter-wave plate to ensure that light goes through

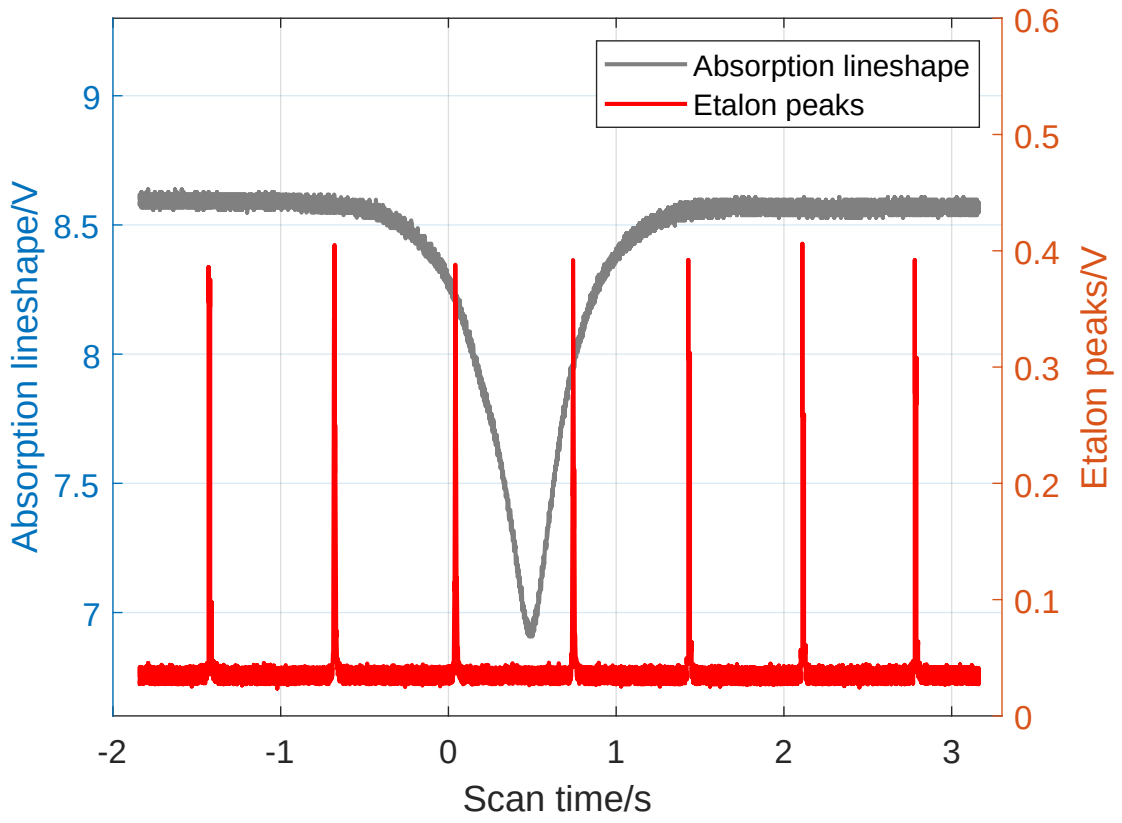
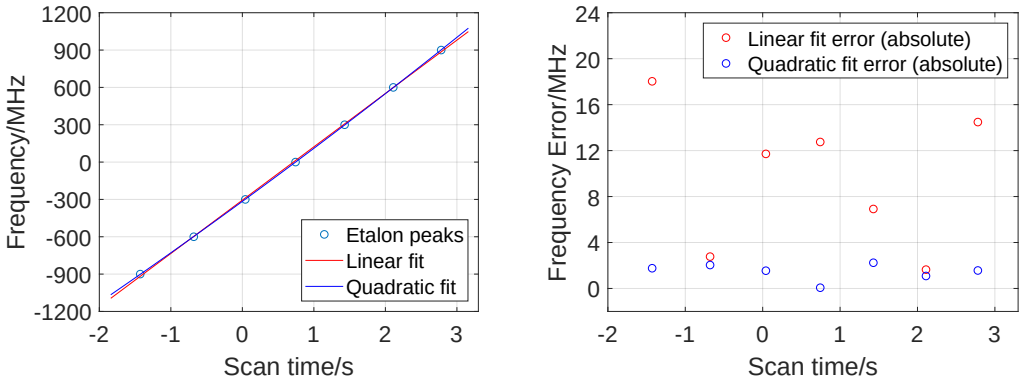


Figure 3.11: This figure presents the raw data plot of the photodiode's reading over the scan time, which corresponds to the intensity of light after being absorbed, together with seven etalon peaks spaced by 300 MHz (the free spectral range of the etalon).

the atomic sample is circularly polarised and there is no component from the other handedness. A typical absorption trace is shown in Fig 3.11.

To convert the scan time into corresponding frequency, we first locate the etalon peaks on the scan time domain: $t_1, t_2, \cdots, t_7$ and assign frequencies to each peak, $f = f_0 + p \cdot FSR (p = 1, 2, \ldots, 7)$ where $FSR = 300$MHz and the offset f_0 is not important. The frequency scan is expected to be approximately linear, but we find that quadratic fitting gives better accuracy, as shown in Fig 3.12. We use the parameters from the quadratic fit to convert the absorption trace into a lineshape on the frequency domain. The etalon does not provide an absolute frequency reference, so we have to include another fitting parameter $\omega_0 = 2\pi f_0$ in the model. And the equation for fitting the normalised absorption lineshape is

$$I(\omega)/I_{in} = e^{-D_a(\omega-\omega_0,T_v)}. \tag{3.26}$$



(a) Etalon peak points with the fits. (b) The fitting errors

Figure 3.12: (a) The linear and quadratic models fit the data points representing the position of each etalon peak. (b) The absolute values of the error for the linear and quadratic models. The inaccuracy of fitting for the quadratic model is ±2.5MHz.

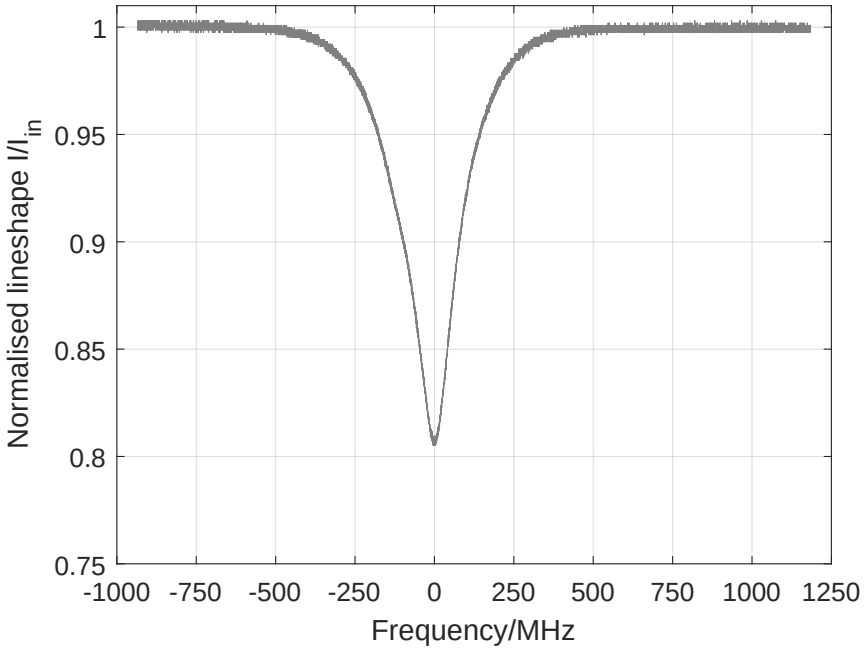


Figure 3.13: The absorption lineshape is normalised to unity and shifted in frequency so that the minimum sits at $f = 0\,\text{MHz}$. The absorption profile for one isotope is symmetrical but the measured profile is the combination of profiles for four isotopes so it is asymmetrical.

A Voigt profile, as shown in eqn. 3.27, is a convolution of a Cauchy-Lorentz distribution (natural linewidth) and a Gaussian distribution (velocity distribution) and

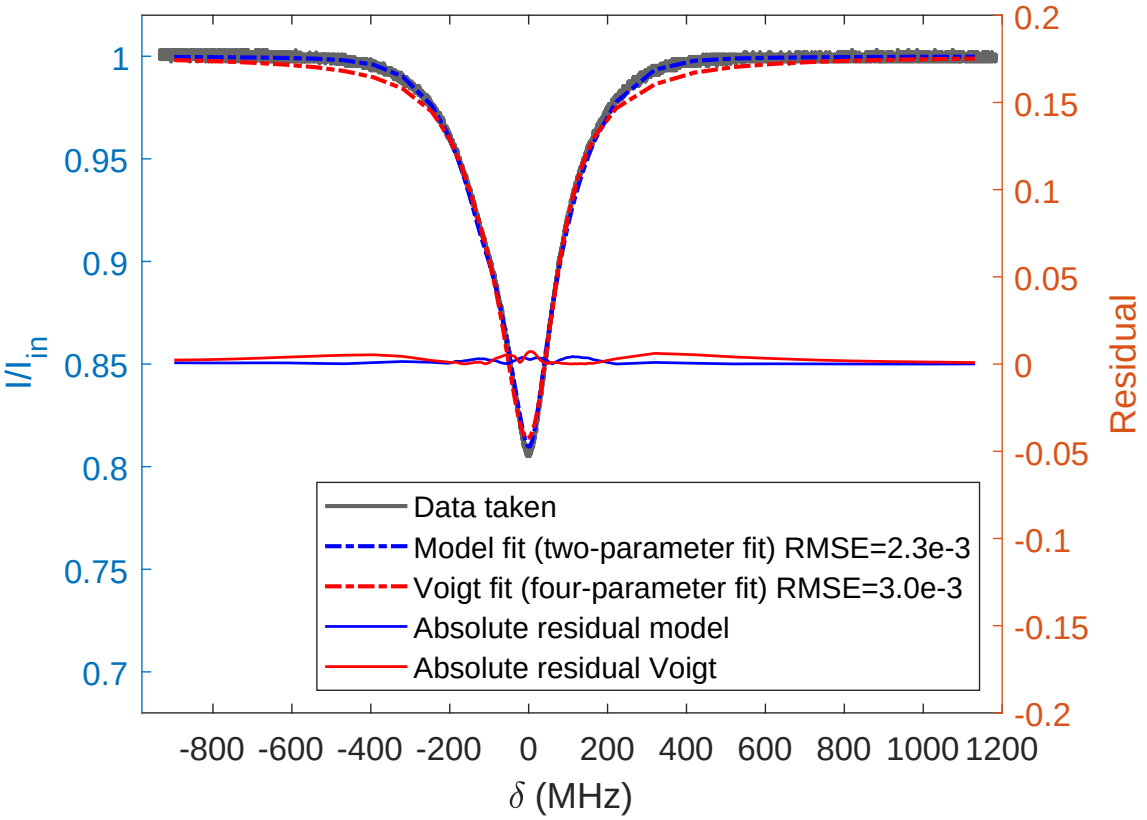


Figure 3.14: The absorption with the frequency measured from the point of maximum absorption. The root-mean-squared error for fitting with a Voigt profile is higher than for our derived model and there are observable differences. The fitted vapour temperature $T_v = 416\,^{\circ}\mathrm{C}$ is considerably lower than the measured oven temperature of $488\,^{\circ}\mathrm{C}$

is a common fitting model for absorption lineshapesRef [64].

$$
\begin{aligned}
I(\omega)/I_{in} &= 1 - A \int_{-\infty}^{\infty}, G(\omega') L(\omega - \omega_0 - \omega')\, d\omega', \\
G(x) &= \frac{e^{-x^2/(2\sigma^2)}}{\sigma\sqrt{2\pi}}, \\
L(x) &= \frac{\gamma}{\pi(x^2 + \gamma^2)}.
\end{aligned}
\tag{3.27}
$$

Therefore, for comparison, we also fit the absorption signal with a Voigt profile. Our model gives a lower root-mean-squared error (RMSE) with only two fitting parameters as compared to the Voigt profile using four free parameter in the fitting (A, σ, $\gamma\,\omega_0$). The fitted parameters derived from a Voigt profile do not reveal physical meanings such as velocity and linewidth directly. Whereas we expect our model to give an accurate vapour temperature T_v in the collision-free regime. By knowing T_v, the

total flux can be calculated

$$\Phi = \frac{WPA}{\sqrt{2\pi m k_B T_v}} \tag{3.28}$$

where m is the mass of a strontium atom, A is the total area of holes on the nozzle and P is the vapour pressure at T_v.

3.3 Opaque mode

The collision-free regime works when the Knudsen number $K_{nL} \geq 10$, which means the vapour temperature should be under 474 °C for our nozzle ($L = 4$ mm and $D = 0.4$ mm). For higher vapour temperature, the RMSE will increase, e.g. when the oven is heated to $T_o = 592$ °C, the RMSE rises to 1.5×10^{-2}.

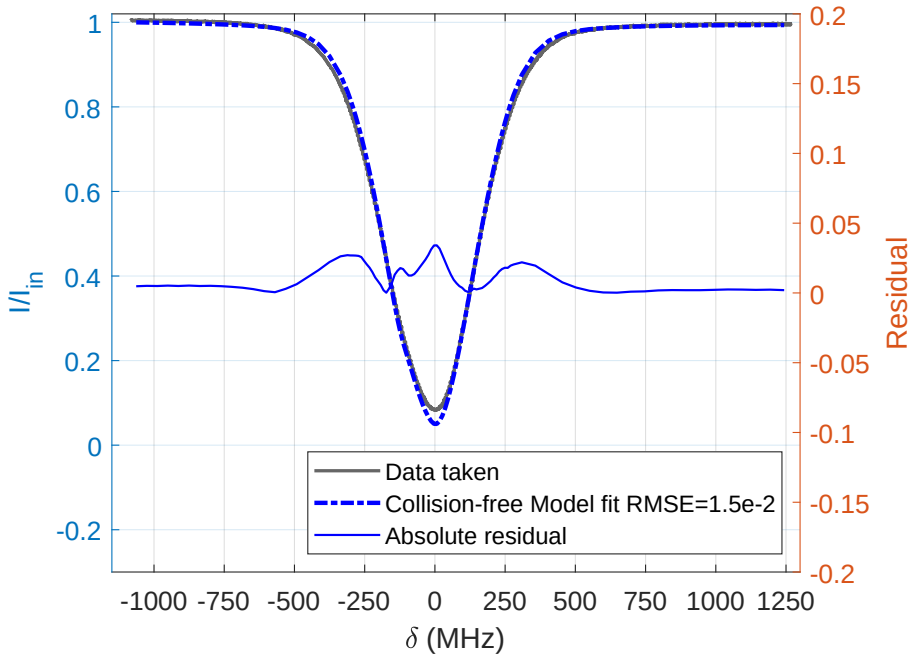


Figure 3.15: When the oven is heated above the collision free mode's threshold $T_v = 474$ °C. Error of fitting the absorption profile with collision-free model will increase. $T_v = 501$ °C, while the oven temperature is at 592 °C.

When $\beta \leq K_{nL} \leq 10$, the temperature starts to affect both the angular dependence and centerline intensity of the atomic flux, while the transmission probability of Clausing W can still predict the total flux[21, 12].

An important assumption for opaque mode is that number density along the tube is a linear function of position.

$$n(z) = n(0)[\xi_1 - (\xi_1 - \xi_0)(\frac{\Upsilon}{L})], \tag{3.29}$$

where υ is the distance from the entrance of the tube, as shown in Fig 2.14. Then we can list out the formula for $j(\theta)$ under opaque mode.

$$\begin{aligned}
\varrho &= \frac{\xi_0}{[2K_{nL}(\xi_1-\xi_0)]^{1/2}},\\
\varrho' &= \varrho(\cos\theta)^{-1/2},\\
F &= \frac{2}{\sqrt{\pi}}\varrho'\frac{(1-\xi_1)}{\xi_0}e^{-(\varrho'\xi_1/\xi_0)^2},\\
S(q) &= \int_0^q (1-t^2)^{1/2}\big(\operatorname{erf}\big\{\varrho'[1+\frac{\beta t(\xi_1-\xi_0)}{\tan\theta\xi_0}]\big\}-\operatorname{erf}\varrho'\big)\,dt.
\end{aligned} \tag{3.30}$$

The angular dependence follows this equation when $q \le 1$

$$j(\theta) = \frac{2}{\sqrt{\pi}}\xi_0\cos\theta\frac{e^{\varrho'^2}}{\varrho'}\big[\frac{R}{2}(\operatorname{erf}\frac{\varrho'\xi_1}{\xi_0}-\operatorname{erf}\varrho'+F)+S(q)\big]+\xi_0\cos\theta, \tag{3.31}$$

and the angular dependence for $q \ge 1$ is

$$j(\theta) = \xi_0\cos\theta+\frac{2}{\sqrt{\pi}}\xi_0\cos\theta\frac{e^{\varrho'^2}}{\varrho'}S(1). \tag{3.32}$$

Along the centre line, angular dependence is

$$j(0) = \xi_0+\frac{\sqrt{\pi}}{2}\xi_0\frac{e^{\varrho^2}}{\varrho}(\operatorname{erf}\frac{\varrho\xi_1}{\xi_0}-\operatorname{erf}\varrho)+(1-\xi_1)\exp[-\varrho^2(\frac{\xi_1^2}{\xi_0^2}-1)]. \tag{3.33}$$

Ref[54] and Ref[65] both made mistakes in their peak intensity equations, the correct expression is shown in Eq. 3.33.

Before futher discussions about parameters ξ_0 and ξ_1, we should define transmission probability W. The theoretical atomic flux of an aperture is Φ_{total} and atomic flux existing off the end of a tube is Φ_{tube}. Then we can define transmission probability W as

$$W = \frac{\Phi_{tube}}{\Phi_{total}}, \tag{3.34}$$

and we know that

$$\begin{aligned}
\Phi_{tube} &= \int_0^{2\pi} I(\theta)d\Omega,\\
&= \int_0^{\pi/2} I(\theta)2\pi\sin\theta d\theta,\\
&= \Phi_{total}2\int_0^1 j(\theta)\,d\cos\theta,
\end{aligned} \tag{3.35}$$

then the W can be expressed as

$$W = 2\int_0^1 j(\theta)\, d\cos\theta. \tag{3.36}$$

In the collision-free mode, the angular dependence $j(\theta)$ is only dependent on the geometry of the nozzle; whereas in the opaque mode, $j(\theta)$ is dependent on the vapour temperature and the values of ξ_0 and ξ_1. Various investigators have explored solutions for ξ_0 and ξ_1, and their derivations lead to similar results for the angular dependence $j(\theta)$, apart from the Giordmaine and Wang model and Becker's model. There is no experimental proof of superiority of a particular model[54].

Zugenmaier's model[83] gives transmission probability W as

$$W = 4/(2 + k_z), \tag{3.37}$$

$$k_z = (\beta/3 + 2\beta u)^{-1}, \tag{3.38}$$

$$u = \beta/4 + [1 - (1 + \beta^2)^{3/2}]/(6\beta^3). \tag{3.39}$$

Olander's model([54]) is based on integral constraints and the equation is

$$\xi_0 = \frac{1}{2}\int_0^2 \frac{j(\theta)}{\cos\theta}\, d(\cos\theta), \tag{3.40}$$

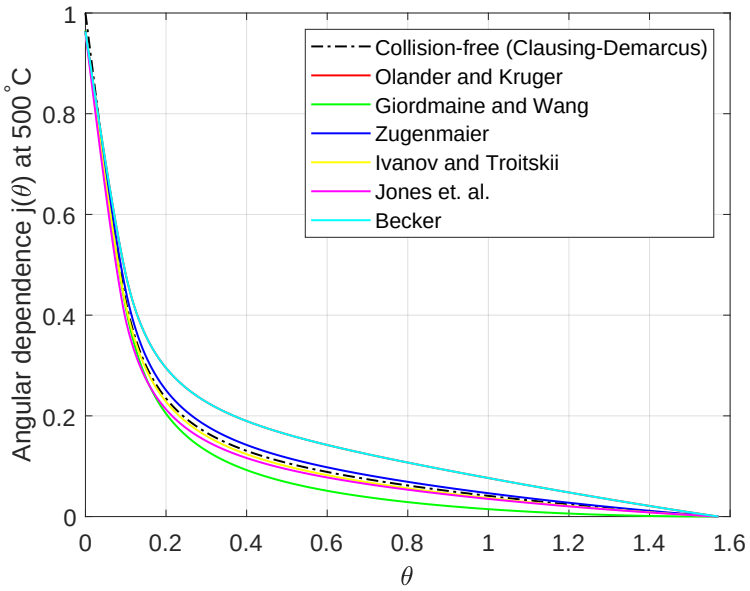
and W used in Olander model is the same as that derived in Clausing-Demarcus model[25]. Ivanov and Troitskii[33] model gives solutions for ξ_0 and ξ_1 as

$$\xi_0 = \xi_1 - \frac{(1 + 2/\beta)(1 + 1/\beta^2)^{1/2} - (1 + 2/\beta^2)}{(1 + 1/\beta^2)^{1/2} + 1}, \tag{3.41}$$

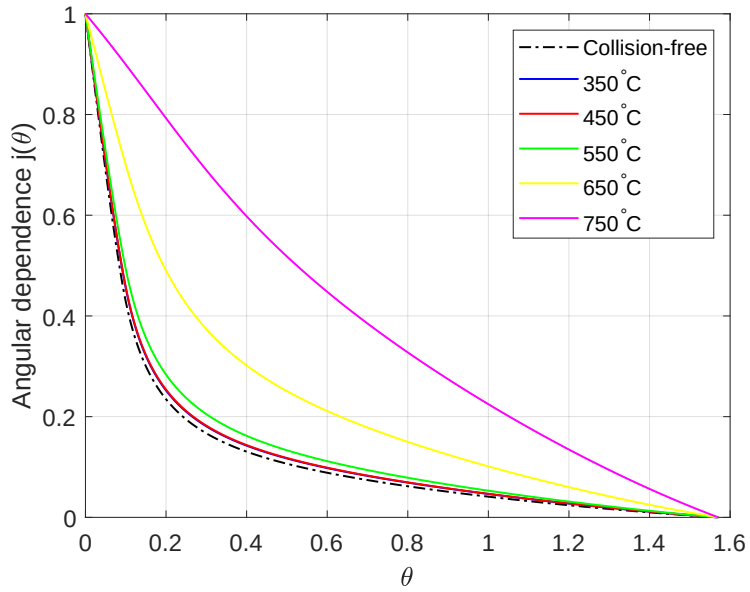
$$\xi_1 = \frac{2 + \beta^2}{2 + \beta(1 + \beta)}. \tag{3.42}$$

Ref[54] missed a pair of brackets when giving out the ξ_1 equation when citing the Ivanov and Troitskii model[33].

We can use the opaque model to fit the the absorption lineshape as shown in Fig 3.17, and the opaque model help to reduce the RMSE marginally, but the model's complexity asks for much longer computing time. Also, the fitted vapour temperature in opaque model is close to that in the collision-free model. So, collision-free model is still the most fast and efficient method to analyse absorption lineshapes taken in opaque mode, and it will increase the uncertainty of fitted vapour temperatures up to $\pm 12\,^{\circ}\mathrm{C}$. The transmission probability factor W (Clausing) used for calculating total flux can predict the flux until $K_{nL} \leq \beta$, but collimation becomes worse when entering the opaque regime.



(a) Angular dependence in various models under vapour temperature 500 °C



(b) Angular dependence varies over temperatures.

Figure 3.16: (a) All curves are calculated for a vapour temperature of $Tvap = 500\,°C$. Giordmaine's and Becker's models are distinguishable and others give very similar angular distributions.(b) Those angular dependence $j(\theta)$ curves have been normalised to equal enterline intensity and $\beta = 0.1$. The angular dependence curve calculated by opaque mode(Zugenmaier model) is close to that from collision-free model at 350 °C and 450 °C. At higher temperature, $j(\theta)$ have large values at larger θ, which means more atoms come off with large existing angle and collimation of the atomic beam has been compromised.

Model	Transmission probability W	ξ_0	ξ_1
Olander[54]	W(Clausing)	$\cdots$	eqn. (3.40)
Giordmaine and Wang[29]	$4\beta/3$	0	1
Zugenmaier[83]	eqn. 3.37	W/2	1
Ivanov and Troitskii[33]	$\cdots$	eqn. (3.41)	eqn. (3.42)
Jones [35]*et. al.*	$(1+3\beta/4)^{-1}$	$W/2.8$	$3W/(4\beta)$
Becker[7]	$(1+3\beta/4)^{-1}$	W	1

Table 3.1: Among all those models, Giordmaine and Wang model distinguish itself by neglecting the finite number density at the exit, so its angular dependence is away from other models.

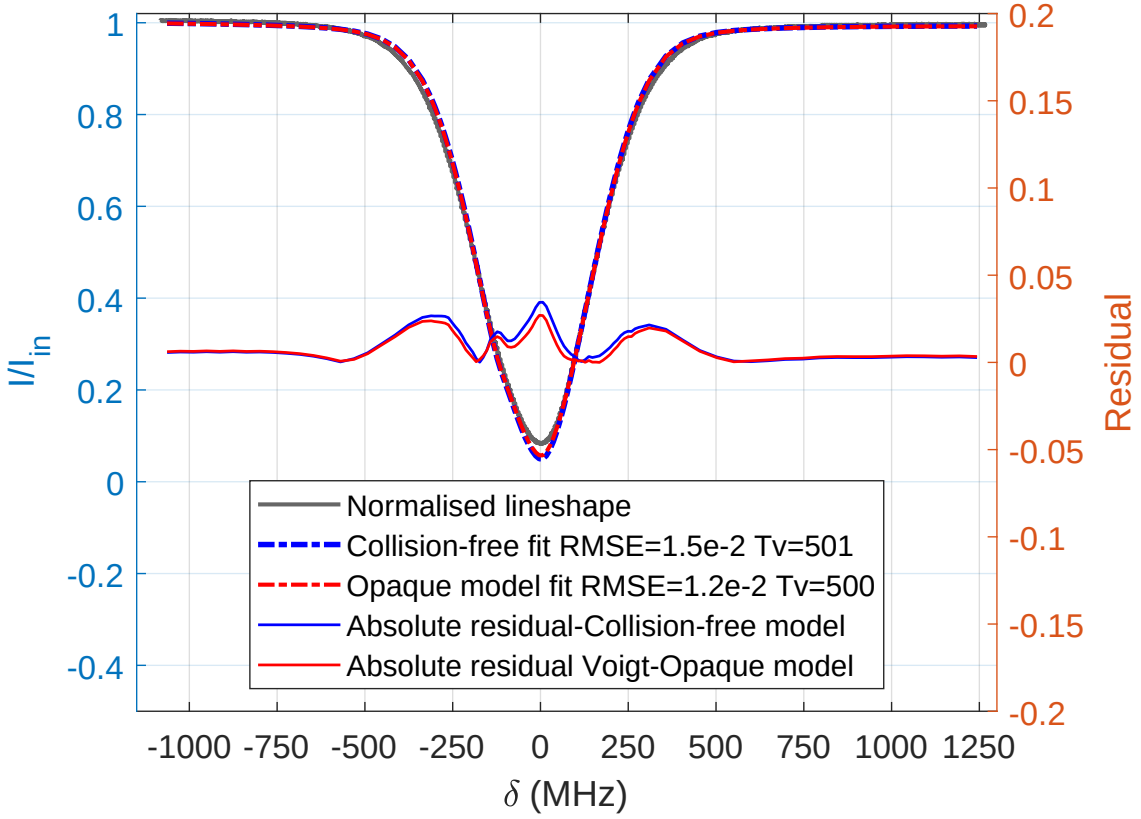


Figure 3.17: The opaque model (red dotted line) fit the lineshape better with smaller RMSE. The fitted vapour temperature using the opaque model (500 °C) is close to that from the collision-free model (blue dotted line, 501 °C).

3.3.1 Flux and peak intensity

By fitting the absorption lineshape, we get the vapour temperature T_v with an uncertainty ±7°C in the collision-free regime ($T_v \leq 474\,°C$). The fitting implies an

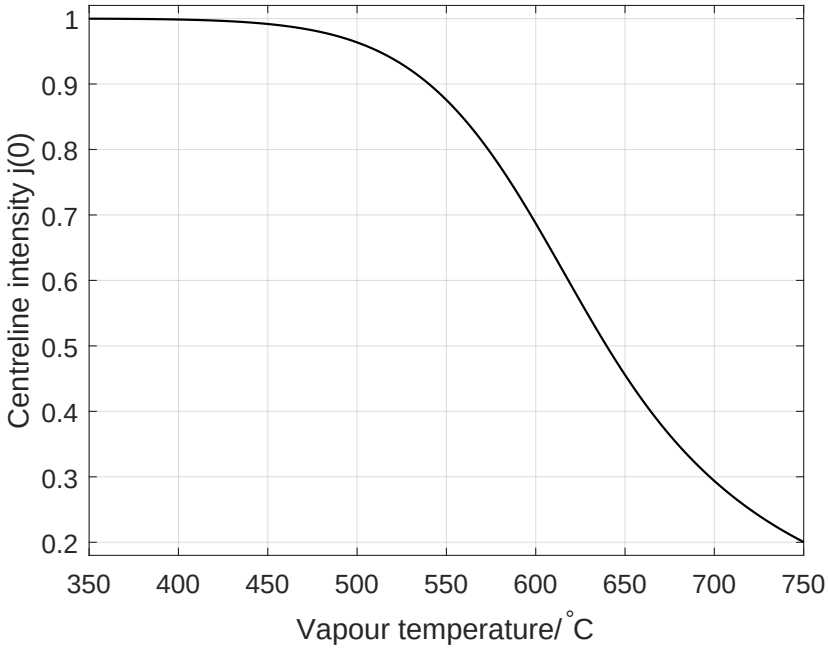
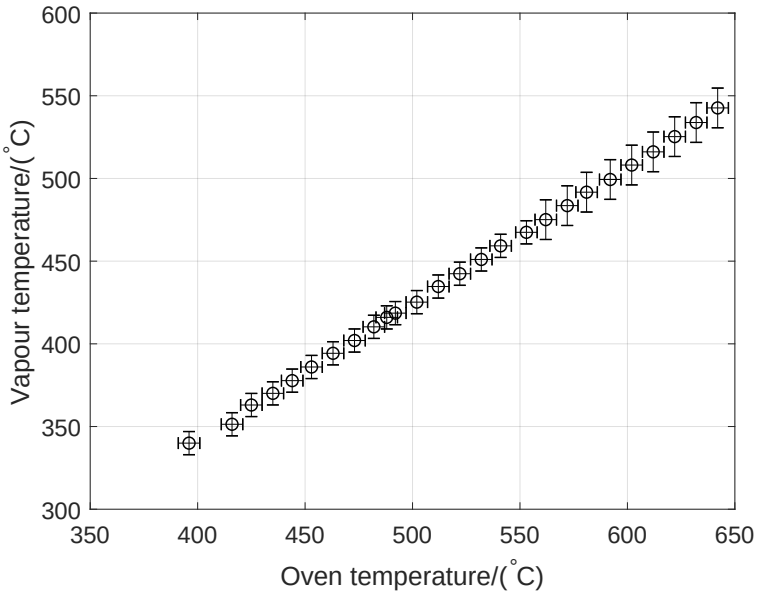


Figure 3.18: The centreline intensity $j(0)$ described by the Zugenmaier model drops with rising temperature, while $j(0)$ described by the collision-free model always equals one. So, to calculate the centerline intensity above 474 °C, the peak intensity $I(0)$ has to be modified as eqn. (3.36).

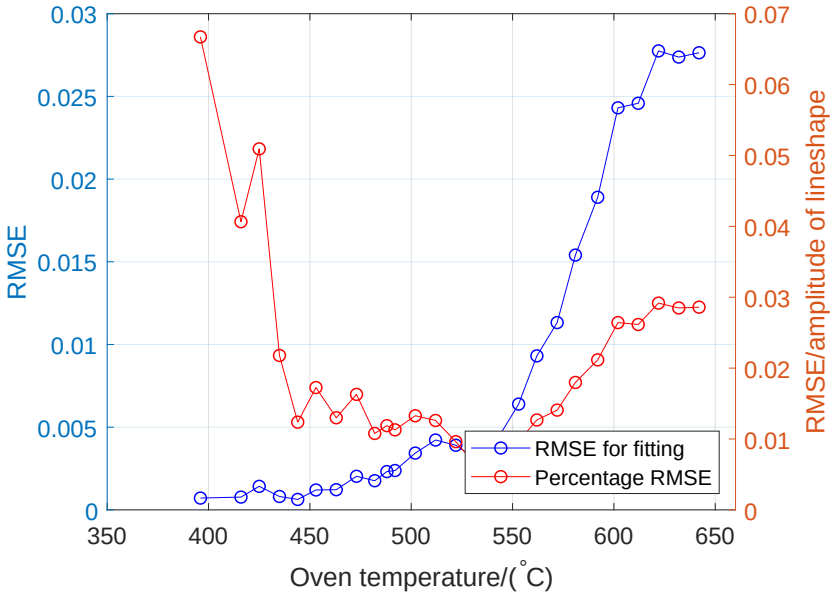
uncertainty of ±12°C in the opaque regime (474 °C $\leq T_v \leq$ 667 °C) but this should be treated with caution since we know that the model itself is not accurate. The fitted vapour temperature is shown in Fig 3.19a. Then we can work out the flux and peak intensity using eqn. 3.28, and results are shown in Fig 3.20a and Fig 3.20b.

3.4 Absorption of the laser light (MOT beams)

The 3D MOT has two strong laser beams that are 45° to the atomic beam's centerline, one of the MOT beam input is shown in Fig 3.21a. The laser beam with initial intensity of I_{in} travels through the vapour sample, and is then retro-reflected by a mirror. The intensity of the reflected beam, after traveling back through the sample, is measured by a photodiode; the ratio between this intensity I_δ and I_{in} corresponds to the optical density. The imbalance in intensities arising from absorption can affect the operation of the MOT. The measured absorption profile for the reflected cooling beam with frequency scanning is shown in Fig 3.21b , which has been converted onto the frequency domain.

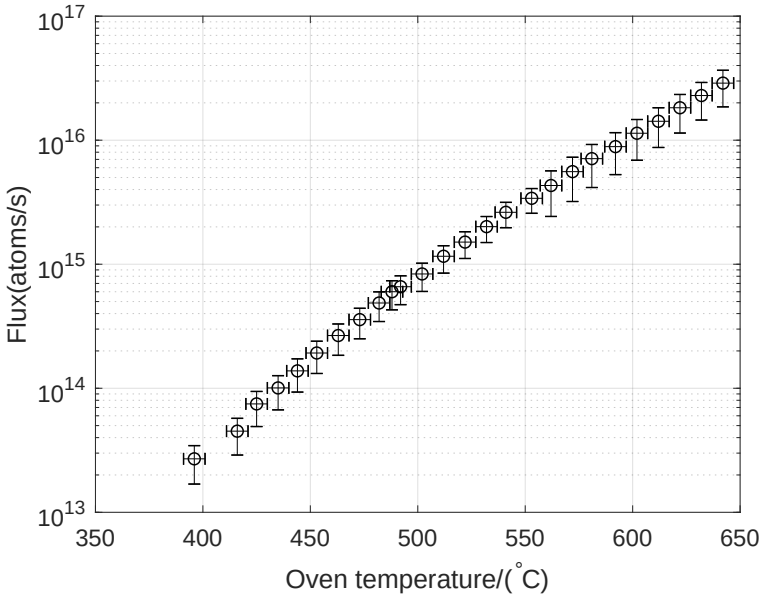


(a) Vapour temperature

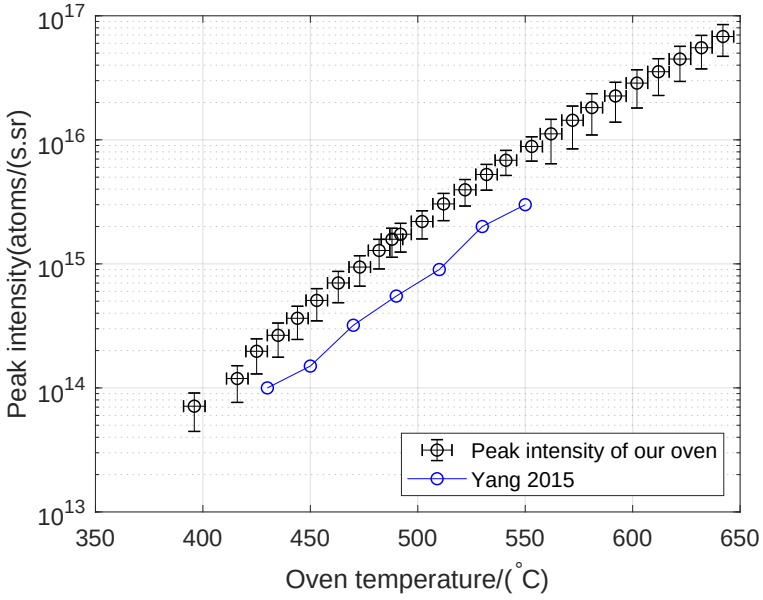


(b) RMSE

Figure 3.19: (a) The vapour temperature is roughly obtained from line-shape fitting, and is 70 °C lower than the oven temperature. (b) The RMSE of fitting (blue line) rises with temperature, especially beyond an oven temperature of $T_o \geq 560\,°\mathrm{C}$, where the vapour temperature $T_v \geq 443\,°\mathrm{C}$ approaches the theoretical threshold between collision-free and opaque modes (474 °C). The percentage RMSE (the RMSE divided by the signal amplitude) initially drops as the signal amplitude increases with temperature, but shows an increase with rising temperature beyond the collision-free regime.



(a) Flux



(b) Peak intensity

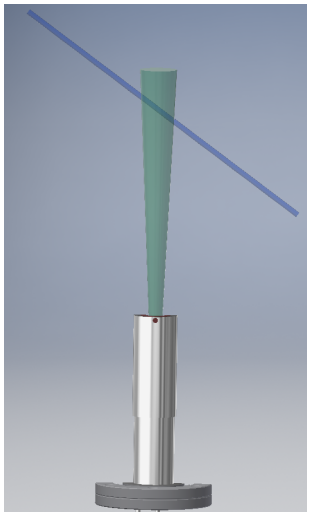
Figure 3.20: (a) The total flux rises exponentially with temperature and is above 10^{14} when the oven temperature is higher than 400 °C. (b) A comparison of our data with Yang *et al.*[80] shows that our oven gives a higher peak intensity at the same temperature.

3.5 Conclusion

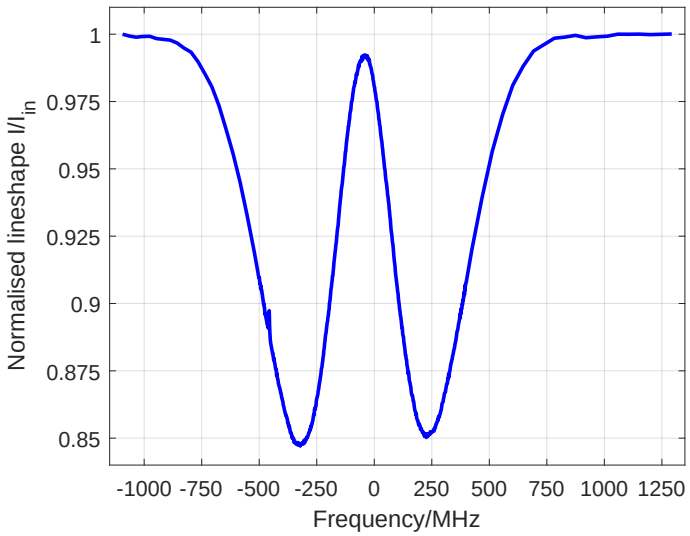
This chapter presented the derivation of a model for absorption spectroscopy of light through an atomic beam and showed that the lineshape derived from it performs better than the traditional Voigt fit, with fewer parameters required. We can extract the angular dependence $j(\theta)$ and vapour temperature T_v from the absorption lineshape, which yields the total flux and peak intensity. The peak intensity from our oven is higher than the previous state of the art[80, 5]. We tested our oven up to $T_o = 642\,^{\circ}\mathrm{C}$, for which the peak intensity and flux are $6.8 \times 10^{16}\,\mathrm{s}^{-1}\,\mathrm{sr}^{-1}$ and $2.9 \times 10^{16}\,\mathrm{s}^{-1}$. We commonly run the oven at $T_o = 502\,^{\circ}\mathrm{C}$ (explained in Chapter 5) and the corresponding peak intensity and flux are $2.2 \times 10^{15}\,\mathrm{s}^{-1}\,\mathrm{sr}^{-1}$ and $7.5 \times 10^{14}\,\mathrm{s}^{-1}$ respectively.

We also summarised various models for the atomic flux under the opaque mode. The collision-free model can be used to analyse the absorption lineshape in the opaque mode but with increasing uncertainty. The investigation of the RMSE shows that within the expected operating temperature range for our oven, the collision-free method is still acceptable for describing the absorption lineshape. It is predicted that the change of flow regime is associated with a change in the velocity distribution, i.e. that collisions in the atomic beam lead to a reduction in the number of slow atoms.

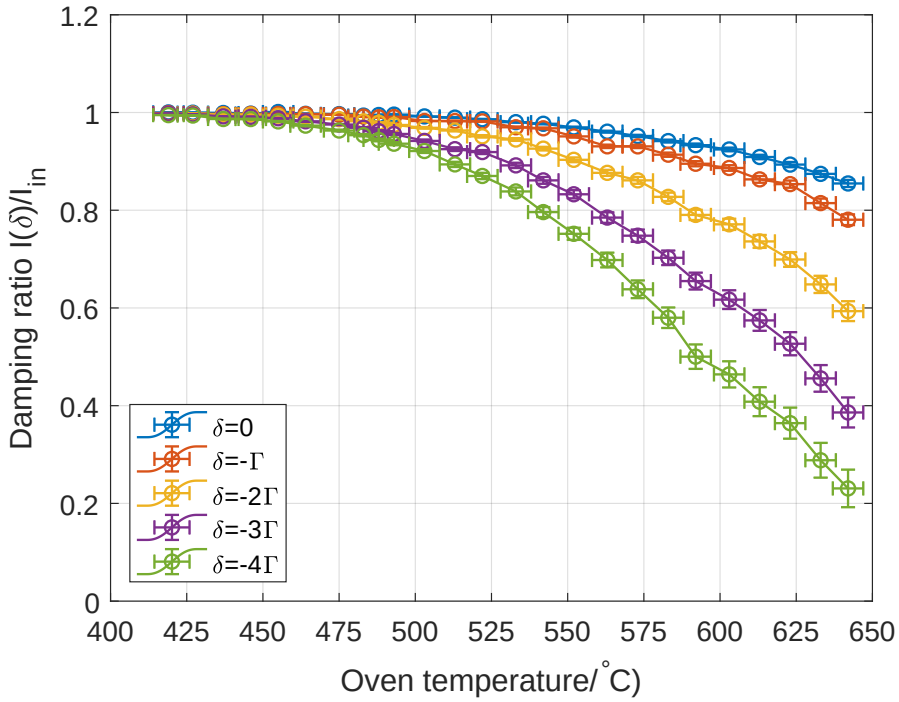
An investigation into the attenuation of the power of a laser beam passing through the atomic vapour showed that the reflected laser cooling beam became weaker with higher temperature or increasing frequency detuning to the red.



(a) 45° input beam.



(b) Normalised lineshape for reflected MOT beam.



(c) Attenuation of the beam power with oven temperature at various detunings.

Figure 3.21: (a) A laser beam (blue) travels at 45° through the atomic beam and the absorption signal is recorded by a photodiode. (b) The lineshape with the input beam intensity is normalised to unity. The lineshape shows symmetry in the frequency domain and the middle peak represents the resonance point. (c) The absorption becomes more severe when the oven's temperature is higher or the laser's frequency is further red-detuned. A 5% uncertainly of the absorption arises from the grid size used for sampling the signal.

Chapter 4

Apparatus: laser system

4.1 Mathematical description of laser radiation

Before giving the details of how the laser system was set up it is useful to outline the standard treatment of diffraction-limited propagation (Gaussian beams) and the polarization of radiation, in order to define relevant parameters.

4.1.1 Gaussian beams for laser cooling

The intensity profile of a Gaussian beam is given by

$$I(r,z) = I_0 \frac{w_0^2}{w^2(z)} \exp\left(\frac{-2r^2}{w^2(z)}\right), \tag{4.1}$$

where I_0 is peak intensity at the focus. The parameter $w(z)$ is the radial distance at which the intensity drops to $1/e^2$ of the intensity at $r = 0$ (r is the radial distance). The axial distance z is measured from the focus and the beam radius has its smallest value of $w_0 = w(0)$ at $z = 0$. This value is called the 'beam waist' or the spot size. The total power contained in the beam can be expressed as

$$P_0 = \frac{\pi}{2} I_0 w_0^2. \tag{4.2}$$

If the beam is apodized by an aperture with radius R, the power P transmitted is

$$P(r,z) = P_0 \left[1 - \exp\left(\frac{-2R^2}{w^2(z)}\right)\right]. \tag{4.3}$$

The intensity along the axis ($r = 0$) at a position z is

$$I(0,z) = \frac{2P_0}{\pi w^2(z)}. \tag{4.4}$$

The spot size parameter $w(z)$ is given by

$$w(z) = w_0\sqrt{1 + \left(\frac{z}{z_R}\right)^2}, \tag{4.5}$$

where z_R is the Rayleigh range given by

$$z_R = \frac{\pi w_0^2}{\lambda}. \tag{4.6}$$

Throughout this thesis, propagation in vacuum is assumed so wavelengths are calculated with a index of refraction $n = 1$. The on-axis intensity drops by half at $z = \pm z_R$, of the peak intensity, i.e. $I(0, z_R) = 0.5I(r = 0, z = 0)$. The '$1/e^2$ beam diameter' is also commonly used for selecting optics where $D = 2w(z)$ and instead of equation 4.3 the intensity and power P_0 are related by

$$I_0 = \frac{8P_0}{\pi D^2}. \tag{4.7}$$

The divergence of a Gaussian beam θ is given by

$$\theta = \lim_{z\to\infty} \arctan\left(\frac{w(z)}{z}\right) = \frac{\lambda}{\pi w_0}, \tag{4.8}$$

where the refractive index of medium is assumed to be $n = 1$.

4.1.2 Polarisation of light

The electric field of a classical plane electromagnetic wave, propagating along the z-axis, can be expressed as

$$\vec{E} = (A_H e^{i\varphi_H}\vec{e}_H + A_v e^{i\varphi_V}\vec{e}_V)e^{ikz-i\omega t} + c.c, \tag{4.9}$$

where $\vec{e}_H$ and $\vec{e}_V$ are horizontal and vertical unit vectors, A_H and A_V are real amplitudes, φ_H and φ_V are the phases of the vertical and horizontal components of the wave. The plane wave can be also expressed as

$$\vec{E} = A_H\vec{e}_H\cos(kz - \omega t + \varphi_H) + A_V\vec{e}_V\cos(kz - \omega t + \varphi_V). \tag{4.10}$$

Polarisation of the light can be classified as follows:

$$\text{Linear polarisation: } \varphi_H = \varphi_V \text{ or } \varphi_V \pm \pi, \tag{4.11}$$

$$\text{Circular polarisation: } \begin{cases} \varphi_H = \varphi_V \pm \pi/2, \\ A_H = A_V, \end{cases} \tag{4.12}$$

where all other cases are elliptical polarisation. There are two special cases for linear polarisation: horizontal polarisation ($A_V = 0$) and vertical polarisation ($A_H = 0$). The electric field vector in a linearly polarised wave oscillates along a straight line with an amplitude of $\sqrt{A_H^2 + A_v^2}$, while the electric field vector in a circularly polarised beam follows a circular pattern with radius $A_H = A_V$.

4.1.3 Polarising optics

Polarising beam splitters (PBS) are transparent cubes consisting of two triangular prisms stuck together. One component of light passes through and the other is is reflected at right angles. Wave plates are made from birefringent optical crystal (quartz) that introduces a phase delay $\Delta\varphi$ between the ordinary and extraordinary components of the electric field. We commonly use two types of wave plate: half-wave plates ($\lambda/2$-plate with $\Delta\varphi = \pi$) and quarter-wave plates ($\lambda/4$-plate with $\Delta\varphi = \pi/2$). For $\lambda/2$-plates

$$\alpha\,|H\rangle + \beta\,|V\rangle \longrightarrow \alpha\,|H\rangle + \beta\,|V\rangle\, e^{i\pi} = \alpha\,|H\rangle - \beta\,|V\rangle\,. \tag{4.13}$$

For the specific case of linearly polarised light (at angle θ to horizontal)

$$\cos\theta\,|H\rangle + \sin\theta\,|V\rangle \longrightarrow \cos\theta\,|H\rangle - \sin\theta\,|V\rangle = \cos\theta\,|H\rangle + \sin(\pi - \theta)\,|V\rangle\,. \tag{4.14}$$

For a quarter-wave plate, the general formula for the transformation is:

$$\alpha\,|H\rangle + \beta\,|V\rangle \longrightarrow \alpha\,|H\rangle + e^{i\pi/2}\beta\,|V\rangle = \alpha\,|H\rangle + i\beta\,|V\rangle\,. \tag{4.15}$$

The transformations for various specific cases using a quarter waver plate are shown below:

$$\begin{aligned}
&\frac{|H\rangle + |V\rangle}{\sqrt{2}}\ (+45^\circ \text{ linearly polarised}) \longrightarrow \frac{|H\rangle + i\,|V\rangle}{\sqrt{2}}\ (\text{right handed}),\\
&\frac{|H\rangle + |V\rangle}{\sqrt{2}}\ (-45^\circ \text{ linearly polarised}) \longrightarrow \frac{|H\rangle - i\,|V\rangle}{\sqrt{2}}\ (\text{left handed}),\\
&\frac{|H\rangle + i\,|V\rangle}{\sqrt{2}}\ (\text{right handed}) \longrightarrow \frac{|H\rangle - |V\rangle}{\sqrt{2}}\ (-45^\circ \text{ linearly polarised}),\\
&\frac{|H\rangle - i\,|V\rangle}{\sqrt{2}}\ (\text{left handed}) \longrightarrow \frac{|H\rangle + |V\rangle}{\sqrt{2}}\ (+45^\circ \text{ linearly polarised}).
\end{aligned} \tag{4.16}$$

4.2 Laser

4.2.1 Main laser table

The overview of the main laser table for laser cooling of strontium is shown in Fig 4.20. The beam splitting module enables the SolsTiS system to be switched to 780 nm for a separate Rb experiment, and to 922 nm for the Sr experiment. The following sections present details of each module.

4.2.2 SolsTiS Ti:sapphire laser

Our main laser source is a Ti:sapphire laser (SolsTiS from M Squared Lasers). This highly-tunable continuous-wave system covers the wavelength range from 670 nm to 1000 nm. To produce light at 461 nm, the Ti:Sapphire laser is running at 922 nm and outputs 3 W beam into an enhancement cavity (SolsTiS ECD-X), where second harmonic generation (SHG) gives 1.2 W at double the frequency.

The performance of the laser is extremely sensitive to temperature drifts of the Ti:sapphire crystal. A chiller is required to maintain the temperature of cooling fluid running through the crystal holder, but the chiller (NanoTherm) provided by the laser company did not function properly and this caused problems for coupling light into the frequency doubler and reduced the output power. The laser system was affected by the room temperature's drifts over seasons. Purchasing a new chiller (Coherent T253P) solved these problems.

The pump laser for the Ti:Sapphire system is a diode-pumped solid state (DPSS) laser at 532 nm, which provided a (maximum) power of 18 W (Coherent Verdi V18). This laser uses another (T253P) chiller set to 18 °C. The light from the Verdi pump laser goes through a periscope before coupled into the SolsTiS cavity through an input module (M Squared Lasers), which contains a pair of steering mirrors, a telescope and an iris blocking stray beams. Unlike the fully sealed design of SolsTiS cavity, the input module has a hole on the case and is vulnerable to dust in the air. We observed that cleaning optics in the input module regularly helped to maintain the output power from SolsTiS . Therefore we installed two laminar flow hoods (Swegon Air company MAC 10 IQ) above the optical table.

There are different models of SolsTiS available from M Squared Lasers: ours is the SolsTiS-PSX with an intracavity birefringent filter (BRF), an etalon and a piezo-driving actuator (resonator), with a linewidth of 10 MHz. The much more expensive model SolsTiS-SRX has an additional reference cavity. The BRF is used for coarse wavelength tuning according to the target wavelength input from the control user

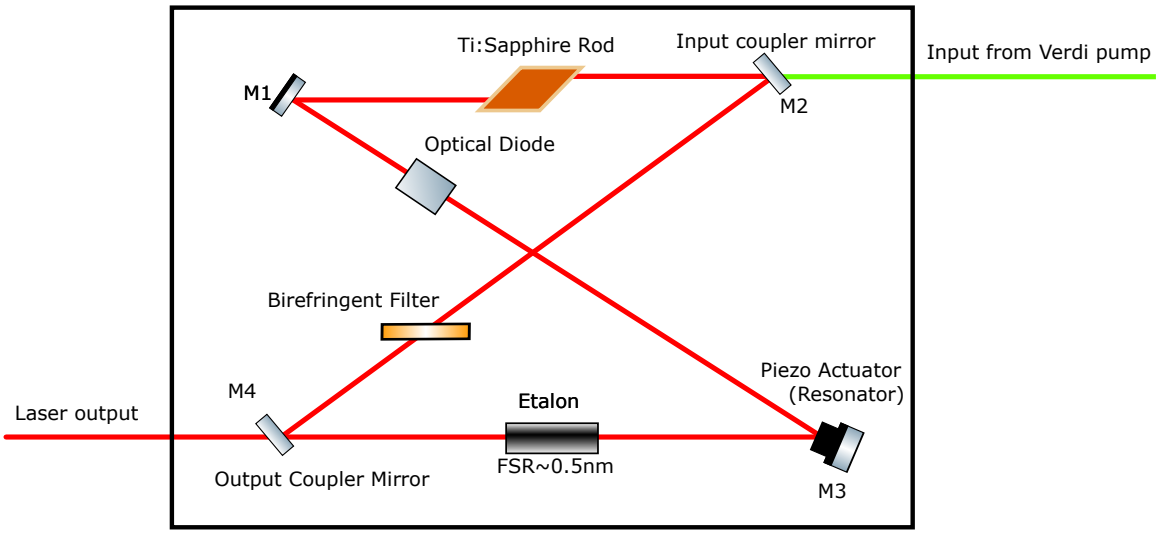


Figure 4.1: The SolsTiS laser has a bow-tie cavity containing a Ti:Saphhire rod, a birefringent filter (BRF), an etalon and a piezo-driving actuator (resonator).

interface in increments of 0.1 nm. Fine adjustments with the etalon can scan over one free spectral range (FSR). The interface allows manual tuning over more than one FSR, but the etalon could jump to the next etalon mode. Once the laser has been fine tuned to the target wavelength and the etalon has been locked to the nearest longitudinal mode of the laser cavity, the resonator lock is engaged, which adjusts the cavity length via the mirror mounted on piezoelectric material (PZT, lead zirconate titanate) to maximise the output power.

External input can be used to tune the PZT-mounted mirror, to stabilize the laser frequency with feedback signals from spectroscopy. The laser has a slow control input, which should be between ±10 V for tuning range of ±15 GHz and a fast control input, which should be between ±10 V for tuning range of ±40 MHz. With 18 W of pumping light, the SolsTiS laser can output 7 W at the peak of the gain curve, around 780 nm, but the output drops to 3 W at nm. Diode laser sources at the required frequencies for strontium are available but only provide hundreds of milliwatts of blue light.

4.2.3 Frequency doubling cavity

A frequency doubling cavity unit is used to generate more than 1 W of light at 461 nm light for laser cooling strontium from the SolsTiS laser as shown in Fig 4.2. The ECD-X module is a bow tie optical cavity of four mirrors built around a lithium triborate crystal (LBO, non-linear optical material). The SHG performance can decay over a period of months, requiring the user to adjust the mirrors and phase-matching to

re-achieve the maximum output power. Light at 922 nm can be absorbed by water vapour inside the high-finesse cavity, so a re-usable desiccant cartridge is installed on the system, which is recommended to be replaced every three months. The desiccant can be re-used after heating to 120C for three hours. The SHG module uses the Hänsch-Couillaud technique to generate the error signal for locking to the input fundamental frequency and a piezo-electric is used to scan and adjust the cavity length. If the total output power is lower than expected, it is necessary to tweak the cavity mirrors to boost the output but alignment should be done in the order specified in the manual (First adjust the pair M3 and M4, then adjust M1 and M4, then M2 and M3 in pairs). It is strongly forbidden by the guidance brochure to adjust M1 and M2 at the same time.

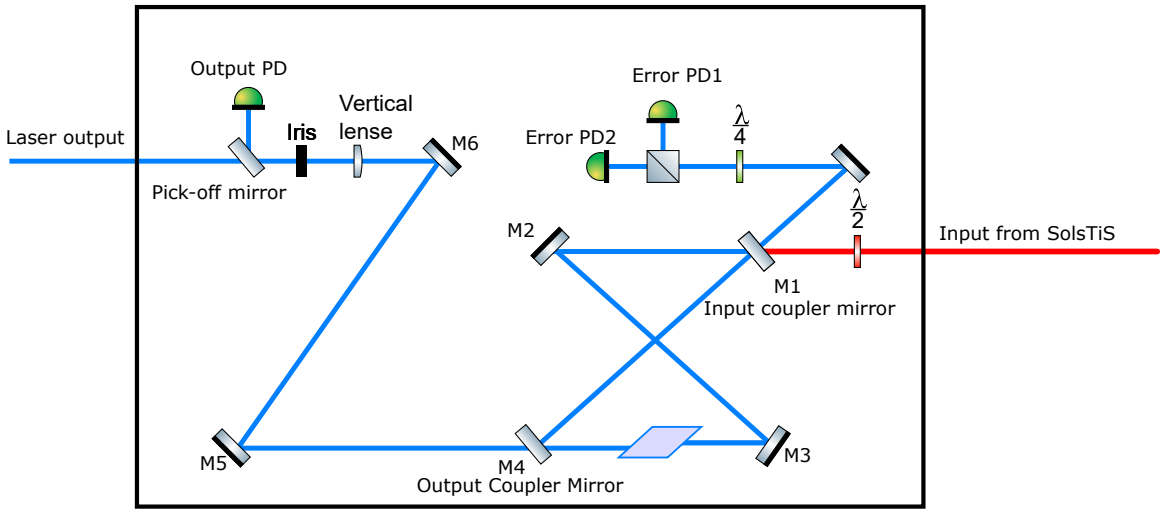


Figure 4.2: The frequency doubling unit has a bow-tie cavity, a LBO crystal and optics to generate an error signal. Those four cavity mirrors can be tweaked to maximise the total output power.

4.2.4 Beam distribution board

Blue light out of the ECD-X cavity is split into four parts, as shown in Fig 4.20: one part goes to the spectroscopy board for generating an error signal for locking; the other three are sent to the optics surrounding the experiment chamber to construct a magneto-optical trap (MOT). We used four collimators (60FC-4-M8-33) and three six-meter polarisation-maintaining single-mode FC/APC fibres (black fibres shown in Fig 4.20) from the company Schäfter and Kirchhoff (PMC-460Si-4.0-NA009-3-APC-600-P). These fibres have a damage threshold of 440 mW in the blue. The blue fibre shown in Fig 4.20 is a ten-meter polarisation-maintaining single-mode FC/APC fibre

from Thorlabs (P3-488PM-FC-10). Those collimators are focus-tunable, which allow users to manually tune the focus length of the collimator to optimise the coupling efficiency and reduce power loss caused by divergence from output of the ECD-X .

Since we did not have easy access to a beam profiler, we used the simple razor blade method to measure the output beam waist, by sliding a knife edge into the output beam and measuring the power of the unblocked part of the beam (with a power meter). For a Gaussian beam, the intensity $P(x)$ measured with blade at position x obeys the equation [24]

$$P(x) = P_0 \left[1 - \mathrm{erf} \frac{\sqrt{2}(x - x_0)}{\omega(z)} \right]. \tag{4.17}$$

We can fit the data points as shown in Fig 4.3.

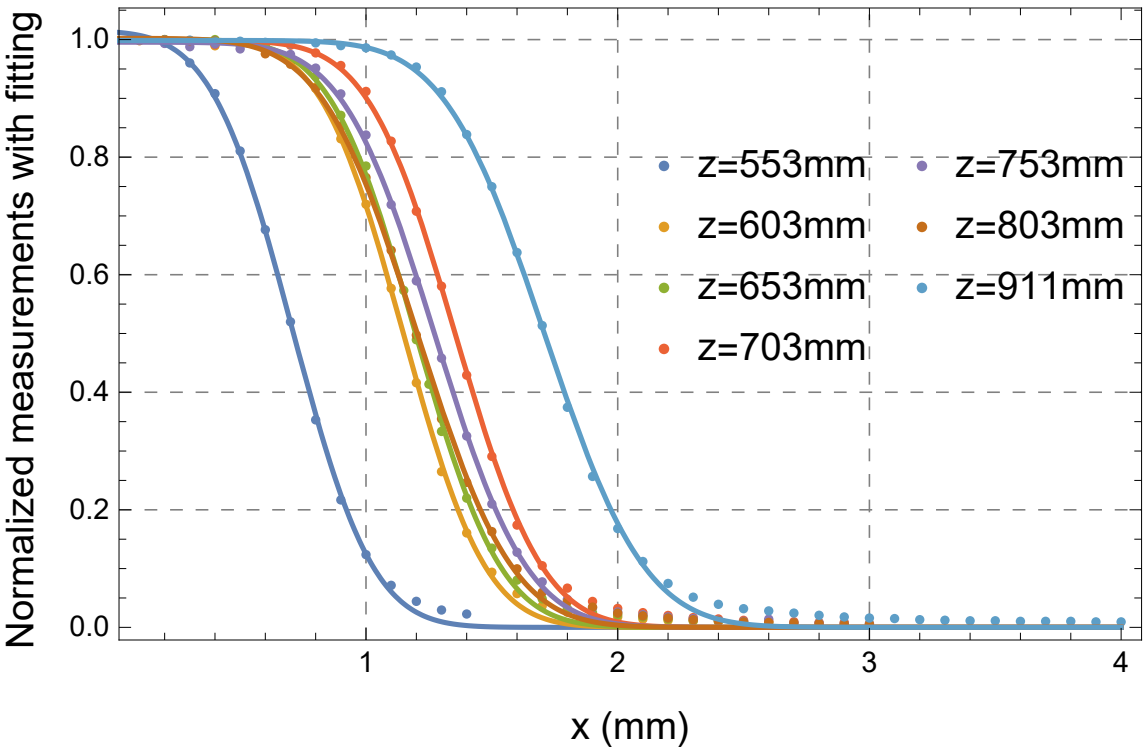


Figure 4.3: Beam intensity measurements at different position x, which is the distance the blade moves transversely to the beam.

The waist $w(z)$ was measured at various positions z along the beam, and eqn. (4.5) was used to fit beam waist as shown in Fig 4.4. The beam divergence was found to be 4.5×10^{-4} rad. We did not try to reshape this beam with telescopes, but laid all collimators roughly at same distance away from the output port of the SHG cavity, and used the focus-tunable collimators to get good fibre coupling efficiency.

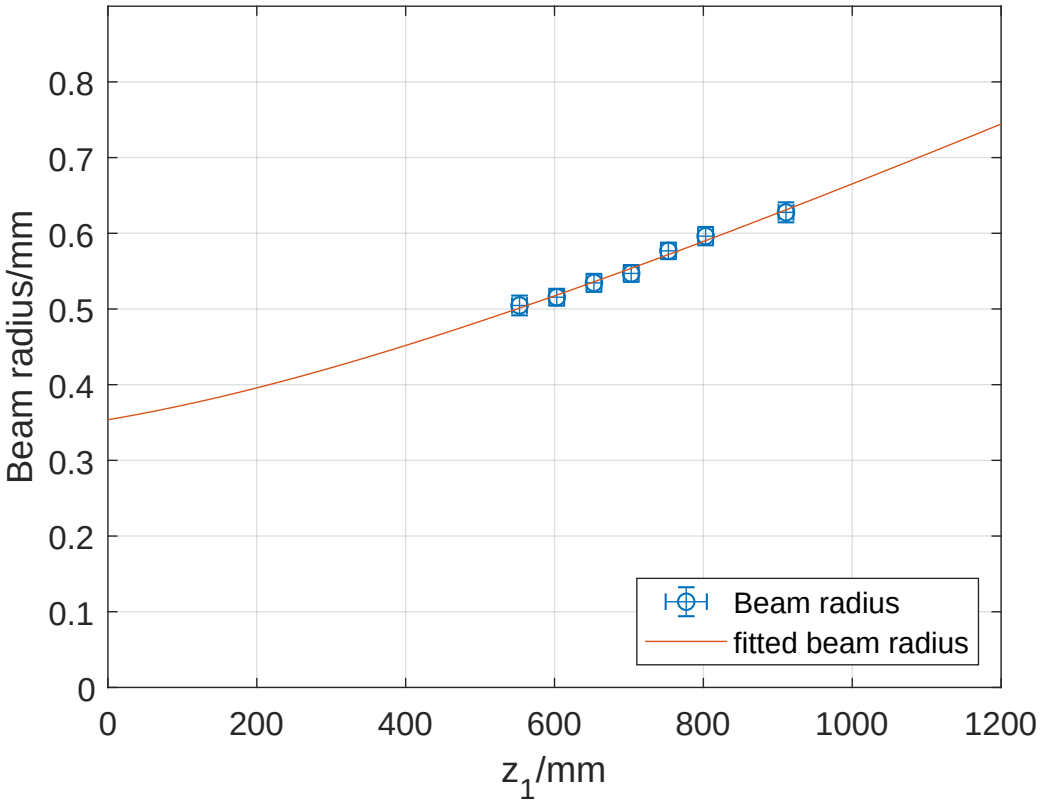


Figure 4.4: The figure presents the measured beam radius at different positions z_e, which is the distance between the razor blade and the output port of the ECD-X . The beam waist is 0.33 mm and the beam divergence of output beam is 4.5×10^{-4} rad.

4.2.5 Secondary distribution board

As shown in the Fig 4.21, the second distribution board split the input from main board into two parts: one for the spectrometer and one for the acousto-optical modulators (AOMs). The wavemeter (MOGLabs, MWM), is customised and tested for wavelengths between 433 nm and 471 nm with resolution 100 MHz (the calibration uncertainty is much greater). This wavemeter is used to tune the SolsTiS and ECD-X close to the atomic resonance and then we lock the laser frequency with our spectroscopy. The power into the wavemeter should be between 1 pW and 1 mW, so there is a neutral density filter in front of the collimator (1% transmission).

The AOM shifts the frequency by roughly 80 MHz (towards the higher frequency) and is used for stabilising the power of the probe beam by actively adjusting the amplitude of the sin-wave signal driving the AOM. Although all the optical fibres are specified as single-mode and polarisation-maintaining, the output may not be

perfectly linearly polarised because of cross-coupling between the two polarisation modes during propagation. Therefore a linear polariser was inserted after the optical fibre to purify the polarisation of the output beam. Then, a half-wave plate and a PBS are used to take a portion of the power onto a photodiode, whose output is compared with a defined setting point. If the photodiode reading drifts away from the setting point, the PID controller (Toptica Photonics, PID 110 controller) will generate a feedback output, which tunes the amplitude of a externally-tunable signal source (oscillator) driving the AOM and correspondingly adjusts the power of the light on the photodiode back to the setting point. This feedback loop almost eliminates power drifts in the output beam from the fibre, in both the short term and long term, and this power-stabilised, polarisation-purified beam gives low noise for usages in the spectroscopy.

4.2.6 Spectroscopy board

We use modulation transfer spectroscopy (MTS) to generate an error signal for laser frequency locking. We also apply a tunable magnetic field over the atomic beam that tunes the locking point by the Zeeman effect, as explained in Sec 4.3.6. We call this tunable MTS spectroscopy (TMTS). A similar scheme was reported for rubidium in October 2019 [67] but we had set up our TMTS independently in March 2019.

4.2.7 Test module for polarisation

As circularly polarised beams are required for a MOT and for the spectroscopy, it is important to have a method to test the handedness of circularly polarised light. The process for constructing a module to test polarisation handedness is shown in Fig 4.5. The first step is to send a beam through half-wave plate and PBS to get a horizontally polarised beam. This horizontally polarised light is then sent through a linear polariser mounted on a rotational cage mount (Thorlabs, CRM1/M), which is rotated to minimise the photodiode reading. The linear polariser now only transmits vertically polarised light. In the second step, we insert a quarter-wave plate mounted on a rotational cage mount (Thorlabs, CRM1/M). The transformations in eqs. (4.16) show that only when the optical axis of the quarter-wave plate is at $\pm 45^\circ$ to the horizontal direction, will the photodiode have the maximised reading. The final step is to secure the angle of the linear polariser and the quarter-wave plate, and construct a four-rod cage to hold them together. This test module is the handedness reference for all the circularly polarised beams.

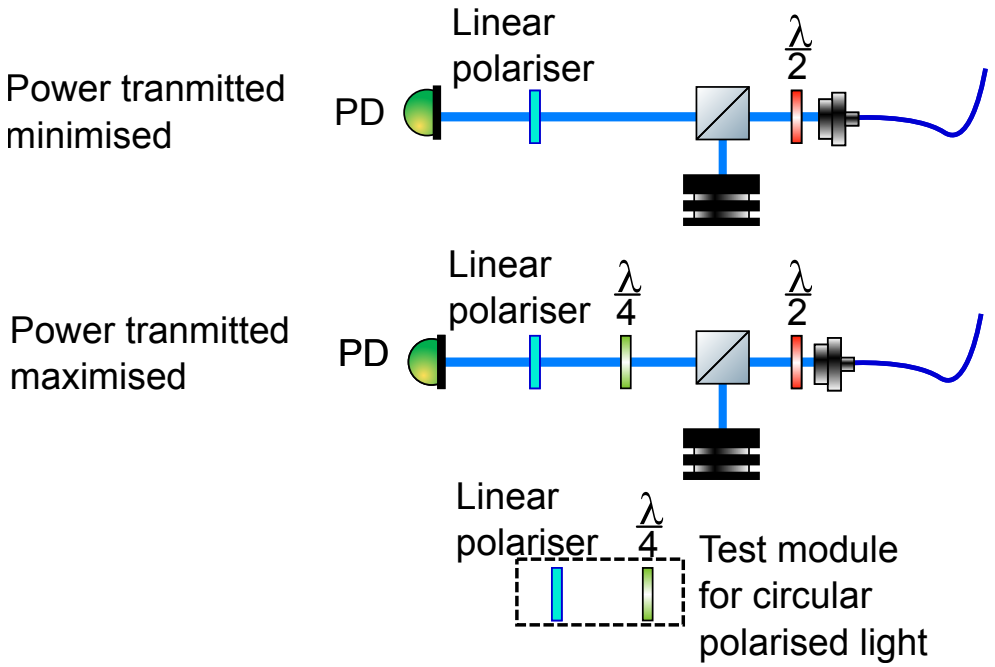


Figure 4.5: This figure presents the first three steps required for constructing the module for testing the handedness of polarised light.

An example of using the test module to determine the handedness of a circularly polarised MOT beam is illustrated in Fig 4.6. Right-handed circular polarised light is converted to vertical polarised light and left-handed circularly light to horizontally polarised light, after going through the quarter-wave plate of the test module, based on eqs. (4.16). Rotating the quarter-wave plate in front of the MOT beam fibre to reach a minimum or maximum reading for the photodiode ensures that the MOT beams are left-handed or right-handed as required. In practice, it is hard to work out the required polarisation relative to the direction of the magnetic field (current flow in the coils), but if the MOT beams are correct relatively to each other, there remains a binary choice for the current (which can be changed by swapping over the current leads).

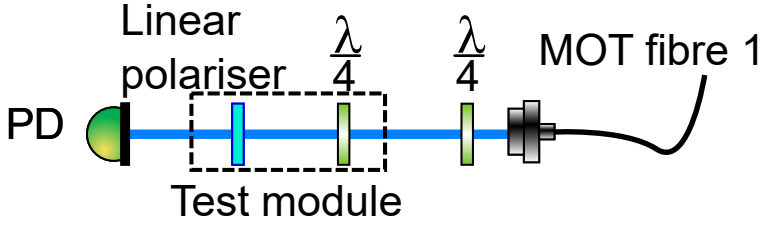


Figure 4.6: The output from MOT fibre 1 is sent through one quarter-wave plate (rotational and cage mounted), then through the test module, and finally onto a photodiode.

4.3 Laser spectroscopy for frequency stabilisation

Stabilising the laser frequency using an error signal generated from the spectroscopy of a certain atomic transition is a very important method for modern laser technology. The strong transition used for laser cooling of strontium has a large natural linewidth (32 MHz). Therefore a locking precision within a few MHz is sufficient. Multiple methods for locking are listed in this section with comments on their feasibility of generating a reliable error signal for laser frequency stabilisation.

4.3.1 Absorption spectroscopy

The simplest approach is to send a laser beam through the strontium gas sample (transverse direction) and measure the transmission. The frequency width of the absorption dip depends on the Doppler broadening from the velocity distribution of the atoms. The line width is around over 1 GHz, which does not function as a precise locking point. This absorption profile has been presented in chapter 3. The laser beam should not have much more than the saturation intensity, otherwise the absorption is weaker than optimum.

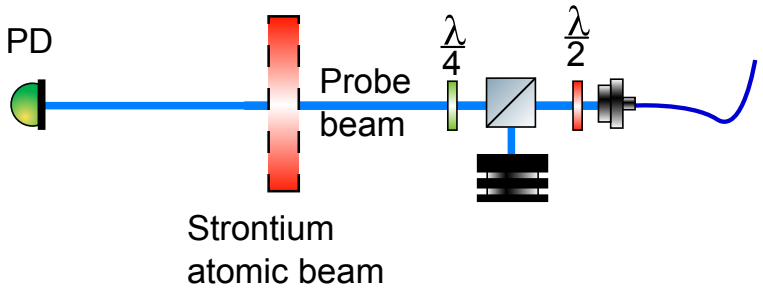


Figure 4.7: A half-wave plate and PBS are used to purify the polarisation and tune the power of the probe beam.

4.3.2 Doppler-free absorption spectroscopy

Saturated absorption spectroscopy is a Doppler-free technique that uses two laser beams: a 'probe' beam and a counter-propagating 'pump' beam. The pump beam is stronger, and may be wider, and it drives atoms into the excited state. Due to the Doppler effect, atoms moving towards the laser beam will observe a blue-shifted laser frequency, while atoms moving in the same direction as the light will observe a red shift. Atoms see opposite Doppler shifts in the pump and probe beam. So, only static atoms can interact with both laser beams, and the saturation caused by the

pump beam decreases the absorption of the photons in the probe, which contributes to a small narrow peak at the minimum point of the absorption lineshape. It can be used for frequency stabilisation with further processing. A traditional Doppler-free absorption spectroscopy layout is shown in Fig 4.8. The quarter-wave plates ensure that the probe beam and pump beam are circularly polarised. We used the cage-mounted optics around the MOT chamber to construct a simple set up for the Doppler-free absorption spectroscopy. The observed lineshape is shown in Fig 4.10, which can generate a dispersion-shaped error signal with phase-sensitive detection.

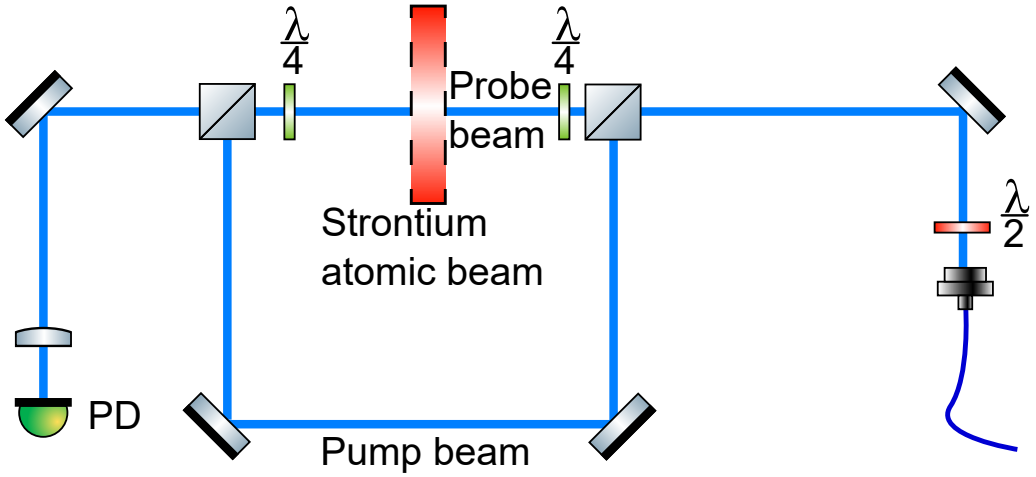


Figure 4.8: The half-wave plate and PBS are used to purify the polarisation and tune the power into the probe and pump branches. The probe beam is weaker compared with the pump, and the probe beam should be less than the saturation intensity to avoid power-broadening.

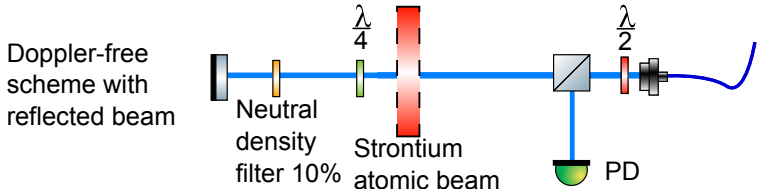


Figure 4.9: The half waveplate and PBS are used to purify the polarisation and tune the power. The horizontally linearly polarised input beam functions as a pump beam and the reflect beam functions as a probe beam. The neutral density filter will attenuate reflected beam, which functions as a probe. The quarter waveplate will convert the reflected beam into a vertically linearly polarised beam, which can then be focused on the photodiode.

Saturated absorption spectroscopy provides a precise reference frequency at the atomic resonance. But in our experiments, we require tuning the laser frequency

over a several times the natural linewidth, e.g. 120 MHz). This requires at least two (expensive) AOMs used in the double-pass arrangement, which takes efforts to align. With a direct digital synthesis (DDS) function generator card providing the driving frequency, the double-pass arrangement can become a highly controllable locking system for automating experiments. To avoid using many AOMs, we only use the Doppler-free absorption spectroscopy to calibrate other locking schemes.

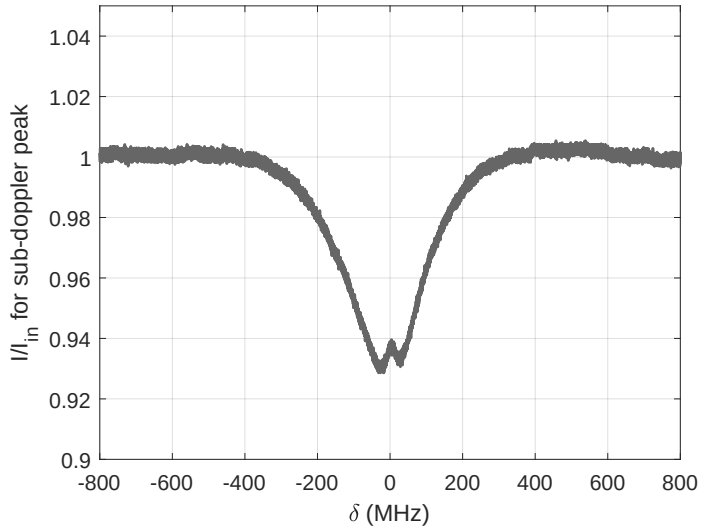


Figure 4.10: The normalised saturated absorption profile was taken at oven temperature 397 °C. The dominant peak is that of ^{88}Sr, which can used as an absolute frequency reference to calibrate other spectroscopy methods.

4.3.3 Polarisation spectroscopy

Polarisation spectroscopy is a widely-used modulation-free method for frequency stabilisation. A circularly-polarised pump beam builds up a bifringence in the sample that affects the polarisation of the linearly polarised probe beam[34]. This can be described as the pump beam creating a difference in the absorption coefficient for the left-hand and right-hand circularly polarised components in the probe beam. The circularly polarised pump beam saturates either the $\sigma+$ or $\sigma-$ transition which reduces the absorption of the component in the probe beam with corresponding handedness. The difference is read out by a differential photodiode, which provides common-mode rejection of noise (as compared to taking difference between two photodiode readings). For the odd isotopes of strontium which have nuclear spin and hyperfine structures, optical pumping can affect the signal. A simple layout of optics for polarisation spectroscopy is shown in the Fig 4.11.

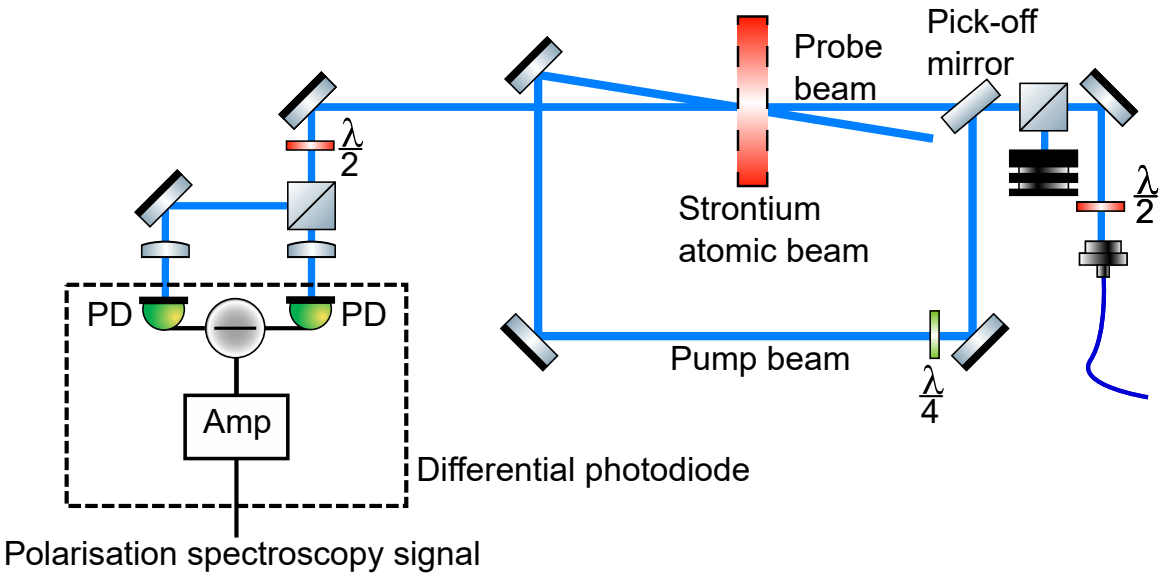


Figure 4.11: The optical layout for the polarisation spectroscopy is simple. The differential photodiode is used for reading out the error signal.

An advantage of the polarisation spectroscopy is that it requires simple optics and electronics to generate a dispersive error signal, without modulating the laser frequency or applied magnetic field. A disadvantage for our applications is the narrow range of frequency tuning of around 80 MHz, which is smaller than we require.

4.3.4 DAVLL scheme

We also explored the so-called Dichroic Atomic Vapour Laser Locking (DAVLL) spectroscopy. This method takes advantages of the splitting sub-levels caused by Zeeman effect under static magnetic field parallel to the atomic beam[75]. Linearly polarized light consists of two circularly polarised components. Each of them drives one of the σ components and contributes to an absorption lineshape. If there is no magnetic field, the two lineshapes are overlapped with each other. The normal Zeeman effect shifts the $\sigma+$ component by

$$\delta_{\sigma+} = \frac{g\mu_B}{h} \tag{4.18}$$

in units of Hz, and $\delta_{\sigma-} = -\delta_{\sigma+}$. The Zeeman shift for a B-field of 1 G is 1.4 MHz. With magnetic field applied, the circularly polarised components, $\sigma+$ and $\sigma-$, are spaced by $2\delta_{\sigma+}$. These two circularly polarised components are converted into horizontally and vertically linearly polarised light respectively first after passing through a quarter-wave plate, and then separated by a PBS cube and detected by a differential photodiode. The differential signal is a dispersive signal with a linear slope

(31.5 MHz with 15 G field[22]) around the resonance[34]. The diagram of DAVLL spectroscopy is shown in Fig 4.12. By applying one pumping beam(Fig 4.13), we can get sub-Doppler DAVLL lineshapes, which covers narrower range of frequency[34]. The output of differential photodiode should be zeroed out by tuning the quarter waveplate when there is no field applied.

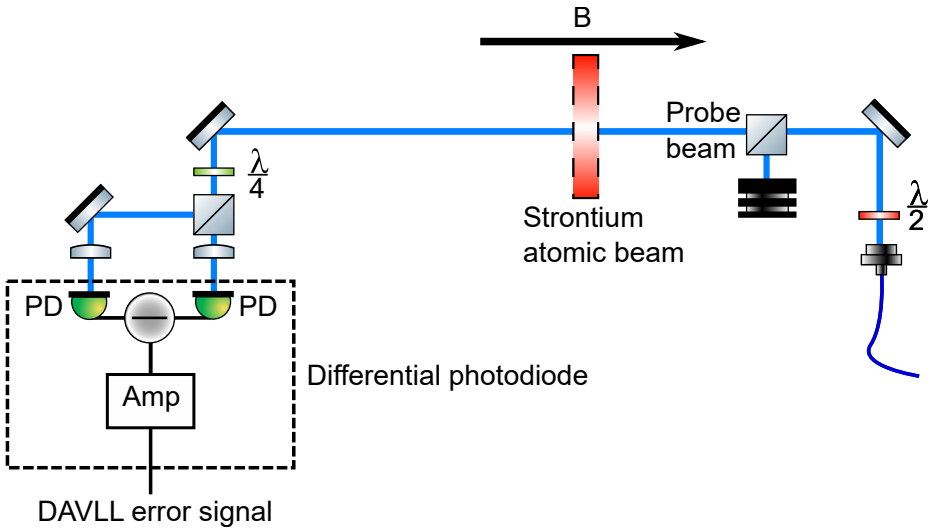


Figure 4.12: A magnetic field is applied over the gas sample to split the Zeeman sub-levels, which are probed by two circularly polarised components in the linearly polarised probe beam. The quarter-wave plate and PBS convert the circularly polarised components into vertically and horizontally linearly polarised light and separate them onto the differential photodiode. The differential signal read out from the differential photodiode is a dispersive signal.

The advantage of the DAVLL scheme is that it gives a linear slope over a large frequency range. By adjusting the locking point along the linear slope, the stabilised frequency can be tuned over 100 MHz. The sub-Doppler DAVLL scheme has a sharper slope around the resonance, while has a smaller frequency tuning range[34]. The disadvantages of DAVLL and sub-Doppler DAVLL schemes are that they are both rely heavily on the homogeneity and stability of magnetic field. Also, stray fields affect the lineshape. To achieve a wide tuning range, DAVLL scheme requires a strong magnetic field (above 45 G). We tried permanent magnets held in place by a 3D-printed plastic box as shown in Fig 4.15; this holds a single neodymium disk magnets (25 mm by 10 mm) above the spectroscopy chamber. Due to limited space around the spectroscopy chamber, we could not form a more balanced layout for magnets. The results we obtained with DAVLL are shown in Fig 4.14 (calibrated with Doppler-free spectroscopy). Unfortunately this set was not successful enough for a

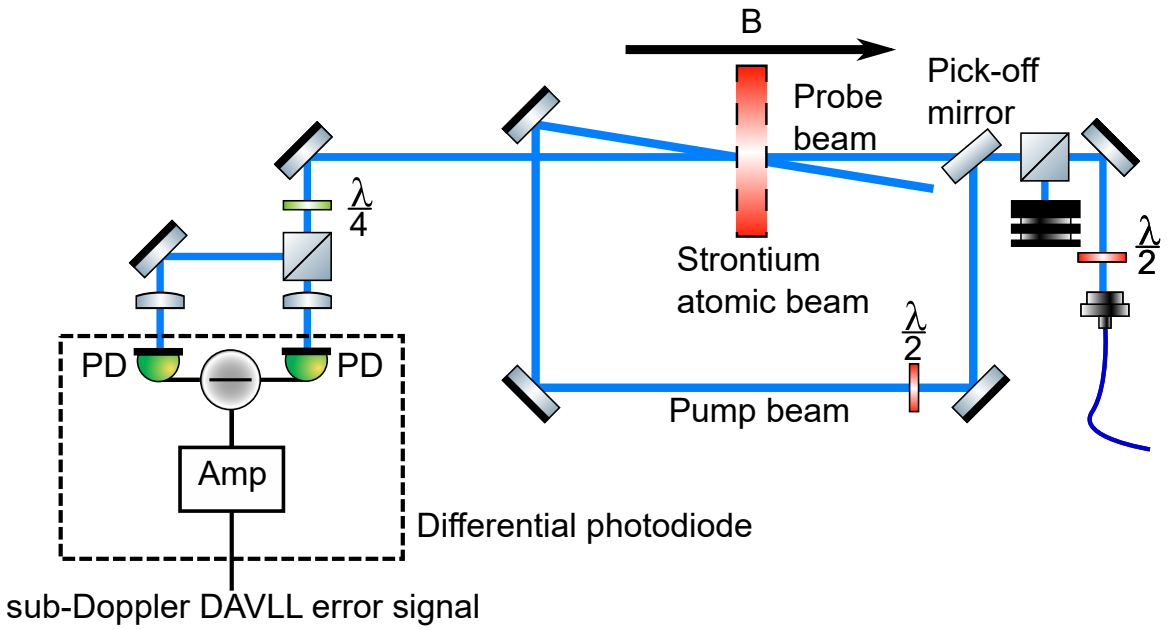


Figure 4.13: A linearly polarised pump beam is used to get the sub-Doppler feature. The half-wave plate is used to transform the pump beam into horizontal linearly polarised light.

proper locking because of vacuum problems. The strontium was kept under mineral oil when delivered (Sigma-Aldrich, 403326-5G) and despite cleaning it thoroughly with solvents (hexane), we observed residuals baked out from strontium granules. Residual components from mineral oil were vaporised after heating and built up inside the chamber, which messed up the spectrum over time. So, we had to clear the apparatus and refill the oven with high-purity strontium delivered in a sealed glass tube(Sigma-Aldrich, 460346-5G).

4.3.5 Frequency modulation spectroscopy

Frequency modulation(FM) spectroscopy is a widely used scheme for stabilising frequency[52] and theory for it can be found in Ref [10]. The layout of optics is shown in Fig 4.16 and the generated signal has a dispersion shape with a steep slope across the resonance. A disadvantage is that the laser source is modulated with a high-frequency input signal, which can affect other parts of the experiment sharing the same laser. Also, the tuning range is limited, so we could not use it for our experiment.

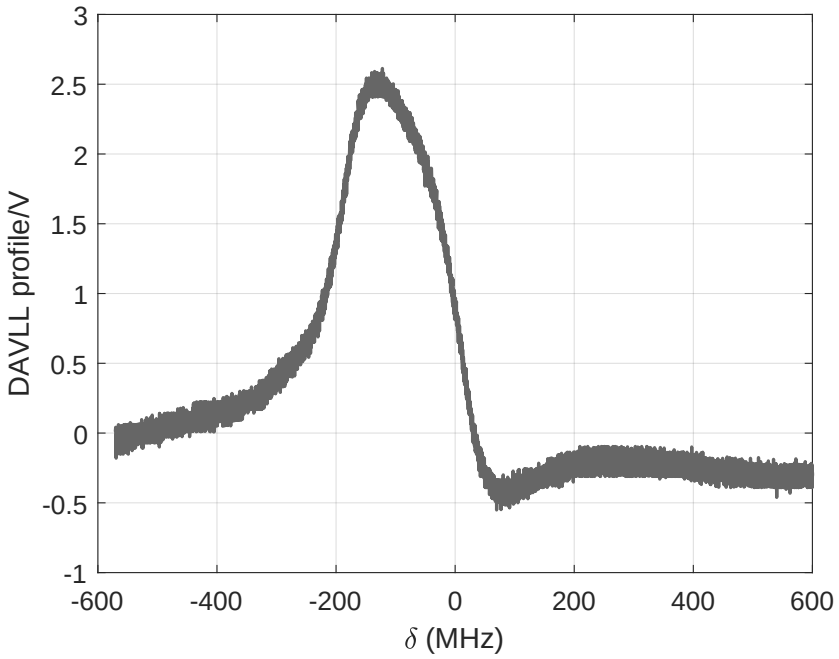
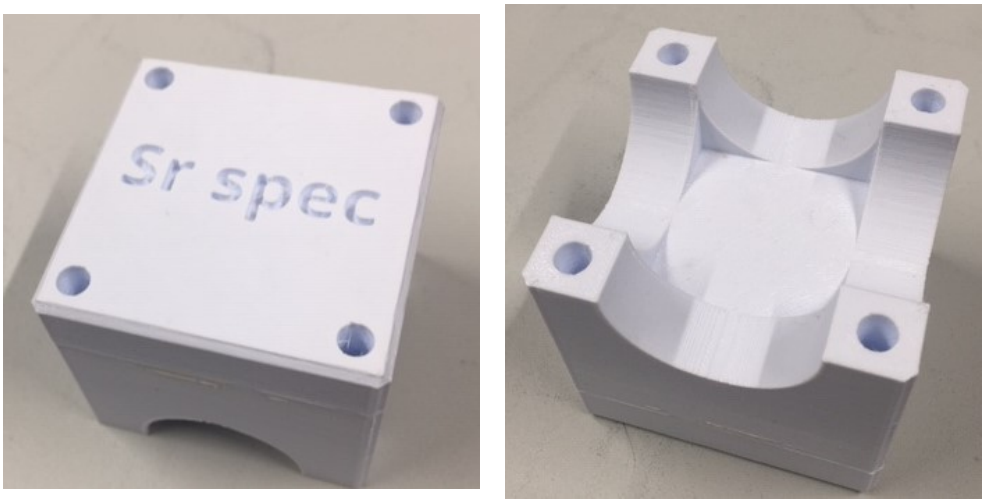


Figure 4.14: The DAVLL lineshape has a linear slope across the resonance and can be used to tune the locking point by changing the voltage set point.



(a) Top view of the magnet holder.

(b) Back view of the magnet holder.

Figure 4.15: This 3D printed case (designed by project student Peter Zhou) was used to hold the permanent magnet, which fits around a CF-40 cross and can be bolted down on the optical table.

4.3.6 Modulation Transfer spectroscopy

The basic theory for modulation transfer spectroscopy (MTS) can be found in Ref. [47]. The pump beam is frequency modulated at 10 MHz by an EOM driven by a signal

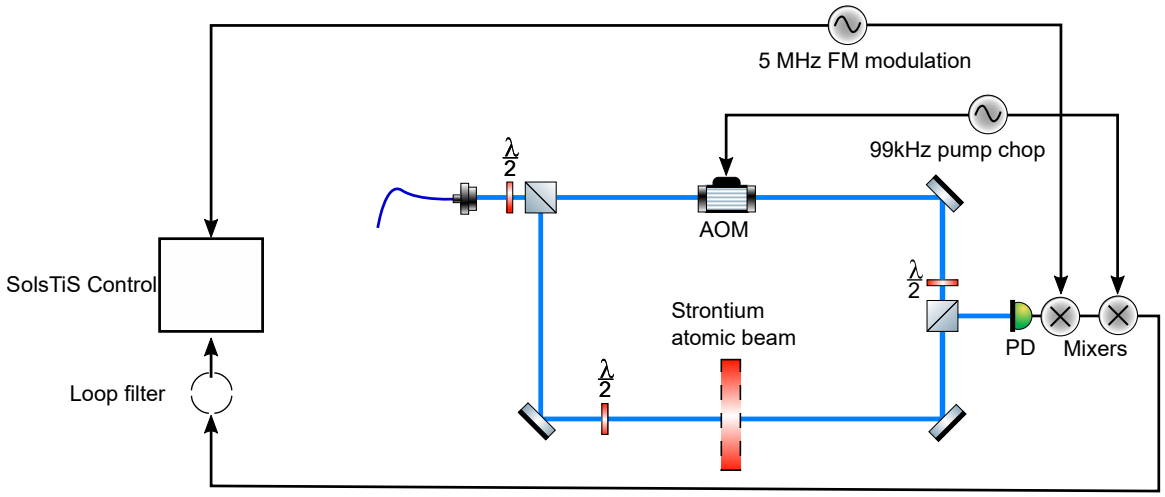


Figure 4.16: The set up for the FM spectroscopy has an AOM for modulation of the frequency of the laser.

generator (Stanford Instruments). Another signal generator (of the same type) working at the same frequency is synchronised with the first source, but with an adjustable phase difference. We need to extract the 10 MHz component out from the photodiode's output signal. The amplitude of the 10 MHz component is −61 dBV, which is fairly small. A gain-switchable photodiode can solve the problem. But we only have fixed-gain photodiode in the lab, so we replace the 887 Ω gain resistor(92A) and the 20 pF integrator capacitor in the Thorlabs PDA10A-EC photodiode with a 20 kΩ resistor and a 1.2 pF capacitor, to boost up the gain without sacrificing too much of the bandwidth. The amplified signal is then mixed with a reference signal from the second source to extract the MTS error signal. The optics layout is presented in Fig 4.21 (without field) and a typical lineshape is shown in Fig 4.17, together with a saturated absorption profile for calibration.

MTS does not modulate the source laser directly, so it would not affect other branches sharing the same laser source. However the stabilised frequency can be only tuned within a very limited range, which leads to our final spectroscopy solution - tunable MTS.

4.3.7 Tunable MTS

We installed a pair of Helmholtz coils around the spectroscopy chamber as shown in Fig 4.21. The static magnetic field can shift the MTS lineshape. The quarter-wave plates shown in the figure are aligned so that only one of the σ components is measured. We can shift the error signal in the frequency domain by tuning the

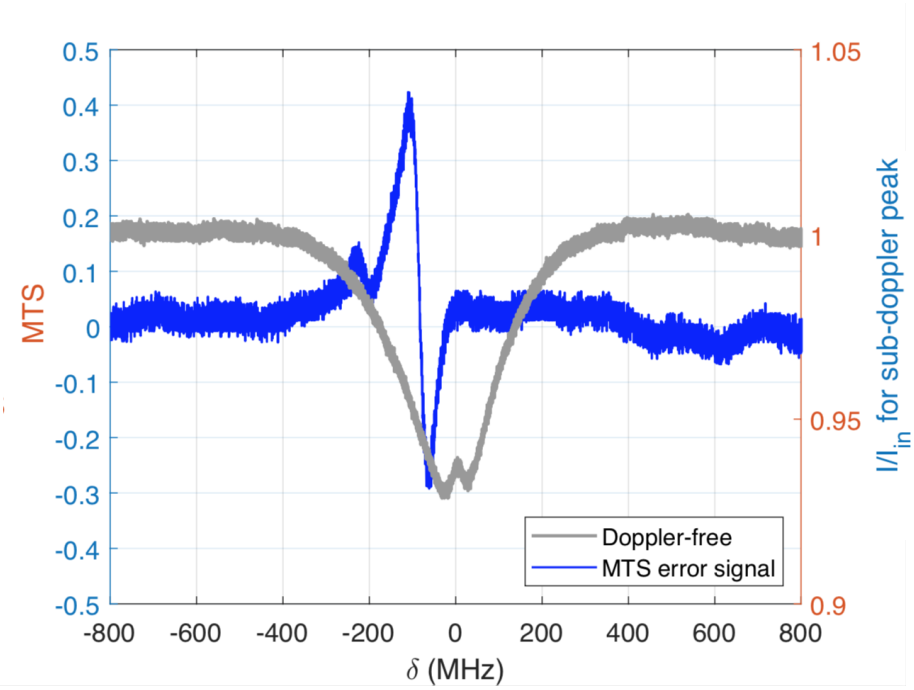


Figure 4.17: The MTS error signal has a steep linear slope around resonance. It is calibrated with respect to the saturation absorption spectroscopy. There is around 80 MHz offset between the two signals, as the input beam for MTS has been tuned by an AOM before entering the spectroscopy chamber.

current sent into the coils. The laser frequency is locked to the zero point of the linear slope on the MTS error signal, and this zero point can be tuned directly by changing the current[1]. We calibrated the frequency of the MTS' locking point under various currents with respect to saturated absorption spectroscopy. The relationship between the locked frequency detuning, δ, and the applied current is shown in Fig 4.18. The precision of locking is within ± 3.5 MHz.

4.3.8 locking electronics

The MTS signal has a dispersive shape and we want to engage frequency locking at the zero-crossing point. As previously mentioned (Sec 4.2.2), the laser has two external inputs for tuning its frequency: slow coarse tuning and fast fine tuning. To generate the control signals for these slow and fast inputs, the error signal is integrated by two operational amplifier circuits in series. The electronics layout was designed by Sean Ravenhall[61] and I constructed a version of control box for the Sr experiment as shown in Fig 4.19.

[1]Ref [67] reported a similar scheme for Rubidium as our locking method at October, 2019, while our tunable MTS approach has been proposed and realised by us independently since March, 2019.

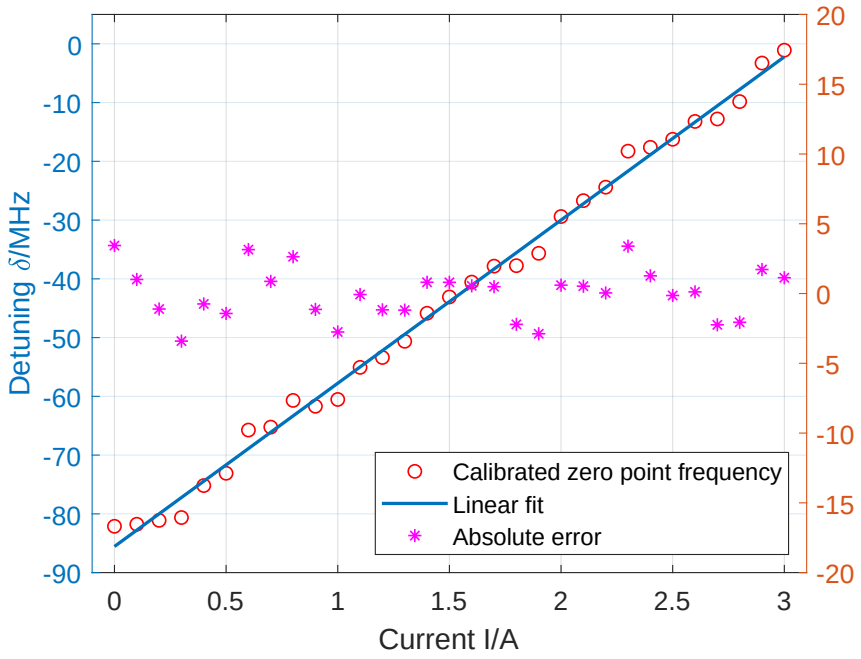


Figure 4.18: We fit the frequency detuning data with a linear line. The gradient is $27.8\,\mathrm{MHz\,A^{-1}}$ and the frequency offset (detuning) without current is $-85.5\,\mathrm{MHz}$, with uncertainty of $\pm 3.5\,\mathrm{MHz}$.

To lock the laser, we first use the wavemeter to manually tune the laser frequency close to the transition. Then, we start scanning the laser resonator frequency with the inbuilt scanning function on the laser interface and locate the MTS error signal. Then we gradually ramp down the scanning range and increase the gain of the feedback signal for slow piezo tuning (output after the second integrator, 'slow feedback' channel), so that the long term drift will be compensated. Then we can flip the single-pole, double-throw(SPDT) switch to send the feedback signal('fast feedback' channel) into fast piezo tuning channel (integrated output from the first integrator), so that fast drifts can be smoothed out and the laser's frequency is fully locked. By changing the current put through the pair of the MTS coils, the locked frequency can be freely tuned over range of 4Γ without re-locking.



Figure 4.19: This figure presents the box of home-built locking electronics. The MTS error signal goes into the first BNC channel on the left and the fast feedback output comes out from the second BNC channel from the left. The third BNC channel is for a external scanning signal, which is controlled by the SPDT (Single-Pole Double-Throw) switch named "external scan - fast int", which is designed to allow the user to externally scan the resonator. We use the inbuilt function of the SolsTiS interface for frequency scanning, so the SPDT (Single-Pole Double-Throw) switch is always left on the "Fast int" side, which means the two integrators are connected and no external scan signal is used. The trimmer potentiometer (trimpot, or variable resistor) adjusts the gain of the slow feedback signal.

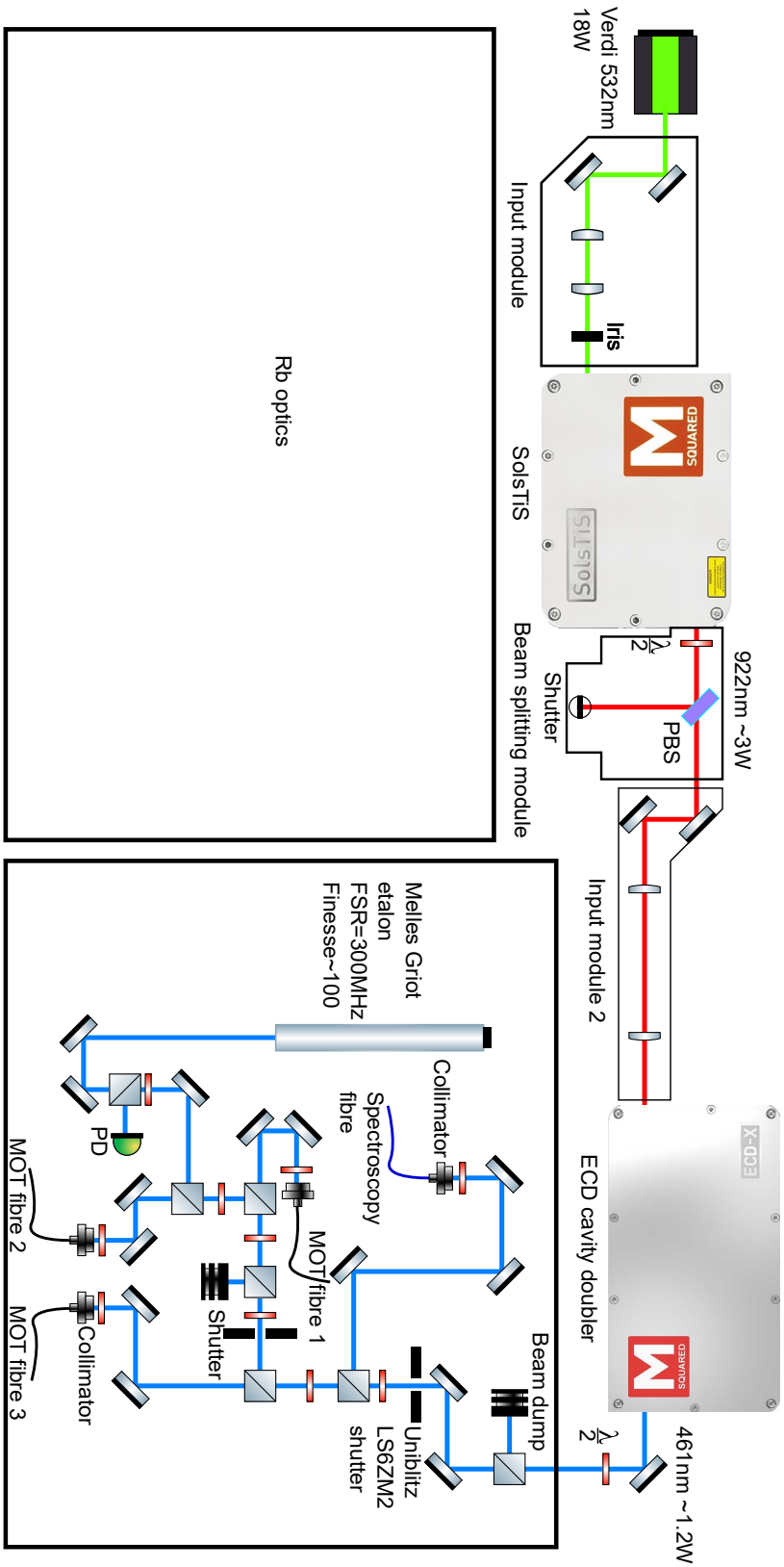


Figure 4.20: The SolsTiS laser can be switched to 780 nm for the Rb experiment and to 922 nm for the Sr experiment.

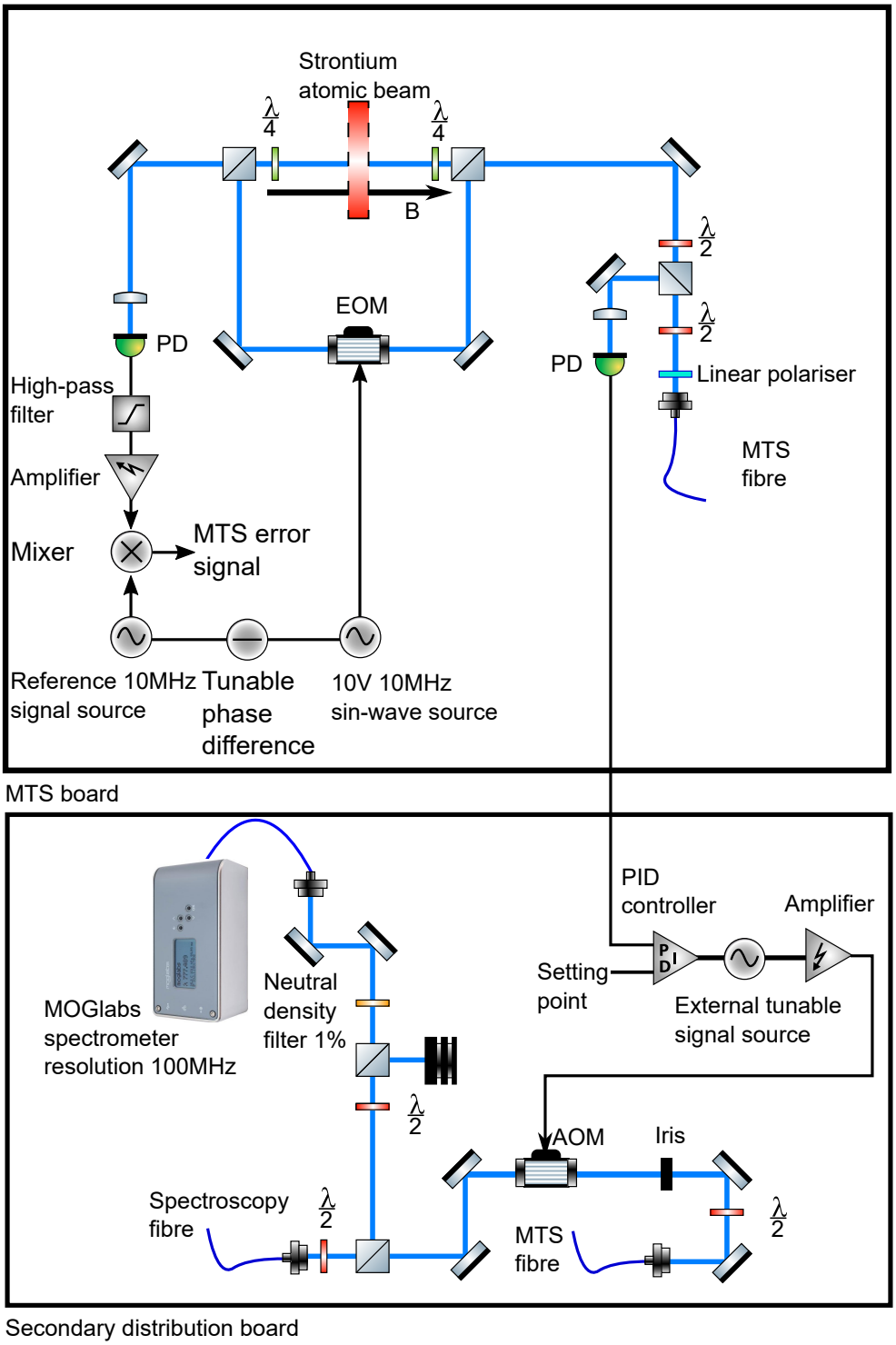


Figure 4.21: The second distribution board splits the input from main board into two parts: one for the wavemeter and one for the AOM.

Chapter 5

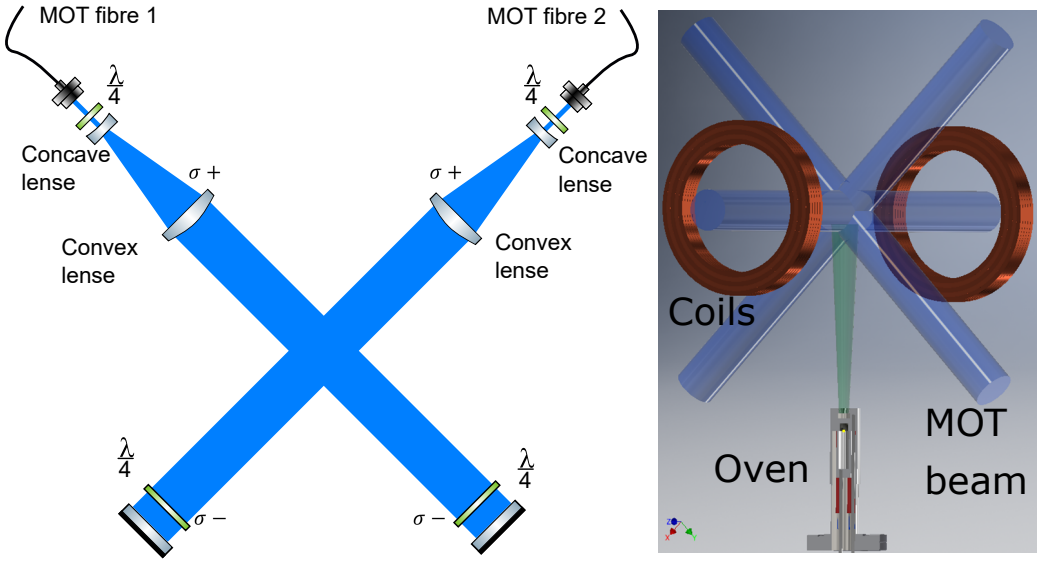
Magneto-optical trapping of strontium

5.1 MOT optics

Strontium has a very low vapour pressure at room temperature and the source must be heated to obtain a high flux of atoms. Strontium vapour will condense on cold surfaces (e.g. viewports), which can cause troubles for a Zeeman slower, as it requires a viewport in line of sight of the atomic oven. The viewport used for the Zeeman slowing beam is commonly heated up to avoid it becoming coated with strontium and opaque to the laser light. Our solution skips the usage of a Zeeman slower and relies on the direct trapping of atoms into a MOT from an atomic beam out of the oven. This approach can be effective even though the capture velocity of a MOT ($\sim 20\,\mathrm{m\,s^{-1}}$) is much lower than that for a Zeeman slower $> 150\,\mathrm{m\,s^{-1}}$. Our approach of using a MOT for direct trapping of strontium atoms is similar to that is reported in Ref [53], but we independently devised and started the experiment in January 2016. The arrangement of the optical components is shown in Fig 5.1a and the scheme of direct trapping is shown in Fig 5.1b.

5.2 Measurements for trapped atoms

After we observe the trapped atoms in the MOT as shown in Fig 5.2, we can optimise the performance of the MOT by aligning the polarisations and directions of MOT beam, and measure the loading rate of atoms while varying the field gradient, beam intensity, detuning and temperature.



(a) Optics used for x and y arm

(b) MOT beams with coils

Figure 5.1: (a) Two of the MOT beams are in the $x-y$ plane, and there is an additional arm along the z axis for the 3D MOT. Each quarter-wave plate sitting in front of the fibre output is aligned to convert linearly polarised light out of the fibre into circularly polarised beams with a proper handedness. Each quarter-wave plates in front of the mirror ensures that the reflected beam has the correct handedness.(b) The green beam refers to an atomic beam emitted. The three MOT beams (blue beams) construct a 3D molasses and form a 3D MOT with a pair of water-cooled coils, which can carry high currents.

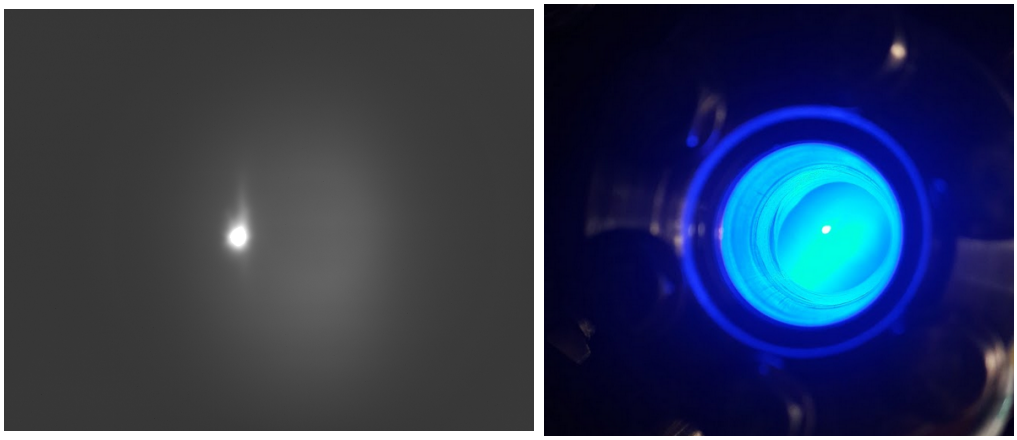
5.2.1 Optics for measurements

The basic method for measuring the loading of atoms is to record the intensity of the fluorescence either by photodiode or camera. Our measurements were taken with a photodiode (Thorlabs biased-detector DET36A2 for 350−1100 nm). We also tried the camera approach with a CCD camera from Thorlabs (CS505MU). The required optics are shown in Fig 5.3.

5.2.2 Data analysis

We calibrated the photodiode to get the ratio between the fluorescence power $P_d(t)$ measured and the voltage $V_d(t)$ on photodiode and , which is shown in Fig 5.4. The gradient is $k_d = 7.7\,\mu\text{W/V}$, and the total power received by the photodiode is $P_d = k_d V_d$, where V_d is the voltage read out from the photodiode.

We assume that the photons are scattered isotropically, so only those photons within a certain solid angle Ω can reach the photodiode's detecting surface. The



(a) MOT image on the Pixelink camera (b) MOT image on a cell phone

Figure 5.2: (a) An image taken with a CCD camera (fire-wire Pixelink) on a grey scale so white regions are high pixel counts. (b) An image taken with a cell phone camera.

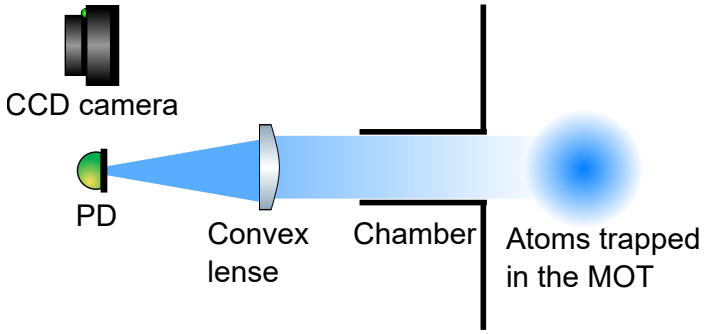


Figure 5.3: The convex lens focuses the florescence light onto the photodiode (or camera's CCD panel), and we can record the process of loading atoms into the MOT by monitoring the reading. Our vision for the cloud of trapped atoms is limited by the CF16 viewport on the chamber and the imaging lens.

distance between the imaging convex lens and the MOT centre is r =30 cm, and the lens has a focal length of D =7.5 cm and diameter of 1 inch (2.54 cm). So the solid angle of its effective aperture is

$$\Omega = 2\pi(1 - \cos\theta) = 2\pi(1 - \frac{r}{\sqrt{r^2 + (D/2)^2}}) \tag{5.1}$$

The imaging lens corresponds to a solid angle of 5.6×10^{-3} sr and open area of the CF16 viewport on the chamber corresponds to a solid angle of 3.3×10^{-2} sr. So, the total power of all emitted florescence photons is

$$P_{\text{total}} = \frac{4\pi}{\Omega} P_d = \frac{4\pi}{\Omega} k_d V_d. \tag{5.2}$$

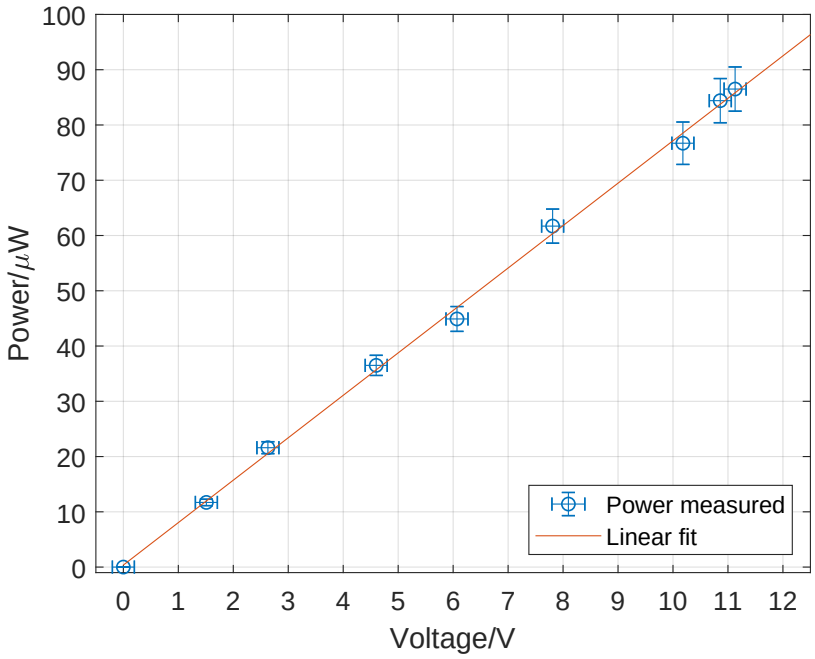


Figure 5.4: The voltage of the photodiode was measured with a multimeter and the power was measure with power meter (Ophir Nova II).

$N(t)$ is the number of atoms trapped in the MOT at time t, which can be expressed as

$$\frac{dN}{dt} = L - L_{\text{collision}} - L_{\text{dark}}, \tag{5.3}$$

$$= L - \frac{N}{\tau_{\text{collision}}} - \frac{N}{\tau_{\text{dark}}}, \tag{5.4}$$

$$= L - \frac{N}{\tau}, \tag{5.5}$$

where L is the loading rate of atoms into the MOT, $L_{\text{collision}}$ is the loss rate caused by collision of trapped atoms with background atoms, L_{dark} is the loss rate of atoms leaking into the dark state, τ_{dark} is the expected lifetime that an atom stays cycling on the cooling transition before leaking into the metastable triplet state (dark state), $\tau_{\text{collision}}$ is lifetime of atoms trapped in the MOT before being knocked out of the trap by collisions with other atoms, e.g. from the oven. So, the effective life time τ

$$\tau = \frac{1}{1/\tau_{\text{collision}} + 1/\tau_{\text{dark}}}. \tag{5.6}$$

We start with the MOT beams off, and the number in the MOT is zero. At $t = 0$ we turn the MOT beams on. When the MOT reaches equilibrium, $dN/dt = 0$. So

the solution for $N(t)$ is:

$$N = L\tau(1 - e^{-t/\tau}) \text{ for } (t \geq 0), \tag{5.7}$$

and the number of atoms trapped at equilibrium is

$$N_{eq} = L\tau. \tag{5.8}$$

With N_{eq} atoms trapped at the centre of the 3D MOT with a frequency detuning δ, the total energy of emitted florescence photons can be worked out from the scattering rate of photons. The intensity of MOT beams along x, y, z axis are $I_x, I_y\, I_z$, and the scattering rate of photons is

$$R_{\text{scat}} = \frac{\Gamma}{2} \frac{C_a I_{total}/I_{\text{sat}}}{1 + C_a I_{total}/I_{\text{sat}} + \delta^2/\Gamma^2}, \tag{5.9}$$

where C_a is a factor counting for the effective components of six MOT beams driving the transition, and $I_{total} = 2I_x + 2I_y + 2I_z$. The detailed analysis of how atoms interact with six MOT beams can be found in Ref [76]. A simple estimation suggested by Ref [70] is to ignore the magnetic field and assume that atoms are not localised, and so we can take $C_a = 1$; this is an overestimate of the true C_a and will hence lead to an underestimated atom number. So, the total energy of the photons emitted by trapped atoms at equilibrium state per unit time is

$$P_{\text{total}} = L\tau R_{\text{scat}} E_p \tau(1 - e^{-t/\tau}) \text{ for } t \geq 0, \tag{5.10}$$

where $E_p = hc/\lambda$ is the energy of a single photon, c is the speed of light. The voltage reading from the photodiode is (for $t \geq 0$)

$$V_d(t) = A_d(1 - e^{-t/\tau}) \text{ for } (t \geq 0). \tag{5.11}$$

where A_d is the amplitude and τ is the time constant. By fitting the voltage trace for loading with eqn. (5.11), we can get the amplitude A_d and time constant τ. The loading rate L can be expressed as

$$L = \frac{4\pi k_d A_d}{\Omega E_p R_{\text{scat}}} \frac{1}{\tau} \tag{5.12}$$

A typical loading curve and its fitting are shown in Fig 5.5, from which we can get τ and A_d. The initial sharp rise (jump) comes from florescence of atoms in the strontium vapour just after the shutter's opening and before atoms' loading. To compensate for the sharp jump at the beginning, we can add an similar exponential term to the

fitting. There are two exponential terms A_{shutter} and A_{mot}, as show in eqn. (5.15), accounting for amplitude of florescence contributed by opening of the shutter and the loading of the MOT respectively, with time constants τ_s and τ. Before recording a voltage trace for MOT loading, we would first record the sharp jump by turning on the shutter without applying the magnetic field, which can be used to fit the τ_s and A_s. The fitted shutter time constant is around 0.8 ms, and the opening time of the uniblitz shutter is around 1 ms according to the data sheet, which leads to an uncertainty of ± 1 ms for measurements of the time constant τ.

$$V_{\text{shutter}}(t) = A_s(1-e)^{-t/\tau_s} \text{ for } (t \geq t_s), \tag{5.13}$$

$$V_{\text{mot}}(t) = A_d(1-e)^{-t/\tau} \text{ for } (t \geq 0), \tag{5.14}$$

$$V_d(t) = V_{\text{shutter}}(t) + V_{\text{mot}}(t). \tag{5.15}$$

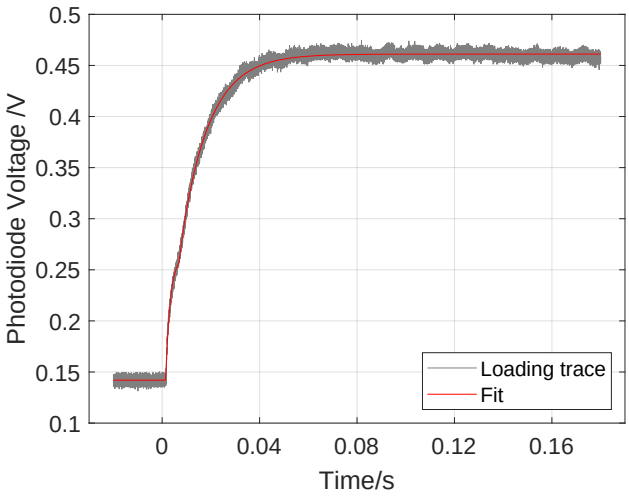


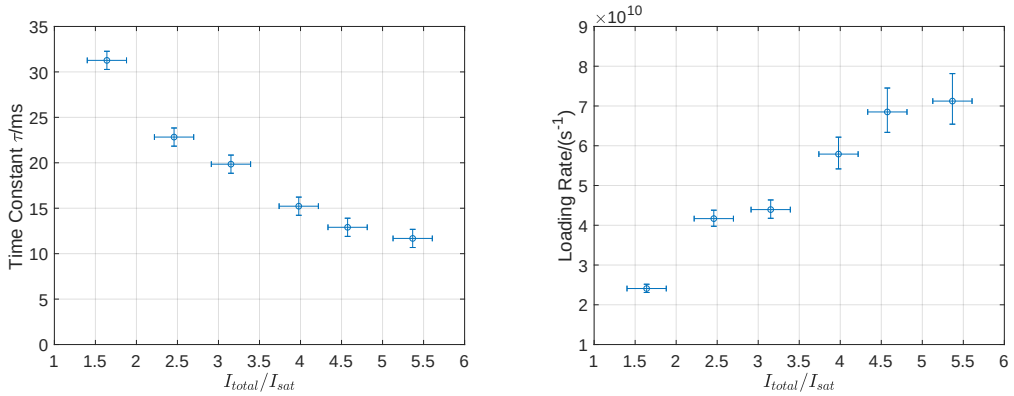
Figure 5.5: We find the time constant $\tau = 11.68$ ms and amplitude $A_d = 0.1976$ V by fitting the loading trace with eqn. 5.7.

5.2.3 Results

During the experiment, we searched the parameter space of oven temperature, detuning, gradient of magnetic field and beam intensity, so we can find the best set of parameters for optimizing the MOT's trapping. Over the following sections, our results are presented, analysed and explained.

5.2.3.1 Loading rate versus MOT beam intensity

With fixed frequency detuning $\delta = -3.1\,\Gamma$, field gradient $B'_z = 63.6\,\mathrm{G/cm}$ and oven temperature $T_o = 502\,^{\circ}\mathrm{C}$, we investigated the time constant τ and loading rate L as a function of total cooling beam intensities I_{total}, as shown in Fig 5.6. The optimised beam intensity is shown in Table 5.1 and the highest loading rate is $7.1 \times 10^{10}\,\mathrm{s}^{-1}$.



(a) Time constant versus $I_{\mathrm{total}}/I_{\mathrm{sat}}$ (b) Loading Rate versus $I_{\mathrm{total}}/I_{\mathrm{sat}}$

Figure 5.6: Time constants and loading rates measured over different $I_{\mathrm{total}}/I_{\mathrm{sat}}$ are shown here, with the detuning at $\delta = -3.1\,\Gamma$, the field gradient at $B'_z = 63.6\,\mathrm{G/cm}$ and the oven temperature at $T_o = 502\,^{\circ}\mathrm{C}$.

For trapping atoms from an isotropic vapour sample (such as Rb), MOT beams usually have the same intensity, but we are trapping atoms directly from an directional atomic beam with angular intensity distribution $I(\theta)$. This means that an uneven distribution of power within MOT beams can capture a higher fraction of the available atoms. The most probable velocity in an effusive beam with vapour temperature $T_v = 425\,^{\circ}\mathrm{C}$ is $[v_p]_{\mathrm{beam}} = 448\,\mathrm{m\,s^{-1}}$ and the full width half maximum (FWHM) of the velocity distribution is $425\,\mathrm{m\,s^{-1}}$, as shown in Fig 5.7. The divergence of the atomic beam can be defined by the full width half maximum condition $I(\theta_w) = I_0/2$ as $\theta_{\mathrm{FWHM}} = 2\theta_w = 0.17\,\mathrm{rad}\ (10^{\circ})$. So, the estimated values of the most probable velocity along the transverse direction (v_{pt}) and longitudinal direction (v_{pl}) are projections of $[v_p]_{\mathrm{beam}}$. We can get $v_{pl} = 447\,\mathrm{m\,s^{-1}}$ with FWHM $424\,\mathrm{m\,s^{-1}}$ and $v_{pt} = 0\,\mathrm{m\,s^{-1}}$ (by cylindrical symmetry) with FWHM $72\,\mathrm{m\,s^{-1}}$. This estimation shows that a stronger trapping force is required to decelerate the longitudinal velocity of atoms. As shown in Fig 5.8, the deceleration is larger with higher intensities under the condition that the intensity are not far above the saturation intensity I_{sat}. So, we distribute the laser power unevenly, with higher intensities in the vertical cooling beams.

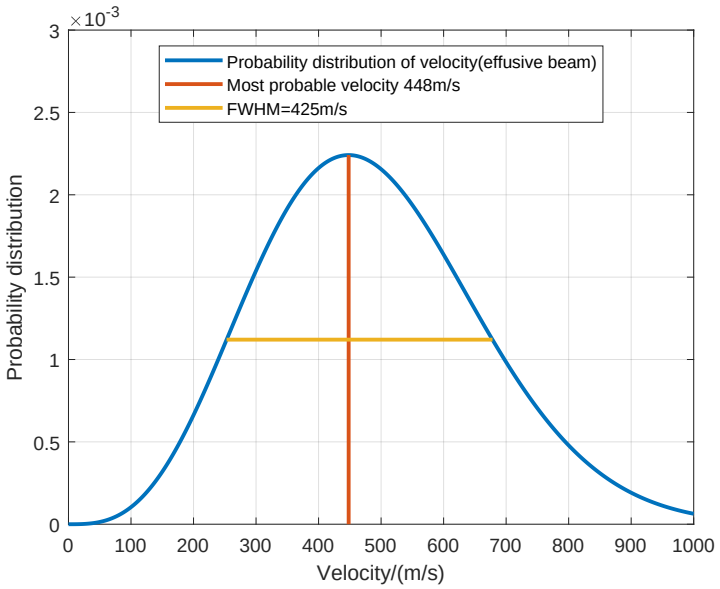


Figure 5.7: The probability distribution of velocities for an effusive beam with vapour temperature $T_v = 425\,^{\circ}\mathrm{C}$ ($T_o = 502\,^{\circ}\mathrm{C}$).

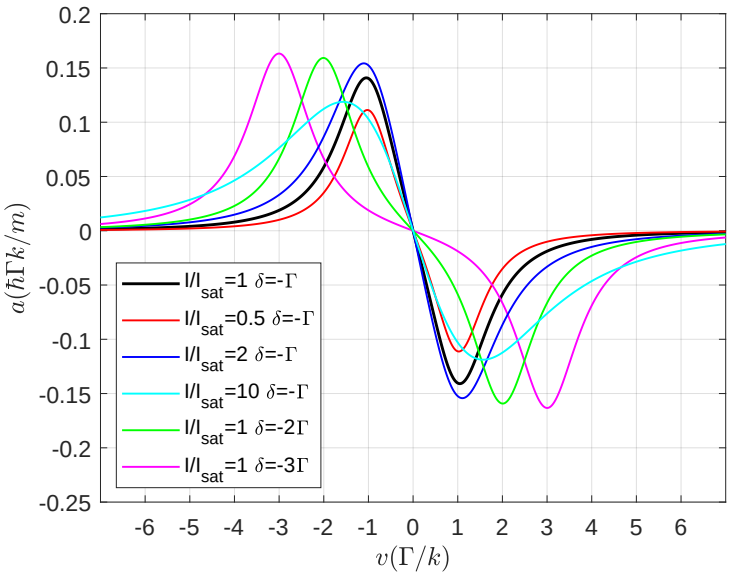


Figure 5.8: This figure presents the deceleration of atoms in a pair counter-propagating laser beams (molasses) under different intensities and frequency detunings. The deceleration and velocity are in units of $a_u = \hbar k\Gamma/m$ and $v_u = \Gamma/k$, which are commonly used to describe deceleration by the molasses force at a certain velocity. v_u is the widely-used estimation of the capture velocity.

Beam direction	Beam diameter /mm($1/e^2$)	Power/mW	I/I_{sat}
x	33	235	1.3
y	33	235	1.3
z	33	48	0.24

Table 5.1: The power in the $x-y$ MOT beams is five times of that in the z beam. The high-intensity beams' power was measured with a thermal power meter (Coherent 210) with $\pm 10\,\mathrm{mW}$ accuracy and the transverse beam power with a different power meter (Coherent Field Mate) to $\pm 2\,\mathrm{mW}$.

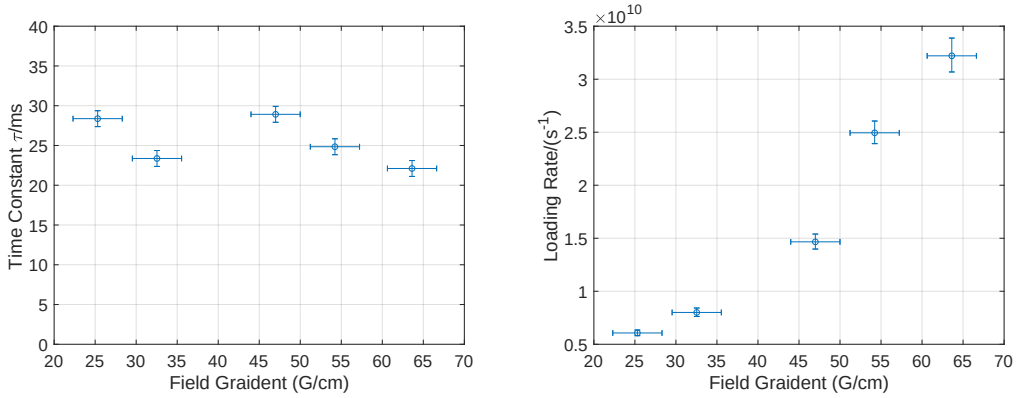
5.2.3.2 Loading rate versus the magnetic field gradient

The frequency detuning is set to $\delta = -3.1\,\Gamma$ and the oven temperature is at $502\,^{\circ}\mathrm{C}$. The loading rate increases with larger magnetic-field gradient as shown in Fig 5.9 up to $B'_z = 63.6\,\mathrm{G/cm}$, which corresponds to the highest current we can provide with our current supply. Increasing the magnetic-field gradient is expected to improve the loading rate up to a certain value determined by the maximum possible deceleration of the atoms.

5.2.3.3 Loading rate versus frequency detuning

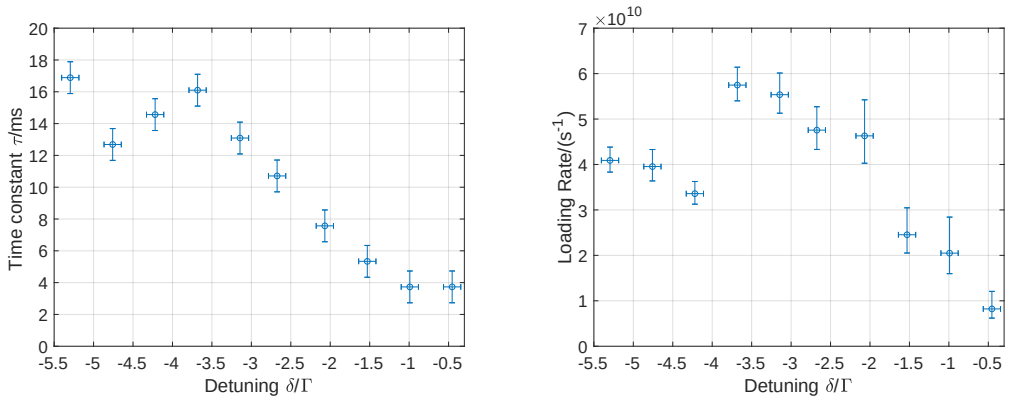
With the power distributed as in Table 5.1, a field gradient of $B'_z = 63.6\,\mathrm{G/cm}$ and an oven temperature $T_o = 502\,^{\circ}\mathrm{C}$, we investigated the time constant τ and loading rate L under various detunings, as shown in Fig 5.10. The optimum detuning is $\delta_0 = -3.7\,\Gamma$ with the highest loading rate as $5.7 \times 10^{10}\,\mathrm{s}^{-1}$.

The maximum deceleration of an atom by the molasses force is at $v = v_u$ when $\delta = -\Gamma$ ($v_c = 15\,\mathrm{m\,s}^{-1}$) and moves to $v' = 3v_u$ when $\delta = -3\Gamma$ as shown in Fig 5.8. At velocity v_u, the atom will see the maximum deceleration, so v_u is often referred as a simple underestimation for the capture velocity of a MOT at detuning $\delta = -\Gamma$. The real capture velocity is larger than v_u at detuning $\delta = -\Gamma$. The capture velocity increases as the laser frequency is shifted away from the resonance, but the deceleration for low-velocity atoms become smaller, implying longer time and longer distance for atoms to be fully trapped. In other words, the detuning range that can be used for the MOT trapping is limited by the beam size and intensity. Having large MOT beams allows us to explore frequency detunings further to the red than in most other MOT experiments.



(a) Time constant versus B'_z (b) Loading Rate versus B'_z

Figure 5.9: We also took data points with magnetic field gradient $B'_z \leq 20\,\mathrm{G/cm}$, but the time constants are obviously too large($\geq 140\,\mathrm{ms}$), which means there are basically no atoms loading into the trap. These large time constants could not be properly processed with the fitting, so we skip them. Loading rate increases with larger field gradient, with the detuning $\delta = -3.1\,\Gamma$ and the oven temperature at 502 °C. The x fibre outputs 230 mW and the y fibre outputs 240 mW, with z fibre outputs 45 mW. Since our apparatus is close to an ion pump magnet there is inaccuracy of the gradient ($\pm 3\,\mathrm{G/cm}$) from stay magnetic field, measured with a magnetic field meter. The maximum loading rate (3.2×10^{10}) is lower than that taken in Sec 5.2.3.3 and Sec 5.2.3.1 as intensities are not initially equal.



(a) Time constant versus detuning (b) Loading Rate versus detuning

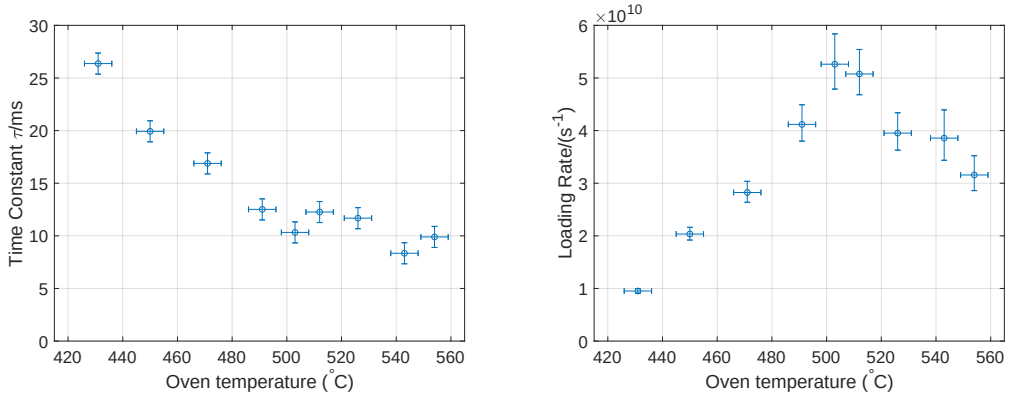
Figure 5.10: This figure presents the time constants and loading rates at different detunings with the power distributed as in Table 5.1, the field gradient $B'_z = 63.6\,\mathrm{G/cm}$ and the oven temperature at $T_o = 502\,°\mathrm{C}$. The laser locking has an frequency inaccuracy of $\pm 3.5\,\mathrm{MHz}$.

To explain how the capture velocity affects the loading rate into the MOT, we start by comparing cases of $\delta = -\Gamma$ and $\delta = -3\Gamma$ with vapour temperature $T_v = 425\,°\mathrm{C}$. If we set the capture velocities of the MOT to be $v_{cm} = 3v_u$ for $\delta = -\Gamma$ and $v_{cm} = 5v_u$ for

$\delta = -3\Gamma$, we can estimate the loading rate. The total flux and peak intensity for the atomic beam out of the nozzle at $T_v = 425\,^{\circ}\mathrm{C}$ are $7.5 \times 10^{14}\,\mathrm{s}^{-1}$ and $2.2 \times 10^{15}\,\mathrm{s}^{-1}\,\mathrm{sr}^{-1}$. The MOT beams have a diameter of 33 mm, so the total flux passing through the MOT region is $1.0 \times 10^{14}\,\mathrm{s}^{-1}$ according to the angular dependence function $j(\theta)$. For a given capture velocity v_{cm}, we can integrate the probability distribution function $f_b(v)$ to find the cumulative probabilities as $P(v \leq 3v_u) = 1.1 \times 10^{-4}$ and $P(v \leq 5v_u) = 1.6 \times 10^{-3}$, which represent the fraction of atoms that can be trapped. So, the estimated loading rate at $\delta = -\Gamma$ and $\delta = -3\Gamma$ are $1.1 \times 10^{10}\,\mathrm{s}^{-1}$ and $8.1 \times 10^{10}\,\mathrm{s}^{-1}$, which are close to our measurements.

5.2.3.4 Loading rate versus oven temperature

With beam power distributed as in Table 5.1, field gradient at $B'_z = 63.6\,\mathrm{G/cm}$ and detuning at $\delta = -2.7\Gamma$, we measured the time constant τ and loading rate L for various temperatures, as shown in Fig 5.11. The optimal oven temperature is $T_o = 502\,^{\circ}\mathrm{C}$ and the highest loading rate is $5.3 \times 10^{10}\,\mathrm{s}^{-1}$.



(a) Time constant versus T_o (b) Loading rate versus T_o

Figure 5.11: This figure presents the time constants and loading rates at various oven temperatures. The beam power is distributed as in Table 5.1, field gradient is $B'_z = 63.6\,\mathrm{G/cm}$ and the detuning is $\delta = -2.7\Gamma$. Temperature measurements have an inaccuracy of $\pm 5\,^{\circ}\mathrm{C}$ for the K-type thermocouple.

When the vapour temperature is above 450 °C(oven temperature $T_o \geq$530 °C), the mean free path of atoms in the atomic beam is shorter that the distance between the nozzle and the centre of MOT $L_{nc} = 83\,\mathrm{mm}$. So atoms in the atomic beam can collide with each other before reaching the MOT region, leading to a drop in the loading rate.

5.2.3.5 Analysis of the losses

The loading rate L at equilibrium equals the sum of all loss terms

$$L = L_{\text{collision}} + L_{\text{dark}}, \tag{5.16}$$

where $L_{\text{collision}} = N_{eq}/\tau_{\text{collision}}$ and $L_{\text{dark}} = N_{eq}/\tau_{\text{dark}}$. The mean collision time is

$$\tau_{\text{collision}} = \frac{1}{n\sigma \langle v_{re} \rangle}, \tag{5.17}$$

where the collision cross-section $\sigma = \pi d^2 = 5.3 \times 10^{-19}\,\text{m}^2$, d is the diameter of a strontium atom)[12] and the mean relative velocity $\langle v_{re} \rangle$ is given by

$$[\langle v_{re} \rangle]_{\text{beam}} = \frac{\sqrt{\pi}}{2v_p} \langle v^2 \rangle \tag{5.18}$$

$$= \frac{\sqrt{\pi}}{2v_p} \frac{3k_{\text{B}}T}{M}. \tag{5.19}$$

We can get $\langle v_{re} \rangle = 486\,\text{m}\,\text{s}^{-1}$ at the oven temperature $T_o = 502\,^{\circ}\text{C}(T_v = 425\,^{\circ}\text{C})$. The number density n at the position of the MOT centre (which lies on the centreline of the atomic beam) is

$$n(v) = \frac{f_b(v) I_0 j(0)}{v L_{nc}^2}, \tag{5.20}$$

where I_0 is the peak intensity of an ideal atomic beam. Hence,

$$\langle n \rangle = \frac{\sqrt{\pi}}{2v_p} \frac{I_0 j(0)}{L_{nc}^2}, \tag{5.21}$$

where $L_{nc} = 8.3 \times 10^{-2}\,\text{m}$ is the distance between the nozzle and the MOT centre. This implies a collision rate of

$$\Gamma_{\text{collision}} = \frac{1}{\tau_{\text{collision}}} = \frac{3\pi^2 d^2 I_0 j(0)}{8 L_{nc}^2}, \tag{5.22}$$

which is shown in Fig 5.12. So, the collision rate $1/\tau_{\text{collision}} = 0.2\,\text{s}^{-1}$, which is rather small compared with the loss rate into the dark state.

The loss rate of atoms leaking into the dark state is

$$\Gamma_{\text{dark}} = \frac{1}{\tau_{\text{dark}}} = B_{br} R_{scatt} = \frac{B_{br}\Gamma}{2} \frac{C_a I_{total}/I_{\text{sat}}}{1 + C_a I_{total}/I_{\text{sat}} + 4\delta^2/\Gamma^2}, \tag{5.23}$$

where the branching ratio into the metastable dark state is $B_{br} = 6.6 \times 10^{-6}$, $I_{total} = 2I_x + 2I_y + 2I_z$ and C_a equals 1 for the ideal cases. Rather than doing complicated

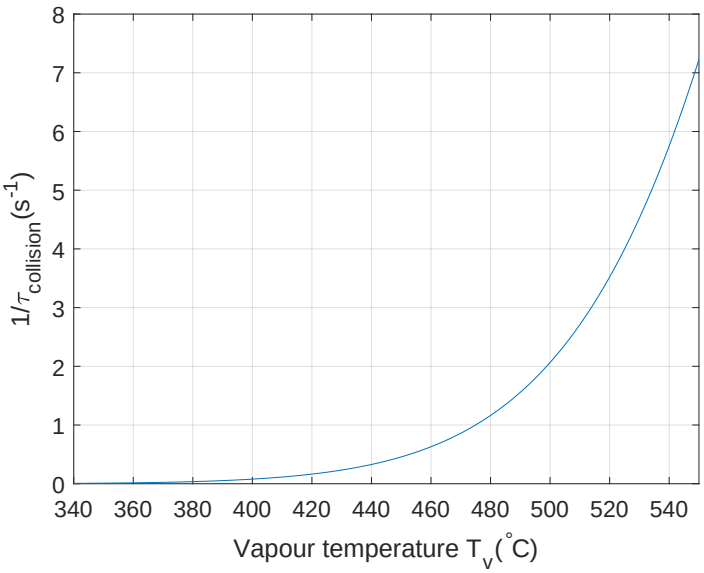


Figure 5.12: The collision rate between trapped atoms and atoms in the background atomic beam is negligible for the temperature we are working in and the mean-free path is a more limiting factor that cause the drop of the loading rate at higher temperatures.

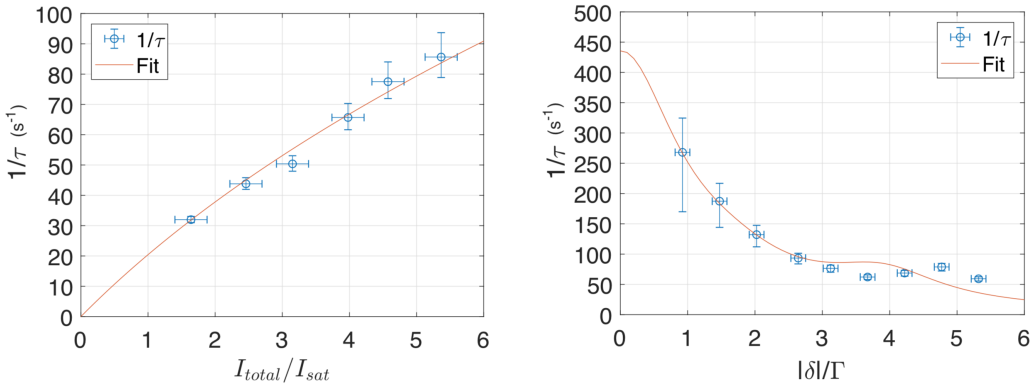
analysis as Ref [76], we use C_a at the denominator to account for the effective components of six beams. Then we can use our data of time constants τ to get its value. As the collision rate $1/\tau_{\text{collision}} = 0.2\,\text{s}^{-1}$ is small at $T_o = 502\,^{\circ}\text{C}$ ($T_v = 425\,^{\circ}\text{C}$), we can assume the dominant loss of trapped atoms is leaking into dark states, So, $1/\tau$ is roughly equal to $1/\tau_{dark}$:

$$\frac{1}{\tau} = \frac{1}{\tau_{\text{collision}}} + \frac{1}{\tau_{\text{dark}}} \approx \frac{B_{br}\Gamma}{2} \frac{C_a I_{total}/I_{\text{sat}}}{1 + C_a I_{total}/I_{\text{sat}} + 4(\delta/\Gamma)^2}. \tag{5.24}$$

Fitted results are shown in Fig 5.13 and $C_a = 0.6$ with inaccuracy ± 0.1.

We also used a camera instead of a photodiode, to measure the loading rate from pictures taken every 200 µs (shutter time T_{shutter}). The second round of measurements with camera were done with an entirely different vacuum system (extended with a scientific chamber), optics, control system (automated with Artiq boards) and equal beam intensities in all three MOT beams. With smaller beam diameters (18 mm) and lower available power for each MOT beam (72 mW), the performance cannot be compared to the first measurement.

By fitting the pixel counts $N_p(t)$ to an exponential curve as in eqn. (5.11), we can find the pixel count amplitude A_p and time constant τ. The expression for the



(a) $1/\tau$ versus I_{total}/I (b) $1/\tau$ versus δ/Γ

Figure 5.13: Measurements of the lifetime against (a) the total intensity I_{total}/I_{sat} for a fixed detuning $\delta = -3.1\,\Gamma$ and (b) the absolute value of frequency detuning for a fixed total intensity $I_{total} = 5.6\,I_{sat}$. Other parameters are the same for both figures: the field gradient $B' = 63.6\,\mathrm{G/cm}$, oven temperature $T_o = 502\,^\circ\mathrm{C}$. The kink come from ^{86}Sr, which is the second most abundant stable isotope.

loading rate is

$$L = \frac{4\pi A_p}{\Omega_c T_{\mathrm{shutter}} q_e R_{\mathrm{scat}}} \frac{1}{\tau}, \tag{5.25}$$

where the shutter time $T_{\mathrm{shutter}} = 200\,\mu\mathrm{s}$, the quantum efficiency $q_e = 65\%$. The solid angle $\Omega_c = 3.3 \times 10^{-2}\,\mathrm{sr}$ is limited by the CF16 viewport, rather not by the imaging lens which has a diameter of 6.35 cm and sits at 14 cm away from the MOT centre. Data are shown in Fig 5.14. The maximum loading rate can be achieved with the oven temperature at $T_o = 502\,^\circ\mathrm{C}$ is $6.8 \times 10^9\,\mathrm{s}^{-1}$ with $\delta = -3.1\,\Gamma$ and $I_{total} = 7.7\,I_{\mathrm{sat}}$.

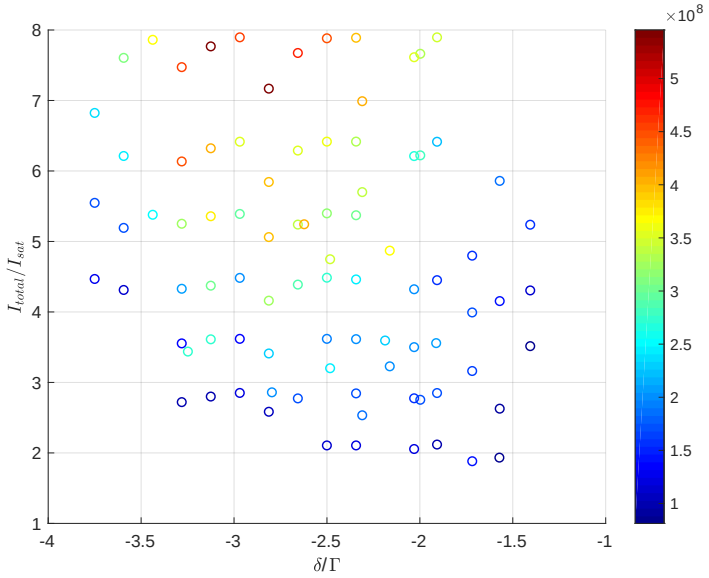


Figure 5.14: The optimal detuning is around $-3.1\,\Gamma$ and loading rate is higher with stronger beam intensities. The maximum loading rate is $5.5 \times 10^8\,\mathrm{s}^{-1}$ and all data points are taken at the oven temperature $T_o = 502\,^{\circ}\mathrm{C}$. The performance is not comparable to the first set-up as beam diameters are reduced and available power is limited.

Chapter 6

Conclusion and outlook

The aim at the start of this project was to make a novel source of strontium for various quantum technology applications such as atomic clocks. As mentioned in the introduction, this was motivated by the success of the 2D MOT for sodium[40] and the investigation that showed that this approach gives a flux of cold atoms similar to a long Zeeman slower [58]. It seems that the group in University of Science and Technology of China[53] also independently reached similar conclusions; that research group demonstrated some aspects of the scheme before us but they did not give much consideration to the design of a suitable atomic oven. Our work is complementary in that we concentrated on developing a new oven which is time-consuming. At the start of this project we had no equipment or laser systems for work with strontium and so all the apparatus was constructed during the project period. For 15 months we had a joint grant with M Squared Lasers which was helpful in some respects but also involved a considerable amount of quarterly reporting and frequent meetings. Overall the project received financial input from a variety of sources including partnership funding from the National Quantum hubs; both from the hubs for Quantum Sensors and Metrology (led by Professor Kai Bongs in Birmingham) and also from the NQIT hub (led by Professor Ian Walmsley in Oxford). These many short-term grants were essential for being able to carry out this work but this made progress slower than it would have been if the project direction was clear from the beginning.

Since January 2019, the research group in Oxford became involved in preparing a proposal to construct a large-scale atom interferometer in the newly-constructed low-vibration Beecroft building in Oxford Physics and an essential requirement is a high-flux source of Sr to achieve a good signal-to-noise ratio. This changed our outlook since it was no longer important to worry about the size or power consumption of the strontium source (within some reasonable limits). A proposal for the AION project (Stage 1) was submitted in Dec 2019, and it is linked to the MAGIS project in the US,

for which is already funded and preliminary work has been carried out at Stanford University[30]. Therefore the development of a high-flux source is demanded.

The long-term vision of AION has 4 stages: Stage 1 to build a 10 m detector and to develop technology for a 100 m detector, Stage 2 is constructing the 100 m detector and doing design study for the km-scale. Stage 3, is a full-scale kilometre-scale device on earth, and Stage 4, would be a satellite-based gravitational waves (GW) detector spanning thousands of kilometres. The ultimate objective of these large-scale devices is to create a new technology for detecting gravitational waves from astrophysical sources in the mid-frequency band ranging from several mHz to a few Hz, which is mostly inaccessible as yet. These devices will be developed and tested for searching for dark matter (DM). The sensitivity of these quantum sensors comes from interference of atomic wave packets and takes advantage of the special features of strontium.

The AION-10 instrument will have two atom interferometers inside a $\sim$10 m vacuum system (Fig 6.2– which was prepared for the proposal by Dr Elliot Bentine). The laser beams that split and recombine the wave packets goes vertically through both interferometers so that there is common-mode rejection of noise in differential measurements, i.e. for the gradient of gravity. Detail of the interferometry are not given here, but it is relevant to describe how the source will be used. Our design of source is shown in the Fig 6.2, and atoms from the 2D MOT are collected in a 3D MOT with blue light. These atoms are transferred to a red MOT (689 nm) to be cooled further as explained in Chapter 1.

These cold atoms are then transported horizontally into the main interferometer tube ready for launching upwards. This transport stage is not the responsibility of the Oxford group but is likely to involve moving the focal spot of a high power laser beam that dipole traps the cold atoms (so-called optical tweezers). The time of flight in the interferometer is several seconds (for a launch height of 4 m) and the atoms must have a very low temperature to stop them spreading out too much and being lost. Having a compact cloud of atoms is also important to minimise problems from imperfections in the wavefronts of the laser beams (that directly cause phase-shift of the interference pattern). The initial object in AION is to reach 20 nK by either evaporative cooling or decompression cooling and then aim for $<$1 nK directly before launching the interferometer sequence. The set up to do this, shown in Fig 6.2, is called the side-arm and two will be installed on the 10m apparatus. To meet the sensitivity target of the first stage of AION requires launching 10^8 atoms of ^{87}Sr and multiple launches per second (interleaving of the clouds) which is far beyond the current state of the art. The proposals also have ambitious targets for the number

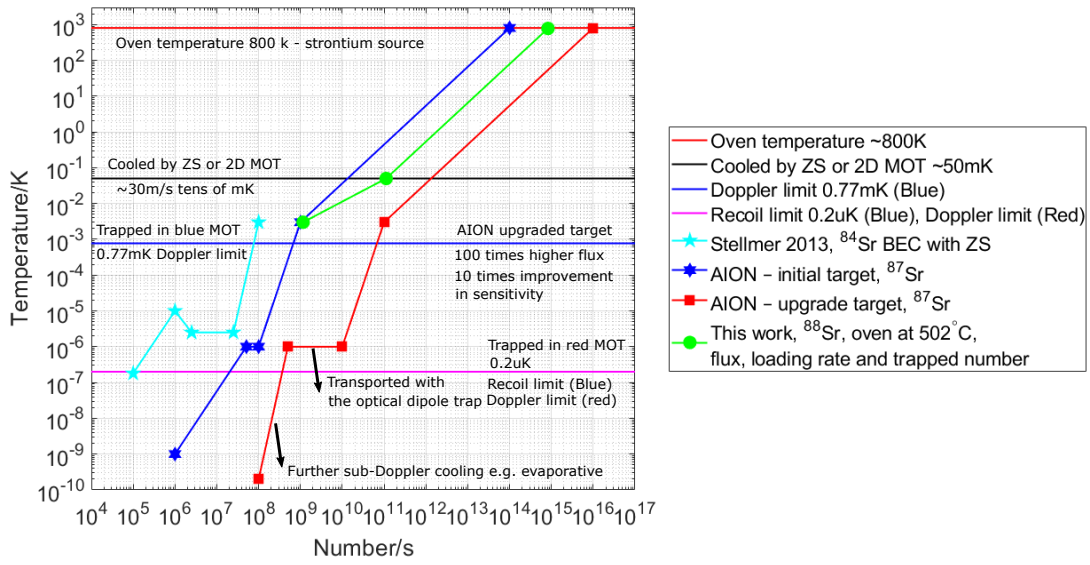


Figure 6.1: Stages required for a BEC of strontium atosm are shown by those horizontal solid lines. When transporting atoms in the optical dipole trap, atoms can be heated. Our experiment with MOT has satisfy the initial requirement for AION project. To satisfy the demand of upgraded AION project, we will have to use repumping lasers and even adapt the oven's size according to the required number.

of laser pulses used to split the atomic wave packets (1000) and improvement of the sensitivity using squeezing. In contrast, increasing the size of the strontium oven to improve the atomic flux and measured signals is a straightforward approach that can be implemented by following the fundamental properties of atomic beams that this thesis has explored. This work provides the guiding principles for the design of a larger atomic source.

The development of atomic ovens always involves trial and error but we have not followed many false directions. Things that can be investigated in the future are:

1. Making a nozzle with a larger area, both physically larger and having a larger total area of exit holes to give more atomic flux at a given temperature (the maximum operating temperature set by the criterion given in Chapter 3). There is some room to do this within a 70 mm ID tube as in the current design, but going up to the next standard size of 100 mm would be straightforward with only a moderate increase in the power consumption of the heaters. It is easy to supply more electrical power but this must be dissipated somewhere and we do not want a source of more than around 100 W of heat on the apparatus (since the interferometer optics must be as stable as possible).

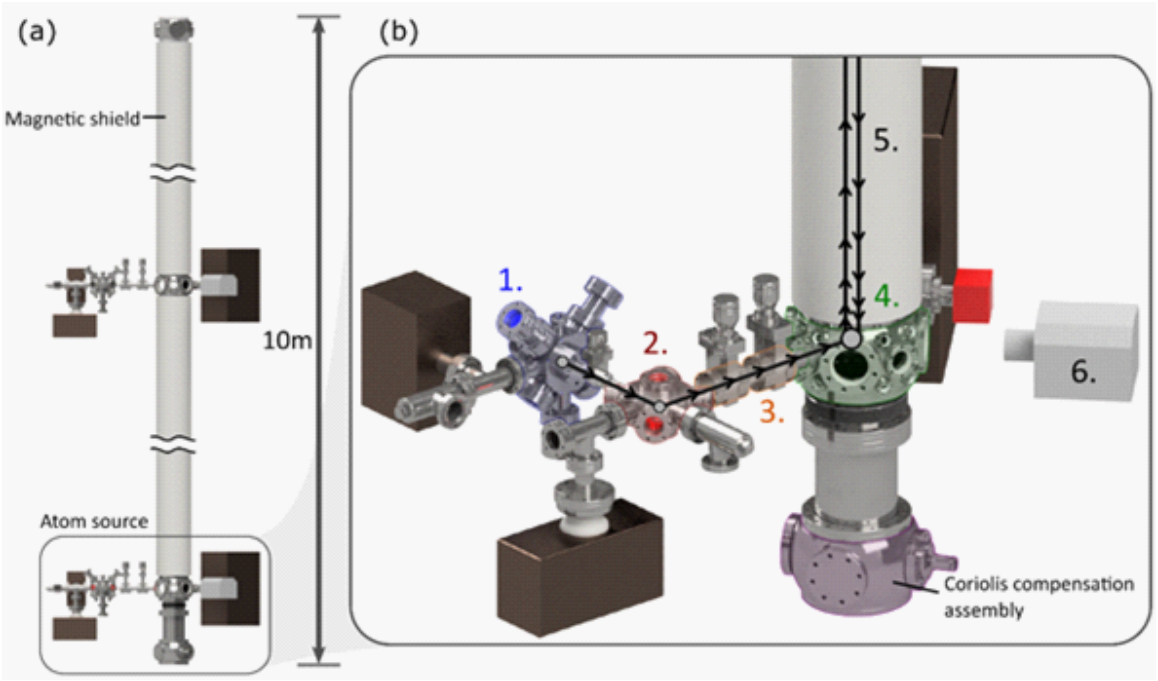


Figure 6.2: (a) The AION-10 vacuum system, showing two atom sources and magnetic shielding. The long free-fall sections are shown with a discontinuity for clarity. (b) Details of a side-arm. (1) After effusing from an oven, strontium atoms are laser-cooled in a 2D magneto-optical trap (MOT), then (2) cooled in a 3D MOT using firstly a broad (blue) transition and then a narrow (red) transition. (3) Cold atoms are transported to a chamber, where (4) they are launched upwards and (5) follow a parabolic free-fall trajectory, during which the interferometry sequence is performed. (6) Readout using an imaging system.

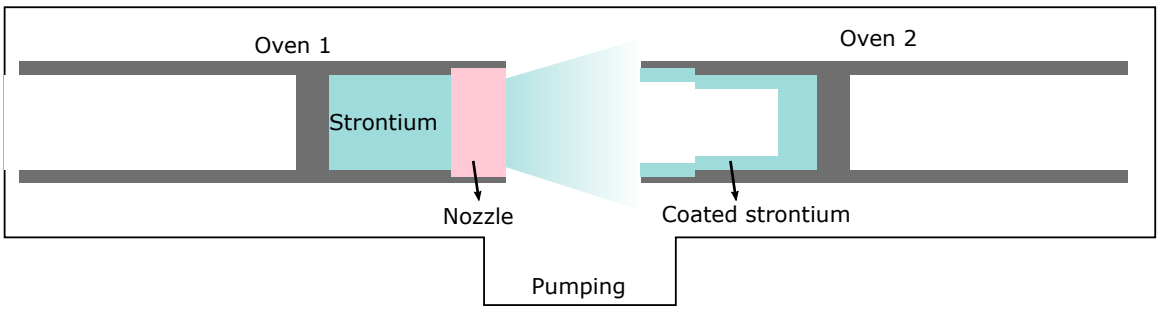


Figure 6.3: Oven 1 contains a large piece of strontium and continuously generate a high flux of strontium atoms and the second oven is coated with layers of strontium. Impurities that can be vaporised will be pumped out.

2. Making the nozzle from stainless steel rather than graphite, which can avoid differential thermal expansion.

3. Using repumping laser(s) to drive suitable transitions in the MOT. Ref [53] reported an order of magnitude increase of the atom number with 481 nm repumping light.

4. Loading the oven by directly distilling strontium into it as shown in Fig 6.3. This would enable relatively cheap industrial-grade metal to be used rather than expensive research grade material. We had some vacuum problems from the mineral oil used to store strontium granules which should be avoided in future.

Appendix A

Thermal analysis of oven

A.1 Oven features

Data for the power consumption, thermocouple readings and the estimated nozzle temperature are presented in Sec 3.1.1, for the range from 400 °C to 650 °C. Measurements were taken over a wider range but with a larger sample spacing as shown in Fig A.1, Fig A.2 and Fig A.3.

A.2 Radiation exchange between surfaces

We can model the process of net radiation exchange between two grey surfaces by adding up the series of reflections, as illustrated by the upward and downward arrows in Fig A.4. There are two surfaces facing each other with their own emissivity, absorptivity and reflectivity.

In the first round, P_{rad1} is emitted from the surface 1 to surface 2, and a power P_{re} is reflected back:

$$P_{rad1} = \varepsilon_1 \sigma A T_1^4, \tag{A.1}$$

$$P_{re1} = \rho_2 P_{rad1}. \tag{A.2}$$

Part of P_{re} is absorbed and rest of it is then reflected off surface 1 again, which is P_{rad1} noted in Fig A.4. So the second round of radiation exchange

$$P_{rad2} = \rho_1 P_{re} = \rho_1 \rho_2 P_{rad1}, \tag{A.3}$$

$$P_{re2} = \rho_2 P_{rad1} = \rho_1 \rho_2^2 P_{rad1}. \tag{A.4}$$

Similarly for the i-th round of the radiation exchange is

$$P_{radi} = (\rho_1 \rho_2)^i P_{rad1}, \tag{A.5}$$

$$P_{rei} = (\rho_1 \rho_2)^i \rho_2 P_{rad1}. \tag{A.6}$$

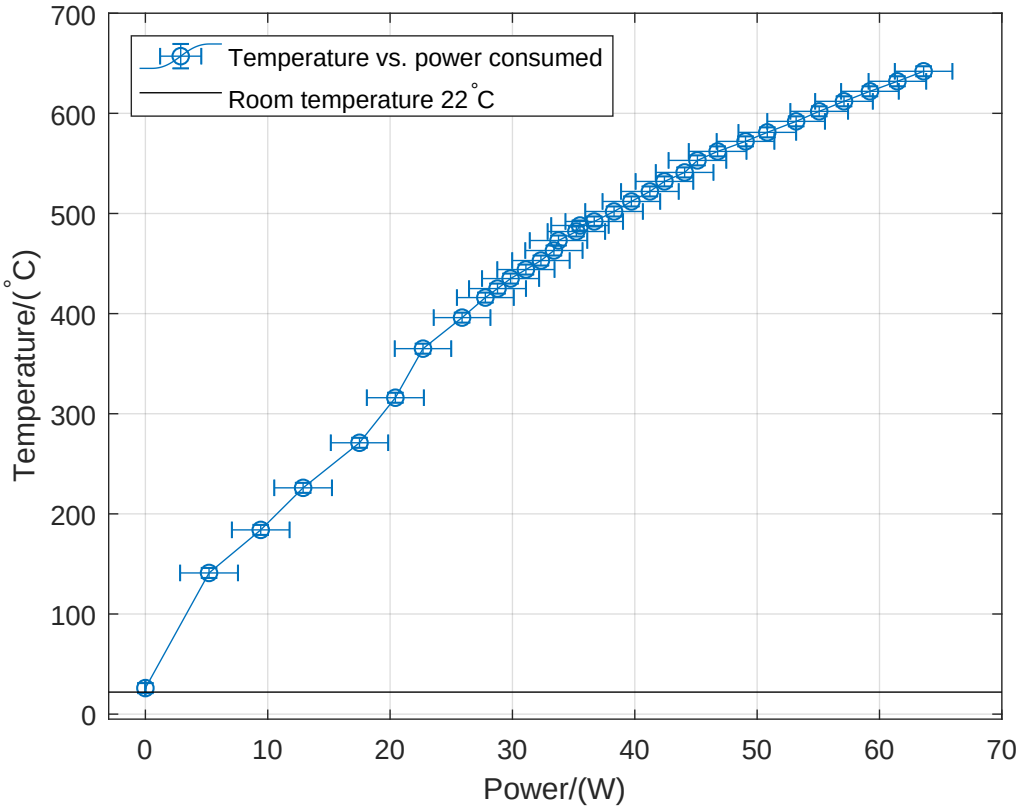


Figure A.1: The temperature of the oven increase with more heater power. We took more data points over the interested region from 400 °C to 650 °C.

So, the total radiative heat loss from surface one to surface two is

$$\begin{aligned} P_{rad12} &= \sum_{i=0}^{\infty} P_{radi} - \sum_{i=0}^{\infty} P_{rei}, \\ &= \sum_{i=0}^{\infty} (\rho_1\rho_2)^i P_{rad1} - \sum_{i=0}^{\infty} (\rho_1\rho_2)^i \rho_2 P_{rad1}, \\ &= \sigma A T_1^4 \frac{\varepsilon_1\varepsilon_2}{\varepsilon_1 + \varepsilon_2 - \varepsilon_1\varepsilon_2}. \end{aligned} \tag{A.7}$$

Similarly, the total radiation given out by surface two towards surface 1 is

$$P_{rad21} = \sigma A T_2^4 \frac{\varepsilon_2\varepsilon_1}{\varepsilon_1 + \varepsilon_2 - \varepsilon_1\varepsilon_2}. \tag{A.8}$$

For this particular simplified case, both surfaces are assumed to be with same area A. A more thorough treatment involves more discussions about directions and geometry of both surfaces, which can be found in Ref [32]. So the net radiation transfer from

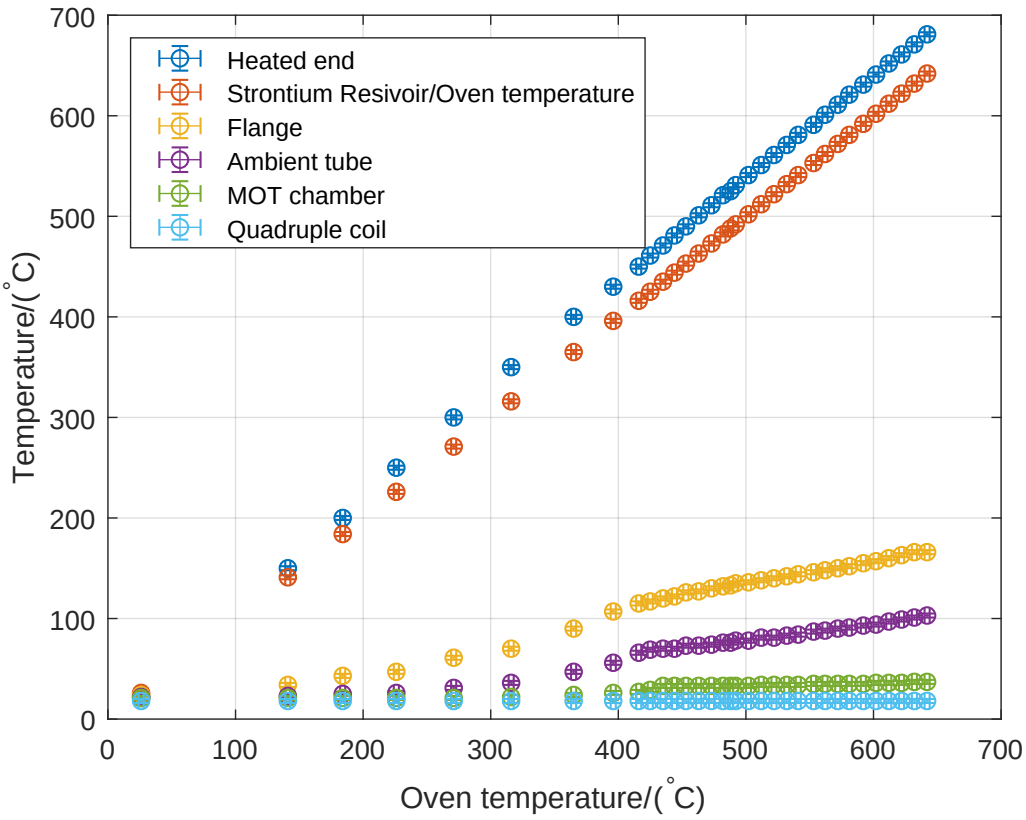


Figure A.2: The temperature of various parts of the apparatus for different oven temperatures. The error bar of the temperature measurements comes from inaccuracies of the K-type thermocouple, which is $\pm 5\,^{\circ}\mathrm{C}$.

surface one to surface two is

$$\begin{aligned} P_{net12} &= P_{rad12} - P_{rad21}, \\ &= \frac{\sigma A \varepsilon_1 \varepsilon_2}{\varepsilon_1 + \varepsilon_2 - \varepsilon_1 \varepsilon_2} (T_1^4 - T_2^4). \end{aligned} \tag{A.9}$$

A.3 Heat shield

Derivations above for radiation exchange between surfaces can be applied for the case with a layer of heat shield in between. For simplicity, we assume that heat shield inserted between is using the same material as surface one and two, with emissivity ε. So the radiation transfer from surface one to the shield and shield to surface two

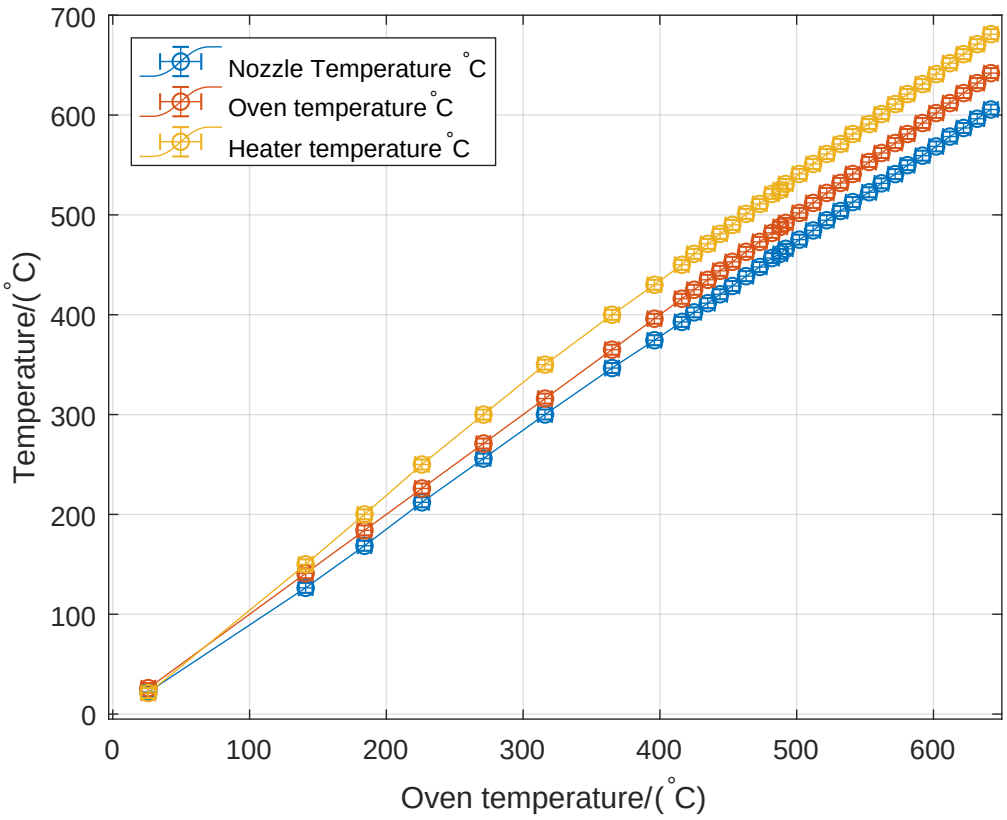


Figure A.3: The nozzle temperature predicted is lower than the oven temperature and that of the heaters. We did not observe clogging over many days running which is contrary to the common belief that the nozzle should be tens of degrees hotter than the oven to avoid build up of material.

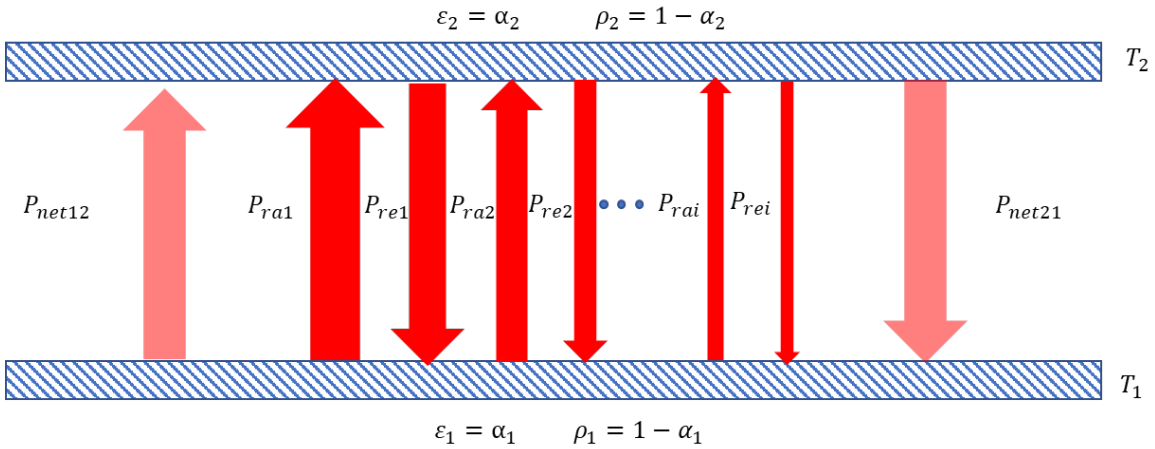


Figure A.4: A grey body does not absorb radiation completely so the radiation emitted will bounce between the two surfaces.

are

$$P_{rad1S} = \frac{\sigma A \varepsilon}{2-\varepsilon}(T_1^4 - T_s^4), \tag{A.10}$$

$$P_{radS2} = \frac{\sigma A \varepsilon}{2-\varepsilon}(T_s^4 - T_2^4). \tag{A.11}$$

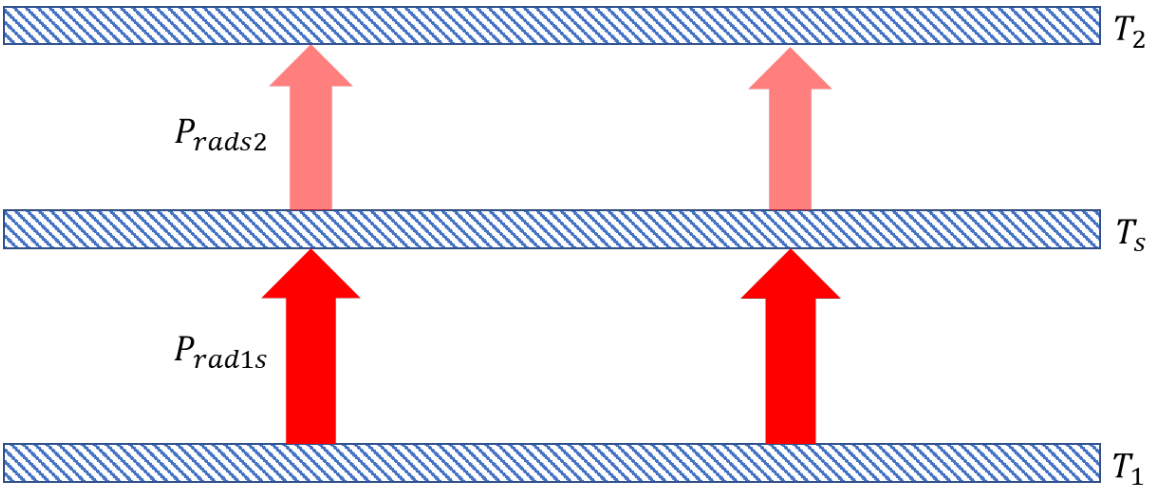


Figure A.5: Heat shield between two surfaces can help to reduce the total radiation loss from the hotter one.

And at equilibrium state, we can get

$$P_{rad1S} = P_{radS2}, \tag{A.12}$$

$$P_{rad1S} + P_{radS2} = \frac{\sigma A \varepsilon}{2-\varepsilon}(T_1^4 - T_2^4). \tag{A.13}$$

So the existence of heat shield helps to reduce the heat radiation transfer by half

$$P_{rad1S} = \frac{1}{2}P_{net12}, \tag{A.14}$$

$$= \frac{1}{2}\frac{\sigma A \varepsilon}{2-\varepsilon}(T_1^1 - T_2^4). \tag{A.15}$$

A.4 Temperature distribution over the outer surface

The outer surface can be divided into three parts according to the cross-section area, which are noted as L_{cn}, L_{nj} and L_{jf}. Only T_n (hot end) and T_f (flange) are known from the thermocouple measurements and T_j amd T_c have to be estimated. We

can treat the outer surface as three cylindrical tube joined together at point x_n and x_j.Heat is source is located at x_n, so T_n should be higher than T_c.

According to eqn. (3.9) and eqn. (3.4), we can know that

$$-kA_{c0}\frac{T_n - T_c}{L_{cn}} = -kA_{c1}\frac{T_n - T_j}{L_{nj}},$$
$$-kA_{c1}\frac{T_n - T_j}{L_{nj}} = -kA_{c2}\frac{T_j - T_f}{L_{jf}},$$

, and we can get

$$T_j = (\frac{A_{c1}}{L_{nj}}T_n + \frac{A_{c2}}{L_{jf}}T_f)\Big/(\frac{A_{c1}}{L_{nj}} + \frac{A_{c2}}{L_{jf}}),$$
$$T_c = T_n - (\frac{A_{c1}}{L_{nj}}T_n - \frac{A_{c1}}{L_{nj}}T_j)\Big/\frac{A_{c0}}{L_{cn}}. \tag{A.16}$$

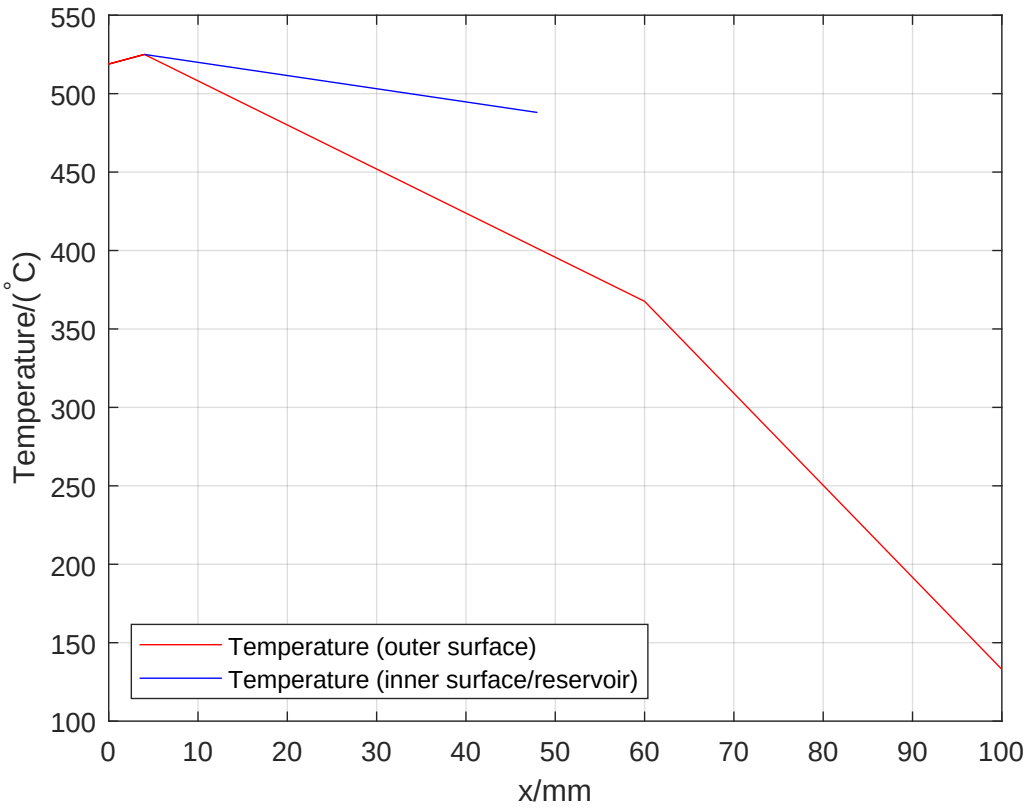


Figure A.6: The outer surface's temperature is described as three linear functions connecting each other. This diagram is only for estimation of power loss. The oven is at 488 °C for this figure.

A thin-wall design leads to larger temperature drop over L_{jf} so temperature at flange can be lower, which can help to reduce conduction, and convection loss from

the flange. Heat loss by radiation can be To even reduce the flange temperature T_f, we reduce the wall thickness from 1 mm to 0.25 mm for the new spectroscopy oven. Knowing the temperature distribution $T_1(x_1) = (T_j - T_n)x_1/L_{nj} + T_n = G_{T1}x_1 + T_n$, we can get total heat loss by radiation P_{lr} over length L_{nj}

$$\begin{aligned} P_{lr1} &= \int_0^{L_{nj}} \frac{\sigma\varepsilon\pi r_{o1}}{2-\varepsilon}(T_1^4 - T_{am}^4)\, dx_1, \\ &= \frac{\sigma\varepsilon\pi r_{o1}}{2-\varepsilon} L_{nj}\Big[\frac{T_j^5 - T_n^5}{5T_j - T_n} - T_{am}^4\Big], \end{aligned} \tag{A.17}$$

and similarly, we can get the heat loss through radiation over length L_{cn} and L_{jf},

$$\begin{aligned} P_{lr0} &= \frac{\sigma\varepsilon\pi r_{o1}}{2-\varepsilon} L_{cn}\Big[\frac{T_c^5 - T_n^5}{5T_c - 5T_n} - T_{am}^4\Big], \\ P_{lr2} &= \frac{\sigma\varepsilon\pi r_{o2}}{2-\varepsilon} L_{jf}\Big[\frac{T_f^5 - T_j^5}{5T_f - T_j} - T_{am}^4\Big]. \end{aligned} \tag{A.18}$$

The total heat loss by radiation contains a few more surfaces, including front surface of oven, side of the bottom flange, backside of the bottom flange.

$$P_{lr} = \sum_{i=1} P_{lri}. \tag{A.19}$$

The total heat loss by heat conduction P_{con} equals heat transfer rate $\dot{Q}$ through the oven

$$P_{con} = kA_{c1}\frac{T_n - T_j}{L_{nj}}. \tag{A.20}$$

We have known the power consumed by the oven from eqn. (3.1), so the heat loss through air convection is

$$P_{air} = P - P_{con} - P_{lr}. \tag{A.21}$$

Appendix B

List of constants

Parameters used in this thesis are listed below:

Stephen-Boltzman constant $\sigma = 5.670\,374\,419 \times 10^{-8}\,\mathrm{Wm^{-2}K^{-4}}$

Thermal Conductivity of 304 stainless steel $k = 16.2\,\mathrm{W/mK}$

Emissivity of polished stainless steel (400 °C to 600 °C) $\varepsilon_s = 0.22$[55]

Emissivity of pressed, filed graphite $\varepsilon_g = 0.980$[42]

Molar heat capacity of strontium vapour $C_{mole} = 26.4\,\mathrm{J\,mol^{-1}\,K^{-1}}$

Avogadro constant N_A =$6.022\,140\,76 \times 10^{23}\,\mathrm{mol^{-1}}$

Saturation intensity I_{sat} =$43\,\mathrm{mW\,cm^{-2}}$

Reduced Planck constant $\hbar = 1.054\,571\,817 \times 10^{-34}\,\mathrm{J\,s}$

Bohr magneton $\mu_B = 9.274\,009\,994 \times 10^{-24}\,\mathrm{J\,T^{-1}}$

Mass of a strontium atom $M = 1.44 \times 10^{-25}\,\mathrm{kg}$

Boltzman constant $k_\mathrm{B} = 1.380\,648\,52 \times 10^{-23}\,\mathrm{m\,kg^2\,s^{-2}\,K^{-1}}$

References

[1] MH Anderson, JR Ensher, MR Matthews, CE Wieman, and EA Cornell. Observation of bose-einstein condensation in a dilute atomic vapor. *science*, 269:14, 1995.

[2] SV Andreev, VI Balykin, VS Letokhov, and VG Minogin. Radiative slowing and reduction of the energy spread of a beam of sodium atoms to 1.5 k in an oppositely directed laser beam. *JETP Letters*, 34(8):442–445, 1981.

[3] AOSense. *Beam-RevC-XX Cold atomic beam system*, 2018 (accessed January 19, 2017).

[4] Mitsuru Asano and Kenji Kubo. Vapor pressure of strontium below 660 k. *Journal of Nuclear Science and Technology*, 15(10):765–767, 1978.

[5] Matteo Barbiero, Marco G Tarallo, Davide Calonico, Filippo Levi, Giacomo Lamporesi, and Gabriele Ferrari. Sideband-enhanced cold atomic source for optical clocks. *Physical Review Applied*, 13(1):014013, 2020.

[6] D. S. Barker, B. J. Reschovsky, N. C. Pisenti, and G. K. Campbell. Enhanced magnetic trap loading for atomic strontium. *Phys. Rev. A*, 92:043418, Oct 2015.

[7] Gerhard Becker. Zur theorie der molekularstrahlerzeugung mit langen kanälen. *Zeitschrift für Physik*, 162(3):290–312, 1961.

[8] Elliot Bentine. *Atomic mixtures in radiofrequency dressed potentials*. PhD thesis, Oxford University, 2018.

[9] Y Bidel, B Klappauf, JC Bernard, Dominique Delande, Guillaume Labeyrie, Christian Miniatura, D Wilkowski, and Robin Kaiser. Coherent light transport in a cold strontium cloud. *Physical review letters*, 88(20):203902, 2002.

[10] Gary C. Bjorklund. Frequency-modulation spectroscopy: a new method for measuring weak absorptions and dispersions. *Opt. Lett.*, 5(1):15–17, Jan 1980.

[11] S Blatt, AD Ludlow, GK Campbell, Jan Westenkær Thomsen, T Zelevinsky, MM Boyd, J Ye, X Baillard, M Fouché, R Le Targat, et al. New limits on coupling of fundamental constants to gravity using sr 87 optical lattice clocks. *Physical Review Letters*, 100(14):140801, 2008.

[12] Stephen J Blundell and Katherine M Blundell. *Concepts in thermal physics*. OUP Oxford, 2009.

[13] A.J.H. Boerboom, H.W. Reyn, and J. Kistemaker. Heat of sublimation and vapour pressure of strontium. *Physica*, 30(1):254 – 257, 1964.

[14] Kai Bongs, Yeshpal Singh, Lyndsie Smith, Wei He, Ole Kock, Dariusz Świerad, Joshua Hughes, Stephan Schiller, Soroosh Alighanbari, Stefano Origlia, et al. Development of a strontium optical lattice clock for the soc mission on the iss. *Comptes Rendus Physique*, 16(5):553–564, 2015.

[15] William Bowden, Richard Hobson, Ian R Hill, Alvise Vianello, Marco Schioppo, Alissa Silva, Helen S Margolis, Patrick EG Baird, and Patrick Gill. A pyramid mot with integrated optical cavities as a cold atom platform for an optical lattice clock. *Scientific reports*, 9(1):1–9, 2019.

[16] Curtis C Bradley, J Greg Story, Jeffrey J Tollett, Jian Chen, NWM Ritchie, and Randall G Hulet. Laser cooling of lithium using relay chirp cooling. *Optics letters*, 17(5):349–351, 1992.

[17] EM Bridge, J Millen, CS Adams, and MPA Jones. A vapor cell based on dispensers for laser spectroscopy. *Review of Scientific Instruments*, 80(1):013101, 2009.

[18] Francisco Camargo. *Strontium Laser Cooling and Trapping Apparatus*. PhD thesis, Rice University, 2015.

[19] Thierry Chaneliere, David Wilkowski, Yannick Bidel, Robin Kaiser, and Christian Miniatura. Saturation-induced coherence loss in coherent backscattering of light. *Physical Review E*, 70(3):036602, 2004.

[20] Steven Chu, Leo Hollberg, John E Bjorkholm, Alex Cable, and Arthur Ashkin. Three-dimensional viscous confinement and cooling of atoms by resonance radiation pressure. *Physical Review Letters*, 55(1):48, 1985.

[21] Pt Clausing. Über die strömung sehr verdünnter gase durch röhren von beliebiger länge. *Annalen der Physik*, 404(8):961–989, 1932.

[22] I. Courtillot, A. Quessada-Vial, A. Brusch, D. Kolker, G. D. Rovera, and P. Lemonde. Accurate spectroscopy of sr atoms. *The European Physical Journal D - Atomic, Molecular, Optical and Plasma Physics*, 33(2):161–171, May 2005.

[23] Jean-Marie Danet, Michel Lours, Stéphane Guérandel, and Emeric De Clercq. Dick effect in a pulsed atomic clock using coherent population trapping. *IEEE Transactions on Ultrasonics, Ferroelectrics, and Frequency Control*, 61(4):567–574, 2014.

[24] Marcos A. de Araújo, Rubens Silva, Emerson de Lima, Daniel P. Pereira, and Paulo C. de Oliveira. Measurement of gaussian laser beam radius using the knife-edge technique: improvement on data analysis. *Appl. Opt.*, 48(2):393–396, Jan 2009.

[25] WC DeMarcus and EH Hopper. Knudsen flow through a circular capillary. *The Journal of Chemical Physics*, 23(7):1344–1344, 1955.

[26] Christopher J Foot. *Atomic physics*, volume 7. Oxford University Press, 2005.

[27] C Fort, A Bambini, L Cacciapuoti, FS Cataliotti, M Prevedelli, GM Tino, and M Inguscio. Cooling mechanisms in potassium magneto-optical traps. *The European Physical Journal D-Atomic, Molecular, Optical and Plasma Physics*, 3(2):113–118, 1998.

[28] Walther Gerlach and Otto Stern. Der experimentelle nachweis der richtungsquantelung im magnetfeld. *Zeitschrift für Physik*, 9(1):349–352, 1922.

[29] JA Giordmaine and TC Wang. Molecular beam formation by long parallel tubes. *Journal of Applied Physics*, 31(3):463–471, 1960.

[30] Peter W Graham, Jason M Hogan, Mark A Kasevich, and Surjeet Rajendran. New method for gravitational wave detection with atomic sensors. *Physical review letters*, 110(17):171102, 2013.

[31] Ian R Hill, Yuri B Ovchinnikov, Elizabeth M Bridge, E Anne Curtis, and Patrick Gill. Zeeman slowers for strontium based on permanent magnets. *Journal of Physics B: Atomic, Molecular and Optical Physics*, 47(7):075006, 2014.

[32] John R Howell, M Pinar Menguc, and Robert Siegel. *Thermal radiation heat transfer*. CRC press, 2015.

[33] BSj Ivanov and VS Troitskii. Formation of directivity patterns of molecular beams. *SOVIET PHYSICS-TECHNICAL PHYSICS*, 8(4):365, 1963.

[34] C Javaux, IG Hughes, G Lochead, J Millen, and MPA Jones. Modulation-free pump-probe spectroscopy of strontium atoms. *The European Physical Journal D*, 57(2):151–154, 2010.

[35] RH Jones, DR Olander, and VR Kruger. Molecular-beam sources fabricated from multichannel arrays. i. angular distributions and peaking factors. *Journal of Applied Physics*, 40(11):4641–4649, 1969.

[36] Gustav Kirchhoff. Ueber das verhältniss zwischen dem emissionsvermögen und dem absorptionsvermögen der körper für wärme und licht. *Annalen der Physik*, 185(2):275–301, 1860.

[37] Martin Knudsen. Die gesetze der molekularströmung und der inneren reibungsströmung der gase durch röhren. *Annalen der Physik*, 333(1):75–130, 1909.

[38] Ole Kock, Wei He, Dariusz Świerad, Lyndsie Smith, Joshua Hughes, Kai Bongs, and Yeshpal Singh. Laser controlled atom source for optical clocks. *Scientific reports*, 6:37321, 2016.

[39] Sebastian Kraft, Felix Vogt, Oliver Appel, Fritz Riehle, and Uwe Sterr. Bose-einstein condensation of alkaline earth atoms: Ca 40. *Physical review letters*, 103(13):130401, 2009.

[40] G Lamporesi, S Donadello, S Serafini, and G Ferrari. Compact high-flux source of cold sodium atoms. *Review of Scientific Instruments*, 84(6):063102, 2013.

[41] J Lee, JA Grover, LA Orozco, and SL Rolston. Sub-doppler cooling of neutral atoms in a grating magneto-optical trap. *JOSA B*, 30(11):2869–2874, 2013.

[42] David R Lide. *CRC handbook of chemistry and physics*, volume 85. CRC press, 2004.

[43] Andrew D Ludlow. *The strontium optical lattice clock: optical spectroscopy with sub-Hertz accuracy*. PhD thesis, Brigham Young University, 2008.

[44] Andrew D Ludlow, T Zelevinsky, GK Campbell, S Blatt, MM Boyd, Marcio HG de Miranda, MJ Martin, JW Thomsen, Seth M Foreman, Jun Ye, et al. Sr lattice clock at 1× 10–16 fractional uncertainty by remote optical evaluation with a ca clock. *Science*, 319(5871):1805–1808, 2008.

[45] Joseph B Mann. Atomic structure calculations. ii. hartree–fock energy results for the elements hydrogen to lawrencium. Technical report, Los Alamos Scientific Lab., N. Mex., 1968.

[46] Tommaso Mazzoni. *Atom interferometry with fermionic and bosonic isotopes of strontium for precision gravity measurements and test of the equivalence principle*. PhD thesis, Universita degli stuidi firenze, 2015.

[47] D J McCarron, S A King, and S L Cornish. Modulation transfer spectroscopy in atomic rubidium. *Measurement Science and Technology*, 19(10):105601, aug 2008.

[48] Harold J Metcalf and Peter Straten. *Laser cooling and trapping of neutral atoms*. Wiley Online Library, 2007.

[49] Giovanni Modugno, Gabriele Ferrari, Giacomo Roati, Robert J Brecha, A Simoni, and Massimo Inguscio. Bose-einstein condensation of potassium atoms by sympathetic cooling. *Science*, 294(5545):1320–1322, 2001.

[50] Takashi Mukaiyama, Hidetoshi Katori, Tetsuya Ido, Ying Li, and Makoto Kuwata-Gonokami. Recoil-limited laser cooling of sr 87 atoms near the fermi temperature. *Physical review letters*, 90(11):113002, 2003.

[51] Nils Nemitz, Takuya Ohkubo, Masao Takamoto, Ichiro Ushijima, Manoj Das, Noriaki Ohmae, and Hidetoshi Katori. Frequency ratio of yb and sr clocks with 5× 10- 17 uncertainty at 150 seconds averaging time. *Nature Photonics*, 10(4):258, 2016.

[52] Matthew A Norcia and James K Thompson. Simple laser stabilization to the strontium 88sr transition at 707 nm. *Review of Scientific Instruments*, 87(2):023110, 2016.

[53] Ingo Nosske, Luc Couturier, Fachao Hu, Canzhu Tan, Chang Qiao, Jan Blume, YH Jiang, Peng Chen, and Matthias Weidemüller. Two-dimensional magneto-optical trap as a source for cold strontium atoms. *Physical Review A*, 96(5):053415, 2017.

[54] Donald R Olander and Valerie Kruger. Molecular beam sources fabricated from multichannel arrays. iii. the exit density problem. *Journal of Applied Physics*, 41(7):2769–2776, 1970.

[55] Tuomas Paloposki and Leif Liedquist. *Steel emissivity at high temperatures*. VTT, 2005.

[56] Benjamin Pasquiou, Alex Bayerle, Slava M Tzanova, Simon Stellmer, Jacek Szczepkowski, Mark Parigger, Rudolf Grimm, and Florian Schreck. Quantum degenerate mixtures of strontium and rubidium atoms. *Physical Review A*, 88(2):023601, 2013.

[57] Hans Pauly. *Atom, Molecule, and Cluster Beams II: Cluster Beams, Fast and Slow Beams, Accessory Equipment and Applications*, volume 32. Springer Science & Business Media, 2013.

[58] E Pedrozo-Peñafiel, F Vivanco, P Castilho, RR Paiva, KM Farias, and VS Bagnato. Direct comparison between a two-dimensional magneto-optical trap and a zeeman slower as sources of cold sodium atoms. *Laser Physics Letters*, 13(6):065501, 2016.

[59] William D Phillips and Harold Metcalf. Laser deceleration of an atomic beam. *Physical Review Letters*, 48(9):596, 1982.

[60] Y.A. Priselkov and A.N. Nesmeyanov. Determination of the vapor pressures of calcium and strontium below their melting points by the method of tagged atoms. *Dokl. Akad. Nauk SSSR*, 95:1207–1210, 01 1954.

[61] Sean Ravenhall. *A compact, high-flux source of cold atoms*. PhD thesis, University of Oxford, 2018.

[62] KJ Ross and B Sonntag. High temperature metal atom beam sources. *Review of scientific instruments*, 66(9):4409–4433, 1995.

[63] Ch Salomon, J Dalibard, WD Phillips, A Clairon, and S Guellati. Laser cooling of cesium atoms below 3 μk. *EPL (Europhysics Letters)*, 12(8):683, 1990.

[64] Marco Schioppo, Nicola Poli, Marco Prevedelli, Ch Lisdat, U Sterr, GM Tino, et al. A compact and efficient strontium oven for laser-cooling experiments. *Review of Scientific Instruments*, 83(10):103101, 2012.

[65] Giacinto Scoles et al. *Atomic and molecular beam methods*, volume 1. Oxford university press New York, 1988.

[66] Ruwan Senaratne, Shankari V Rajagopal, Zachary A Geiger, Kurt M Fujiwara, Vyacheslav Lebedev, and David M Weld. Effusive atomic oven nozzle design using an aligned microcapillary array. *Review of Scientific Instruments*, 86(2):023105, 2015.

[67] Chloe So, Nicholas L. R. Spong, Charles Möhl, Yuechun Jiao, Teodora Ilieva, and Charles S. Adams. Zeeman-tunable modulation transfer spectroscopy. *Opt. Lett.*, 44(21):5374–5377, Nov 2019.

[68] F Sorrentino, G Ferrari, N Poli, R Drullinger, and GM Tino. Laser cooling and trapping of atomic strontium for ultracold atoms physics, high-precision spectroscopy and quantum sensors. *Modern Physics Letters B*, 20(21):1287–1320, 2006.

[69] Daniel A Steck. Sodium d line data. *Report, Los Alamos National Laboratory, Los Alamos*, 124, 2000.

[70] Daniel A Steck. Rubidium 87 d line data, 2001.

[71] Schreck Florian Stellmer, Simon and Killian Thomas. Degenerate quantum gases of strontium. *Annual Review of Cold Atoms and Molecules*, 2:80, 2014.

[72] Simon Stellmer, Rudolf Grimm, and Florian Schreck. Production of quantum-degenerate strontium gases. *Physical Review A*, 87(1):013611, 2013.

[73] Simon Stellmer, Meng Khoon Tey, Bo Huang, Rudolf Grimm, and Florian Schreck. Bose-einstein condensation of strontium. *Physical review letters*, 103(20):200401, 2009.

[74] Yosuke Takasu, Kenichi Maki, Kaduki Komori, Tetsushi Takano, Kazuhito Honda, Mitsutaka Kumakura, Tsutomu Yabuzaki, and Yoshiro Takahashi. Spin-singlet bose-einstein condensation of two-electron atoms. *Physical Review Letters*, 91(4):040404, 2003.

[75] Angharad Mair Thomas. *Ultra-cold collisions and evaporative cooling of caesium in a magnetic trap*. PhD thesis, University of Oxford, 2004.

[76] C. G. Townsend, N. H. Edwards, K. P. Zetie, C. J. Cooper, J. Rink, and C. J. Foot. High-density trapping of cesium atoms in a dark magneto-optical trap. *Phys. Rev. A*, 53:1702–1714, Mar 1996.

[77] Dimitrios Trypogeorgos. *Periodically driven atomic systems*. PhD thesis, University of Oxford, 2014.

[78] Dimitrios Trypogeorgos. *Periodically driven atomic systems*. PhD thesis, University of Oxford, 2014.

[79] Xinye Xu, Thomas H Loftus, John L Hall, Alan Gallagher, and Jun Ye. Cooling and trapping of atomic strontium. *JOSA B*, 20(5):968–976, 2003.

[80] Tao Yang, Kanhaiya Pandey, Mysore Srinivas Pramod, Frederic Leroux, Chang Chi Kwong, Elnur Hajiyev, Zhong Yi Chia, Bess Fang, and David Wilkowski. A high flux source of cold strontium atoms. *The European Physical Journal D*, 69(10):1–12, 2015.

[81] Masami Yasuda and Hidetoshi Katori. Lifetime measurement of the p 2 3 metastable state of strontium atoms. *Physical review letters*, 92(15):153004, 2004.

[82] Xibo Zhang and Jun Ye. Precision measurement and frequency metrology with ultracold atoms. *National Science Review*, 3(2):189–200, 2016.

[83] P Zugenmaier and H-J Cantow. Ein einfaches verfahren zur indizierung von röntgenweitwinkel-reflexen von substanzen mit orthorhombischer elementarzelle. *Kolloid-Zeitschrift und Zeitschrift für Polymere*, 230(1):229–236, 1969.